UNIVERSITÄT DER BUNDESWEHR
FAKULTÄT FÜR LUFT- UND RAUMFAHRTTECHNIK
INSTITUT FÜR RAUMFAHRTTECHNIK UND WELTRAUMNUTZUNG

# WEAK AND DEGRADED SIGNAL ACQUISITION TECHNIQUES IN GNSS SOFTWARE RECEIVER

Ayse Sicramaz Ayaz

Vollständiger Abdruck der von der Fakultät für Luft- und Raumfahrttechnik
der Universität der Bundeswehr München zur Erlangung des akademischen Grades eines

Doktor-Ingenieur (Dr.-Ing.)

genehmigte Dissertation.

Vorsitzender: Prof. Dr.-Ing. Peter Stütz
Gutachter/Gutachterin:
1. Prof. Dr.-Ing. Bernd Eissfeller
2. Prof. Dr.-Ing.Wolfgang Gerstacker

Die Dissertation wurde am 15.02.2013 bei der Universität der Bundeswehr München eingereicht und durch die Fakultät für Luft- und Raumfahrttechnik am 13.03.2013 angenommen. Die mündliche Prüfung fand am 18.10.2013 statt.

# PREFACE

I want to express my deepest gratitude to my supervisors, Prof. Bernd Eissfeller, Prof. Wolfgang Gerstacker and Prof. Günter Hein for their encouraging attitude and attentive guidance. I appreciate their unfailing support and valuable comments on my research problems.

I owe my sincere thanks to Dr. Thomas Pany for providing me excellent research facilities and support. He coordinated effective examples and pragmatic insights to follow as a researcher and I feel fortunate to share the common academic environment with him for some time. I also thank to my former colleague Dr. Jae-Gyu Jang for the joyful discussions we have made on the common projects we worked.

I would like to thank my Software Receiver group colleagues especially to Dr. Jong-Hoon Won to stimulate me to finish the thesis and also Dr. Sun-Jun Ko, Daniel Sanroma, Thomas Kraus, Dr. Isabelle Kraemer and Marco Anghlieri.

I am grateful to my parents Edibe, Rahmi for their encouragement during my whole life. Most importantly, I thank my husband Serkan for his love and understanding throughout the thesis duration. Finally, my warmest thanks go to my daughter Elif to lead me to perceive the sense of life and give me joyful moments.

# ABSTRACT

Navigation systems play a significant role in today's location based services. The dependency on navigation systems is increasing fast in different application domains such as intelligent transport systems, rail transportation, precision agriculture, surface mining, trackers and defense sector. These systems possess GNSS receivers in their infrastructures either reporting their real-time position to a related organization or using navigation information directly. Depending on the application domain, GNSS signals can be affected from indoor, urban channel conditions or various interference, jammer sources. As the number of GNSS users increase, the research community began to focus on these challenging problems that result in more advanced receiver architectures. One of the main components of these receiver architectures is the acquisition block that is the most time consuming process in the receiver. In these harsh environment conditions, it becomes demanding that acquisition process be able to work in an energy efficient way due to the battery limitation of GNSS products such as Personal Digital Assistance (PDA)s and smartphones.

The dissertation has two main contributions, namely performance analysis of high sensitivity acquisition algorithms and interference suppression methods in GNSS receiver so-called ipexSR developed in University of Federal Armed Forces Munich. In our investigations, computational cost of algorithms is also considered since fast acquisition is a preferential criterion in GNSS receivers. In the first part, sensitivity analysis of GNSS signals considering signal modulation is evaluated. The simulations indicate that coherent integration time specifies the main sensitivity gain. In our analysis, using assisted GNSS, long coherent integration effect is investigated in the presence of error sources, i.e. clock jitter, receiver acceleration and channel effect. The results show that Rayleigh fading channel causes the major acquisition sensitivity loss among all error sources. In the second part, interference signals effect on acquisition process is studied. Interference detection and mitigation methods of pulse blanking, short-time Fourier Transform (STFT), Wavelet transform, fractional Fourier transform (FrFT) are investigated. In particular, STFT-Forward Consecutive Mean Excision (FCME) is studied as one of the promising alternatives to deal with pulse and continuous wave interference also providing feasible

computational complexity in real-time receiver. Our work also includes the analysis of the novel FrFT algorithm for chirp jammer signal detection. This part of the work is the first attempt to use FrFT in GNSS domain for chirp jammer signal detection and mitigation.

# ZUSAMMENFASSUNG

Navigationssysteme spielen eine wichtige Rolle in heutigen standortbasierten Dienstleistungen. Die Abhängigkeit auf Navigationsanlagen erhöht sich für viele Systeme wie intelligentes Verkehrssystem, Schienenverkehrstechnik, präzise Landwirtschaft, Tagesbergbau und Verteidigungssektor schnell. Diese Systeme besitzen GNSS-Empfänger in ihren Infrastrukturen, die entweder ihre Echtzeitposition zu einer in Verbindung stehenden Organisation berichten oder direkt selbst Navigationsinformationen verwenden. Je nach Anwendungsgebiet können GNSS Signale vom Innenraum in Gebäuden, städtischen Kanal- Bedingungen oder verschiedenen Störquellen (u.a. auch Jammer) beeinflusst werden. Da die Anzahl von GNSS-Benutzern stetig wächst, fing die Forschungsgemeinschaft an, sich auf diese schwierigen Probleme zu konzentrieren, um eine modernere Empfängerarchitektur zu entwickeln. Eine der Hauptkomponenten dieser Empfängerarchitektur ist die Akquisitionseinheit, welche das rechenintensivste Verfahren im Empfänger darstellt. In diesen harten Umgebungsbedingungen wird verlangt, dass der Akquisitionsprozess aufgrund der Batteriebeschränkung der GNSS-Produkte wie PDAs und Smartphones in der Lage ist, in einer energieeffizienten Art und Weise zu arbeiten.

Die Dissertation hat zwei Hauptbeiträge, nämlich die Leistungsanalyse von hohen Empfindlichkeitsalgorithmen der Signalakquisition und die Entstörungsmethoden mithilfe des GNSS-Empfänger „ipexSR“, welcher an der Universität der Bundeswehr München entwickelt wurde. In unseren Untersuchungen wird auch der Rechenaufwand der Algorithmen betrachtet, da eine schnelle Signalerfassung ein bevorzugtes Kriterium in GNSS-Empfängern ist. Im ersten Teil wird die Empfindlichkeit der GNSS-Signale unter Berücksichtigung der Signalmodulation analysiert und ausgewertet. Die Simulationen zeigen an, dass die kohärente Integrationszeit den höchsten Empfindlichkeitsgewinn spezifiziert. Jedoch ist es bei der Pilotsignal-Akquisition kritisch den Suchraum von Hilfsdaten zu reduzieren, da die Empfindlichkeit nicht nur von der kohärenten Integrationszeit abhängt, sondern auch von der der Suchraumdimension aufgrund der erhöhten Fehlalarmwahrscheinlichkeit. Nach der Leistungsanalyse unter Verwendung von

unterstützten GNSS, wird die lange kohärente Integrationswirkung in Anwesenheit der Fehlerquellen wie Taktjitter, Empfängerbeschleunigung und Kanaleffekte untersucht. Die Ergebnisse zeigen, dass der Rayleigh-Fading-Kanal die größten Akquisitionsempfindlichkeitsverluste unter allen Fehlerquellen verursacht. Im zweiten Teil werden die Störsignaleinflüsse auf den Akquisitionsprozess untersucht. Hier werden die Interferenzerkennung und -unterdrückungsmethoden durch Ausblendung von Signalpulsen und Kurzzeit-Fourier-Transformation (STFT), Wavelet-Transformation, fraktionierte Fouriertransformation (FrFT) vorgestellt. Insbesondere wird STFT-FCME als eine der vielversprechendsten Alternativen studiert, welche mit kontinuierlichen und gepulsten Interferenzen mit einem durchführbaren Rechenaufwand in Echtzeit-Empfänger umgehen kann. Ein weiterer neuer DSP-Algorithmus ist die FrFT basierte Exzision für die Signalunterdrückung von Jammern mit Chirpsignalen.

CONTENTS

LIST OF ALGORITHMS

# LIST OF SYMBOLS

| | |
|---|---|
| $a$ | Line of sight acceleration |
| $c$ | Speed of light |
| $c_{PRN}^{com}$ | Modified compensated local code |
| $d$ | Navigation data bit |
| $e_{E1-A}$ | Galileo E1 PRS channel |
| $e_{E1-B}$ | Galileo E1 OS data channel |
| $e_{E1-C}$ | Galileo E1 OS pilot channel |
| $E$ | Signal energy after coherent integration time |
| $\xi_i$ | Code delay of the locally generated code |
| $f_A(x)$ | PDF of the signal bin using non-central chi-square distribution |
| $f_c(t)$ | Time-varying frequency-offset |
| $f_{chip}$ | Chip rate in [chip/s] |
| $f_{DME}$ | Carrier frequency of the DME signal |
| $f_{D0}$ | Initial Doppler frequency |
| $f_{RF}$ | RF frequency |
| $f_s$ | Sampling rate |
| $f_s''$ | Decimation sampling rate |
| $f_s'''$ | Resampling sampling rate |
| $F_d$ | Decimation factor |
| $G$ | Correlator gain |
| $G_p$ | Processing gain |
| $h(\tau)$ | Window function |
| $H_0$ | Hypothesis considering noise without presence of desired signal |
| $H_1$ | Hypothesis with presence of noise and desired signal |
| $l_c$ | Code length in meters |
| $I_k(x)$ | Modified Bessel function of the first kind of order k |
| $K_a(t,u)$ | Kernel function |
| $L_{imp}$ | System implementation loss |
| $r_{TCG}$ | Compression gain |
| $n_{f_d}$ | Number of Doppler bins |
| $N_s$ | Oversampling factor |
| $s_\mu$ | Transmit signal |
| $\Delta\tau$ | Code phase offset |
| $\hat{\tau}$ | Code phase estimate |
| $\Delta f_d$ | Doppler frequency offset |
| $\Delta F_d$ | Doppler search range |
| $m$ | Number of non-coherent integrations |
| $N_s$ | Number of acquisition search bins |
| $P$ | Signal power in [dBHz] |
| $P(Y)$ | P(Y) code |
| $P_d$ | Detection probability |
| $P_{fa}$ | Probability of false alarm |
| $P(t,w)$ | Time-frequency distribution |
| $r_\mu$ | Received signal after analog to digital conversion (ADC) |
| $r_\mu^{blank}$ | Blanked IF signal |

| | |
|---|---|
| $r_{\mu}^{clip}$ | Clipped IF signal |
| $\mathrm{r_{IF}}$ | Received IF signal |
| $\mathrm{r_{v}'}$ | Decimated received samples |
| $\mathrm{r_{K}'''}$ | Resamples received samples |
| $\mathrm{r_{pp}}$ | Received DME pulse pair |
| $\mathrm{r_{DME}}$ | Received DME signal |
| R | Correlation function |
| $R_{fp}$ | Largest correlation peak |
| $R_{mp}$ | Mean correlation peak |
| $R_{sp}$ | Second largest correlation peak |
| $R_a(u)$ | The a-th order FrFT |
| $\mathrm{s_{CI}}$ | Chirp jammer signal |
| $\mathrm{s_{CWI}}$ | Continuous wave interference signal |
| $\mathrm{t_{\mu}}$ | Time of μ-th sample |
| $T_{blank}$ | Blanking threshold |
| $\mathrm{T_c}$ | PRN code chip duration |
| $\mathrm{T_{code}}$ | Code period |
| $\mathrm{T_{coh}}$ | Coherent integration time |
| $\mathrm{T_{chip}}$ | Chip duration |
| $T_{clip}$ | Clipping threshold |
| $\mathrm{T_d}$ | The test statistic of the differential detector |
| $\mathrm{T_{dp}}$ | Test statistics of the dot-product detector |
| $\mathrm{T_{difr}}$ | Test statistics of the differential real detector |
| $\mathrm{T_{FCME}}$ | FCME threshold |
| $T_{high}$ | Higher threshold |
| $\mathrm{T_{low}}$ | Lower threshold |
| $\mathrm{T_p}$ | P(Y) code chip duration |
| $\mathrm{T_{PRN}}$ | Duration of one ranging code period [s] |
| $\mathrm{T_{st}}$ | Test statistics of the non-coherent squaring detector |
| $\mathrm{T_{unc}}$ | Uncertainty time |
| $\mathrm{\theta_{DME}}$ | Carrier phase of DME signal |
| $\Phi(t)$ | Wavelet mother function |
| $\Phi_{s,d}^{*}$ | Wavelet with variables scale and dilate |
| $\varphi$ | Carrier phase offset |
| $\varphi_{\mathrm{rec}}$ | Initial carrier phase offset |
| $\alpha$ | Rotation angle |
| $\mathrm{v_0}$ | Initial relative velocity |
| $\mathrm{W(s,\tau)}$ | Wavelet with its variables scale s and translation τ |
| $\mathrm{x(t)}$ | Line of sight distance at time t |
| $\mathrm{x_0}$ | Initial relative distance |
| $u_a$ | Chirp rate of the signal |
| $y_{\mu}$ | Deformed signal |

# LIST OF ABBREVIATIONS

| | |
|---|---|
| AOA | Angle of Arrival |
| ACF | Auto Correlation Function |
| ADC | Analog to Digital Converter |
| AGC | Automatic Gain Control |
| AltBOC | Alternative BOC modulation |
| ATC | Air Traffic Control |
| AWGN | Additive White Gaussian Noise |
| BPSK | Binary Phase Shift Keying |
| BOC | Binary Offset Carrier |
| CASM | Coherent Adaptive Subcarrier Modulation |
| CBOC | Coherent Binary Offset Carrier |
| CDMA | Code Division Multiple Access |
| CIT | Coherent Integration Time |
| CJ | Chirp Jammer |
| $C/N_0$ | Carrier to noise density ratio |
| CPU | Central Processing Unit |
| CWI | Continuous Wave Interference |
| DD | Differential Detectors |
| DLL | Delay Locked Loop |
| DOA | Direction Of Arrival |
| FCME | Forward Consecutive Mean Excision |
| FD | Frequency Domain |
| FFT | Fast Fourier Transform |
| FrFT | Fractional Fourier Transform |
| GIOVE | Galileo Test Satellite |
| GPS | Global Positioning System |
| GNSS | Global Navigation Satellite System |
| JSR | Jammer to Signal Ratio |
| JTIDS | Joint Tactical Information Distribution System |
| IF | Intermediate Frequency |
| ITS | Intelligent Transport Systems |

| | |
|---|---|
| LDACS | L-band Digital Aviation Communications System |
| LHCP | Left Hand Circularly Polarized |
| LNA | Low Noise Amplifier |
| LO | Local Oscillator |
| LOS | Line of sight |
| MAI | Multiple Access Interference |
| MBOC | Multiplexed Binary Offset Carrier |
| MF | Matched Filter |
| MIDS | Multifunctional Information Distribution System |
| ML | Maximum Likelihood |
| MSE | Mean Square Error |
| NCD | Non Coherent Detection |
| NCS | Non Coherent Squaring |
| NLOS | Non Line of Sight |
| NF | Noise Figure |
| OCXO | Oven Controlled Crystal Oscillator |
| PDA | Personal Digital Assistance |
| PDF | Probability Density Function |
| PLL | Phase Locked Loop |
| PRN | Pseudo Random Noise |
| PRS | Public Regulated Service |
| PRF | Pulse Repetition Frequency |
| PSI | Pulse Interference |
| RHCP | Right Hand Circularly Polarized |
| SDR | Software Defined Radio |
| STFT | Short Time Fourier Transform |
| STFrFT | Short Time Fractional Fourier Transform |
| TACAN | Tactical Air Navigation |
| TD | Time Domain |
| TDM | Time Division Multiplexing |
| TTFF | Time to First Fix |
| UWB | Ultra Wide Band |
| VMS | Vessel Monitoring System |

# CHAPTER 1. INTRODUCTION

In recent years, satellite based navigation began to play a significant role in social life. Navigators are no longer luxuries and become absolute necessities in our daily lives. The competition in the satellite navigation has led to the coexistence of several navigation systems in the world. Besides US-GPS, European counterpart of GALILEO, Russian contribution GLONASS and Chinese BeiDou leads new global navigation satellite systems (GNSS). This competition introduces new challenges in receiver architecture design to acquire various signals. The continuity of digital radio towards multicarrier, multi-standard receivers is a potential solution which is known as the GNSS Software Defined Radio (SDR) concept. The main idea comes from replacing some hardware components with software signal processing modules in a GNSS receiver which allows dynamically adapting to different signals. The demand of software solutions over their hardware counterparts such as correlators resides mainly on their flexibility on modifications of the implementations and high configurability.

Thanks to the compatibility and interoperability of GNSS signals, at the user level it provides an opportunity to improve signal availability, sensitivity, positioning accuracy and thus guarantee of service. This will also provide sub-meter positioning and shorter initialization time. Users receiving signals from multiple satellite systems have the advantage of service continuity in case one of the systems fails and benefit for a more reliable signal acquisition and tracking especially in Safety of Life (SoL) applications.

Indoor and dense urban positioning concepts has a big demand due to the US FCC 911 and EU E112 mandates used in location services in mobile positioning networks. Satellite positioning is the most suitable candidate to implement this service however there is significant satellite signal degradation in indoor and dense urban environments that motivates research community to focus on indoor and urban GNSS scenarios. Generally speaking, the receiver acquires signals in different sensitivity levels due to various environment structures causing multipath, non-line of sight (NLOS) signal, indoor cross-correlation, interference signals and this degradation of around 30 dB effect must be compensated at the receiver to achieve a certain positioning accuracy.

The objective of this thesis is to present optimal algorithms mainly for weak and degraded signal detection and provide performance comparison of available GNSS signals using variety of indoor,

AGPS and interference mitigation algorithms. In this thesis, following topics have been investigated:

- Acquisition process theory and performance comparison using several detector implementations and signals in GNSS software receiver.
- Indoor and assisted acquisition theory with drawbacks and enhancements on the performance using various signal structures and algorithms.
- Interference detection/mitigation algorithms and their effect on acquisition and tracking performance in GNSS receiver.

## 1.1 Literature Overview

Recently, GNSS receivers built in as a standard feature in mobile phones, PDAs that are fed by battery powered units. Since in a mobile phone or in mid-products there are numerous applications, there is then a demand to keep battery power requirements low in GNSS receivers. On the one hand battery requirements to be considered and on the other hand due to the E911/E112 mandates requirements to function in indoor environments should also be meet. At this stage, acquisition module becomes critical that is the most time consuming process in the receiver and a fast acquisition becomes demanding.

A fast acquisition effort was firstly considered in the context of FFT based acquisition [1] by searching all possible code bins in one step using FFT-based correlator. The parallel code phase search via circular correlation concept is introduced in [2] to rapidly calculate correlation results using FFT and IFFT operations. In the early 2000s, FFT based method is proposed by [3] for the process of acquisition in an optimized manner by applying two-dimensional FFTs for both code phase and Doppler frequency and reducing the complexity in a considerable extent by reusing intermediate computations.

Besides fast acquisition, efforts are also focused on the analysis of different detectors for weak signal acquisition. The non-coherent squaring detector was introduced that becomes common in traditional receiver architectures due to increasing the sensitivity of the receiver by wiping out the limitation of navigation data bit sign. Then, the maximum likelihood estimator based acquisition that provides optimal results in the absence of navigation data and code Doppler effect is introduced by [4]. The differentially coherent combining detector was first proposed by [5] that

partially mitigate the squaring loss problem which is a main issue in non-coherent squaring detectors. Differentially coherent combining detectors provide an increase in the receiver sensitivity and a low complexity in the acquisition parameters estimation. References [6], [7], [8] further made performance comparisons with differentially coherent combining detectors in GNSS receivers.

There is an interest to assess new capabilities of the incoming GNSS signals and their potentials for the location based and emergency services in GNSS enabled mobile phone or PDA. The performance of GNSS is known to be severely affected in indoor environments. Indeed, the ability of GNSS signal detection in a harsh environment is the key issue to use GNSS positioning systems in location based applications. Although high sensitivity GPS technology of the current state of the art can cover car navigation and dense urban canyon area, the core indoor area is still a big challenge due to its physical limits. However, a considerable amount of effort has been spent on indoor navigation after the signal design issues of Galileo and modernized GPS. These signals provide a new possibility in the next years that will partially overcome current limitations of indoor environment conditions. Besides signal design issues, different acquisition algorithms are also in discussion. These methods can be classified into classical method [3], [9], strong satellite signal cancellation [10], [11] and fine frequency estimation [12], [13] methods. All algorithms mainly cope with means to detect the weak signal in indoor conditions and meanwhile keeping a probable acquisition time.

GNSS receivers are often subject to interference signals that degrade the acquisition sensitivity and cause loss of lock of tracking loops. Therefore, the key enabling solution is to have interference mitigation techniques implemented at the receiver. The mitigation methods are applied at the receiver considering interference signal type, thus the classification of the interference source needs to be analyzed prior to mitigation phase, namely using the design of *pre-correlation* techniques. Interfering signals affect the acquisition process by degrading the autocorrelation peaks causing false acquisition or desired signal acquisition may fail. Approaches depend strongly on the type of interference signal. In the literature, early studies rely on the interference effects of code acquisition in CDMA systems. Code acquisition under effect of narrowband interference has been studied by [14] and considerable reduced acquisition time is achieved using Fourier transform based interference mitigation methods. The effect of continuous wave interference (CWI) is studied in [15], [16] and in [15] pulse jammers effect on the performance of code acquisition is analyzed and concluded that mean acquisition time is highly

increased. With pulse jammer, if the chip rate to pulse repetition frequency (PRF) ratio is smaller than the number of chips during correlation then the duty factor would have no effect on acquisition performance. For the case of large Jamming to Signal ratio (J/S) CWI, there occurs severe performance degradation; on the other hand in pulse jamming, it presents duty cycle dependent performance degradation. The effect of CWI and pulse jamming on Matched Filter (MF) based code acquisition is studied by [17] and presented that the CWI signal effect can be mitigated using MF based acquisition. To mitigate the narrowband interference, notch filter is used [18]. With increased bandwidth of interference signals, the filter becomes less effective depending on the power of interference signals.

In GNSS domain, interference mitigation methods become a hot topic at the time of writing the thesis. Similar to the CDMA literature, the interference suppression algorithms depend on the type of the interference and there is a common approach of using *pre-correlation* mitigation methods rather than *post-correlation*. Initially, the GPS receiver sensitivity degraded by real world interference signals was reported in [19] and finalized that GPS is vulnerable to potential interference effects which cannot be completely eliminated but can be diminished. The interference effects on acquisition process were evaluated by [20], [21] and stated that the required interference power level to prevent acquisition process differs depending on the type of the interference signal itself. Further, a considerable amount of effort has been spent to analyze various pre-correlation methods for a specific type of an interference signal. In terms of pulse interference, most promising methods applied are in time-domain. Pulse blanking is proposed by [22], [23] that is simple to implement and convenient for a real-time GNSS receiver design. A combination of pulse blanking and wavelet based mitigation algorithm is proposed [24] in the presence of a strong Distance Measuring Equipment (DME) signal. Against CWI, a theoretical study using adaptive notch filter based acquisition performance is analyzed by [25]. An STFT based suppression method is investigated in [26] using real Galileo signals in the presence of DME interference.

## 1.2 Dissertation Outline

The dissertation has two main contributions, namely performance analysis of high sensitivity acquisition algorithms and interference suppression methods in GNSS receiver so-called ipexSR developed in University of Federal Armed Forces, Munich. In our investigations, computational

cost of algorithms is also considered since fast acquisition is an important criterion in GNSS receivers. The thesis is organized as follows. CHAPTER 2 gives a brief overview of GNSS receiver architecture. CHAPTER 3 describes main points of acquisition, the derivations to estimate acquisition parameters of code phase and Doppler frequency via maximum likelihood method. Then, sensitivity analysis of GNSS signals considering signal modulation is evaluated. CHAPTER 4 presents a comparison of the most commonly used detectors used in GNSS receivers. CHAPTER 5 mainly deals with indoor and assisted acquisition performance comparison of GNSS signals. Using assisted GNSS, long coherent integration effect is investigated in the presence of error sources, i.e. clock jitter, receiver acceleration and channel effect. Chapter 6 presents possible interference detection and mitigation algorithms providing computationally attractive and good performance results. In this chapter, interference detection and mitigation methods of pulse blanking, short-time Fourier Transform (STFT), Wavelet transform, fractional Fourier transform (FrFT) are investigated.

## 1.3 Publication List

Two directions of research within GNSS signal acquisition have been considered in this thesis. Papers I –VII deals with signal acquisition methods in software receivers, analysis on assisted and indoor acquisition. Paper VIII-XII considers the pre-correlation interference suppression methods in the software receiver.

[I] A.Sicramaz Ayaz, “Analysis of Differential Acquisition Methods by using Monte-Carlo Simulations”, ION-GNSS 2005, 13-16 September, 2005, Long Beach, California

[II] A.Sicramaz Ayaz, T.Pany, B.Eissfeller, J.H.Won, “FFT Based Acquisition Algorithm in a Multi-Frequency Software Receiver”, IGNSS Symposium, 2006, Holiday Inn Surfers Paradise

[III] A.Sicramaz Ayaz, T.Pany, F.Kneissl, B.Eissfeller,” Performance of Assisted Acquisition of the L2CL Code”, Ka and Broadband Communications Conference, 24-26 September, 2007, Turin, Italy

[IV] A.Sicramaz Ayaz, T.Pany, B.Eissfeller,” Performance of Assisted Acquisition of the L2CL Code in a Multi-Frequency Software Receiver”, ION-GNSS 2007, 25-28 September, 2007, Fort Worth, Texas

[V] M.Anghileri, T.Pany, D.S. Güixens, J.H. Won, A.Sicramaz Ayaz, C.Stöber, I. Krämer, D.Dötterböck, G.W.Hein, B. Eissfeller, "Performance Evaluation of a Multi-frequency GPS/Galileo/SBAS Software Receiver", ION-GNSS 2007, 25-28 September, 2007, Fort Worth

[VI] C. Stöber, M. Anghileri, A. Sicramaz Ayaz, D. Dötterböck, I. Krämer, V. Kropp, D. Sanromà Güixens, J. Hoon Won, B. Eissfeller, T. Pany," ipexSR: A Real-Time Multi-Frequency Software GNSS Receiver", International Symposium ELMAR, 15-17 September 2010, Zadar, Croatia

[VII] A. Sicramaz Ayaz, B. Eissfeller, T. Pany, "Assessment of GNSS Signal Acquisition Sensitivities for Indoor and Urban Scenarios", PIMRC APLEC 2010, 26-29 September 2010, Istanbul, Türkiye

[VIII] A. Sicramaz Ayaz, R. Bauernfeind, J. Gyu Jang, I. Kraemer, D. Dötterböck , B. Ott, T. Pany and B. Eissfeller, "Performance Evaluation of Single Antenna Interference Suppression Techniques on Galileo Signals using Real-time GNSS Software Receiver", ION GNSS 2010, Portland, Oregon

[IX] A. Sicramaz Ayaz, R. Bauernfeind , T. Pany, J. Gyu Jang , B. Eissfeller, „Real-time GIOVE Signal Performance using STFT based Excision Method in the Presence of Interference", ION GNSS 2011, Portland, Oregon

[X] R.Bauernfeind, A. Sicramaz Ayaz, B. Eissfeller, "GNSS Interference Monitoring Network Based on Detection in Automotive ITS Station Receivers", ION GNSS 2011, Portland, Oregon

[XI] A. Sicramaz Ayaz, R. Bauernfeind , T. Pany, B. Eissfeller, "Time-Frequency based Intentional Interference Suppression Techniques in GNSS Receivers", ION GNSS 2012, Nashville, Tennessee

[XII] R.Bauernfeind, T.Kraus, A. Sicramaz Ayaz, D.Dötterböck, D.Fontanella, B. Eissfeller, Analysis, Detection and Mitigation of InCar GNSS Jammer Interference in Intelligent Transport Systems, DLRK Conference, Berlin, 2012

# CHAPTER 2. GNSS RECEIVER ARCHITECTURE

In this chapter, firstly GNSS signal structures, the transmitted signal model and propagation channel effects are described. Afterwards, GNSS receiver architecture is presented.

## 2.1 Transmit Signals Overview

In general, the transmit GNSS signal is composed of data and pilot signals. Each data signal consists of carrier, PRN code and a low rate navigation data. Navigation data comprises satellite health status, satellite position and velocity so called ephemeris, coarse-precision ephemeris data namely almanac and satellite clock error parameters. The almanac data consist of time information and orbital data related to the location of all satellites in the constellation that are updated from ground stations monitoring the constellation. With the use of almanac data, the receiver can initiate acquisition process with the given approximate user position. Besides, ephemeris data contains precise information of position and velocity of satellites over time. Ephemeris data is valid for four hours and transmitted every two hours.

The complex model of the transmitted signal can be modeled as:

$$s_\mu = Ac(t_\mu)d(t_\mu)cos(2\pi f_{RF}t_\mu) + \frac{A}{\sqrt{2}}p(t_\mu)d(t_\mu)sin(2\pi f_{RF}t_\mu) \quad (2\text{-}1)$$

where $A$ represents the amplitude of the signal for all satellites, $c \in \{-1,1\}$ is the PRN code and it is the product of primary code, optionally the secondary code and the subcarrier signal. Primary and secondary codes are pseudo-random memory code sequences where secondary code gives the effect of navigation message, subcarrier signal is the waveform that causes a split spectrum after the modulation, $d \in \{-1,1\}$ is the navigation data sequence, $f_{RF}$ radio frequency in Hertz, $t_\mu$ is the time of sample in second, μ is the sample index, $p$ is the encrypted precision code $P(Y)$ of the satellite.

In Figure 2-1, the structure of GNSS signal transmitter is shown [27]. The signal has a data component and optionally a pilot component. The data component consists of a navigation data sequence having information of satellite availability, satellite trajectories and satellite clock errors. The navigation data sequence follows an optional forward error correction coding in which binary

ranging sequence are BPSK modulated. After multiplication with the PRN code the spread spectrum signal is optionally modulated onto subcarriers. The pilot component has a different spreading sequence that is further modulated onto subcarriers. Then the signal is RF modulated following the combination of baseband data and pilot components.

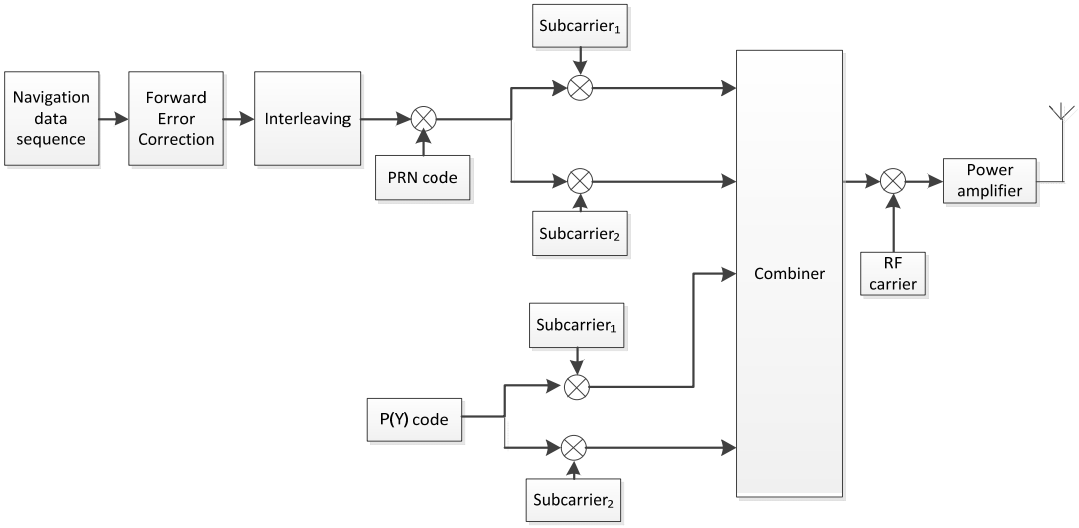


Figure 2-1: GNSS signal transmitter

Table 2.1: Current GNSS signal specifications

| Channel | Code length [chips]/ duration [ms] | | Multiplexing scheme |
|---|---|---|---|
| | Primary | Secondary | |
| L1 C/A | 1023/1 | - | - |
| E1b | 4092/4 | - | CASM |
| L2C | 10230/20 | 767250/1500 | Time Multiplexing |
| L5-I | 10230/1 | 10/10 | Phase Quadrature |
| L5-Q | 10230/1 | 20/20 | |
| E5a-I | 10230/1 | 20/20 | AltBOC |
| E5a-Q | 10230/1 | 100/100 | |
| E5b-I | 10230/1 | 4/4 | |
| E5b-Q | 10230/1 | 100/100 | |

The navigation data sequence and the PRN/P(Y) codes are synchronized to each other, such that navigation data bit transitions arise at code chip transitions. P(Y) code is a long PRN code lasting for one week and has a chipping rate of 10.23 MHz used as a basis for precise positioning services (PPS). In the thesis, P(Y) codes are out of scope and only civil signals are considered. The received signal power levels of GNSS are rather weak and depend on the user elevation angle. The minimum received signal power levels correspond to an elevation angle of 5-degree and main signal structure specifications are tabulated in Table 2.1and Table 2.2. Within modernized GPS, Galileo, Glonass and BeiDou new modulation schemes with long ranging codes is considered. In the receiver, acquisition process of various modulation schemes differs, for example Binary Offset Carrier (BOC) modulated signal has a more complex structure than the BPSK and causes ambiguity due to large secondary peaks owing to the split spectrum of BOC modulation. On the other hand, BOC and its variants i.e. MBOC modulated signals have narrower main lobe of the auto correlation function allowing better accuracy in the tracking process.

In Table 2.2, the minimum Rx power levels illustrated in the table shows no power level offset between GPS and Galileo signals although the minimum Rx power measurements for GPS and Galileo signals are fulfilled with different antenna types.

Table 2.2: Current and Modernized GNSS Signal Structures

| Signals | Compon. | Mod. Scheme | Symbol length [ms] | Code length [chips] | Chip rate [Mcps] | Min. Rx power level [dBW] | Nav. Messge Type | Data rate [sps] |
|---|---|---|---|---|---|---|---|---|
| BeiDou-B1 | (I,Q) | QPSK | NaN | 2046, NaN | 2.046, 2.046 | -163 [3] | (NAV, NAV) | (50,-) |
| BeiDou -B2 | (I,Q) | QPSK | NaN | 2046, NaN | 2.046, 2.046 | -163 [3] | (NAV, NAV) | (50,-) |
| BeiDou -B3 | (I,Q) | QPSK | NaN | 10230, NaN | 10.23, 10.23 | -163 [3] | (NAV, NAV) | (50,-) |
| Glonass L1 C/A | - | BPSK(0.511) | NaN | 511 | 0.511 | -155 | NaN | 50 |
| Glonass L2 | - | BPSK(0.511) | NaN | 511 | 0.511 | -155 | NaN | 50 |
| Glonass L3 | - | BPSK(4) or BPSK(8) | NaN | NaN | 5.11 | NaN | NaN | 100 or 125 |
| GPS L1 C/A | - | BPSK(1) | 20 | 1023 | 1.023 | -158.5 [2] | NAV | 50 |
| GPS L1C | (Data, Pilot) | TMBOC(6,1,1/11) | | 10230 | 1.023 | -157.0 | CNAV-2 | (100,-) |
| GPS L2C | (CM, CL) | BPSK(1) | (20,-) | 10230, 767250 | 0.5115, 0.5115 | -163.0 | (CNAV,-) | (50,-)) |
| GPS L5 | (I5,Q5) | BPSK(10) | (10,-) | 10230, 10230 | 10.23, 10.23 | -157.9 [2] | (CNAV,-) | (100,-) |
| Galileo E1 OS | (Data,Pilot) | CBOC | (4,-) | 4092*1, 4092*25 | 1.023, 1.023 | -157 [1] | (INAV,-) | (250,-) |
| | PRS | BOCc(15,2.5) | NaN | 25575*1 | 10.23 | NaN | NaN | NaN |
| Galileo E5 | E5a Data/Pilot | AltBOC(15,10) | (20,-) | 10230 | 10.23 | -155 [1] | (FNAV,-) | (50,-) |
| | E5b Data/Pilot | | (4,-) | 10230 | 10.23 | -155 [1] | (INAV,-) | (250,-) |
| Galileo E6 | (Data, Pilot) | BPSK(5) | (1,-) | 5115*1, 10230*50 | 5.115, 5.115 | -155 | (CNAV,-) | (1000, -) |
| | PRS | BOCc(15,5) | NaN | 51150*1 | 5.115 | -155 | NaN | NaN |

[1] The minimum Rx power level for Galileo signals is measured based on right hand circularly polarized isotropic 0 dBi antenna and lossless atmosphere.

[2] The minimum Rx power level for GPS signals is measured at the output of a 3 dBi linearly polarized user receiving antenna (located near ground) at worst normal orientation, when the SV is above a 5-degree elevation angle.

[3]The minimum user-received BeiDou signal power level is specified to be -163 dBW for B1I, which is measured at the output of a 0 dB RHCP receiving antenna (located near ground), when the satellite's elevation angle is higher than 5 degree [28].

## 2.2 Multiplexing Schemes Overview

In legacy GPS civil signal called L1 C/A, there exists only data channel, thus no multiplexing is applied on the signal. However, in new signals of GNSS, there are different signal structures containing data and pilot channel components separately which require combining multiple channels to a single channel to transmit over a wireless medium. Therefore, for all new signals multiplexing is performed. There are several multiplexing schemes to combine both channel components used in GNSS as explained in the following:

- *Time Division Multiplexing (TDM)*

In TDM approach, data and pilot channels are transmitted sequentially assigned to a particular time slot on the same carrier. The GPS L2 Civil signal components (L2 Civil Moderate (CM) ($f_{chip} = 0.511$ Mcps) and L2 Civil Long (CL) ($f_{chip} = 0.511$ Mcps)) are combined with TDM at a rate of 1.023 Mcps.

- *Coherent Adaptive Sub-carrier Modulation (CASM)*

CASM is optionally termed as interplex or modified hexaphase modulation in the literature. With CASM, the signal is transmitted with constant power over time so that the signal amplitude does not carry any information. Three components; E1A, E1B and E1C; of the signal are mapped to the two orthogonal phase axes having constellation points with the same amplitude in six possible phases. Galileo E1 signal is combined with CASM to ensure a constant envelope transmit signal [29] on Galileo E1 PRS channel, Open Service (OS) data and pilot channels and the intermodulation product (INT). At one hand, CASM provides a constant envelope on the transmitted signal, on the other hand causes signal transmission with the use of 11.11% less total signal power.

- *Alternative BOC Modulation*

The Alternative BOC modulation (AltBOC) uses a complex subcarrier, therefore the spectrum is

not splitted and it is shifted to higher and lower frequencies. As defined in [30], the AltBOC signal is the product of a PRN code with a complex subcarrier. In Galileo E5 signal structure, four channels (E5a data and pilot, E5b data and pilot) are combined with AltBOC modulation scheme. E5a and E5b signals are BPSK(10) modulated and the AltBOC modulation is used to preserve a constant envelope on the transmitted signal like in 8-PSK constellation. The bits are mapped to the phases of the transmit signal waveform. The power split between four signal components is equally shared as 25%. After AltBOC modulation, using the amplification factors in the multiplexed signal, the power split of the four signal components are calculated. The rates of the power share between signal components vary and 15% of the total signal power is wasted by product signals due to preserving the constant amplitude during transmission.

- *Phase Quadrature Multiplexing*

In GPS L5 signal structure, the I5 and Q5 carrier components are multiplexed in phase quadrature form where Q5 signal carrier lags the I5 signal carrier by 90°. The signal phases are set such that when Q5 signal changes state, a 180° phase reversal of the Q5 carrier occurs. When I5 signal equals one, a 180° phase reversal of the I5 carrier occurs, when Q5(t) equals one, the Q5 carrier advances 90° and when the Q5 signal equals zero, the Q5 carrier shall be retarded by 90° [31].

## 2.3 Propagation Channel

The transmit signal is exposed to phase shifts, delays, power losses, delayed versions of the signal (multipath), tropospheric and ionospheric spread, noise and interference in the propagation channel. To which extent the transmit signal is affected depends on the received signal environment; among them deep urban and indoor environments are the most constraining.

In the literature, mathematical analysis of channel modeling are in general based on oversimplified assumptions, i.e. independent and identically distributed amplitude fading, uniformly distributed Poisson arrival time and no interference between paths. All these simplifications cause unreliable channel modeling and in this regard, empirically driven channel modeling is desired. The multipath is one of the constraining effects on the channel that is caused by multiple reflections of the transmitted signal in the propagation channel. These signal paths have different delays, attenuations and phase shifts induced by various channel conditions. In navigation applications, numerous short delayed multipath occur [32] within urban channel

excess delay range of 1 μs and 300 ηs and in rural environments between 0 and 500 ηs depending on the satellite elevation angle. The greater the satellite elevation angle, the shorter the excess delay and a greater signal power occurs. Multipath replicas of the input signal does not give much degradation on the acquisition sensitivity since the exposed Doppler frequency and code delay on the Rx signal is under acquisition error limits; for indoor multipath the code delay error is within half code chip duration and delay spread is on the order of 10 to 50 ηs [33]. In case of urban multipath, the maximum excess delay is on the order of 1 μs and via measurement campaigns observed generally lower than 0.5 μs [34]. The multipath component with an excess delay shorter than the chip length has a correlation with the LOS component hence causes excessive false acquisition and distorts the positioning accuracy. In general in GNSS applications, multipath components are not considered in the receiver and accepted as useless components as stated in [6], [35]. However, as mentioned in [36] they can also be make use of it in the receiver design.

## 2.4 Received Signal Flow

General signal processing structure in GNSS receiver is shown in Figure 2-2. After the signal is received by a Right Hand Circularly Polarized (RHCP) GNSS antenna, it is processed by Low Noise Amplifier (LNA) having a twofold objective in the front-end. One is to amplify the signal and second is to reject out of band interference. Then the signal is down converted to Intermediate Frequency (IF) via a Local Oscillator (LO). The IF signal is digitized by an Analog to Digital Converter (ADC) which converts the signal stream into a set of samples. Thereafter, samples are quantized by a number of bit levels. In GNSS applications, one bit quantization is sufficient for synchronization and positioning, but higher quantization levels afford improved SNR. However, in strongly interfered GNSS signal case, with one bit receiver the strong interfering signal dominates the correlator. In case of multi bit receivers, 3 or 4 quantization bits are required to gain the desired false alarm probability. After IF samples are then passed to the master receiver where the entire signal processing is controlled. A number of receiver units are attached where each one tracks signals corresponding to a specific PRN code family. With receiver units it is intended to say i.e. GPS L1 C/A, Galileo E1 (E1B, E1C), L2CS (L2CM, L2CL) signal structures. Each receiver unit involves several channels tracking different satellites belonging to the same PRN code family. Acquisition Manager, as its name indicates controls the acquisition process, it is composed of two parts; one part performs the single coherent integration

Fourier acquisition and the second part realizes indoor acquisition especially used for high-sensitivity applications.

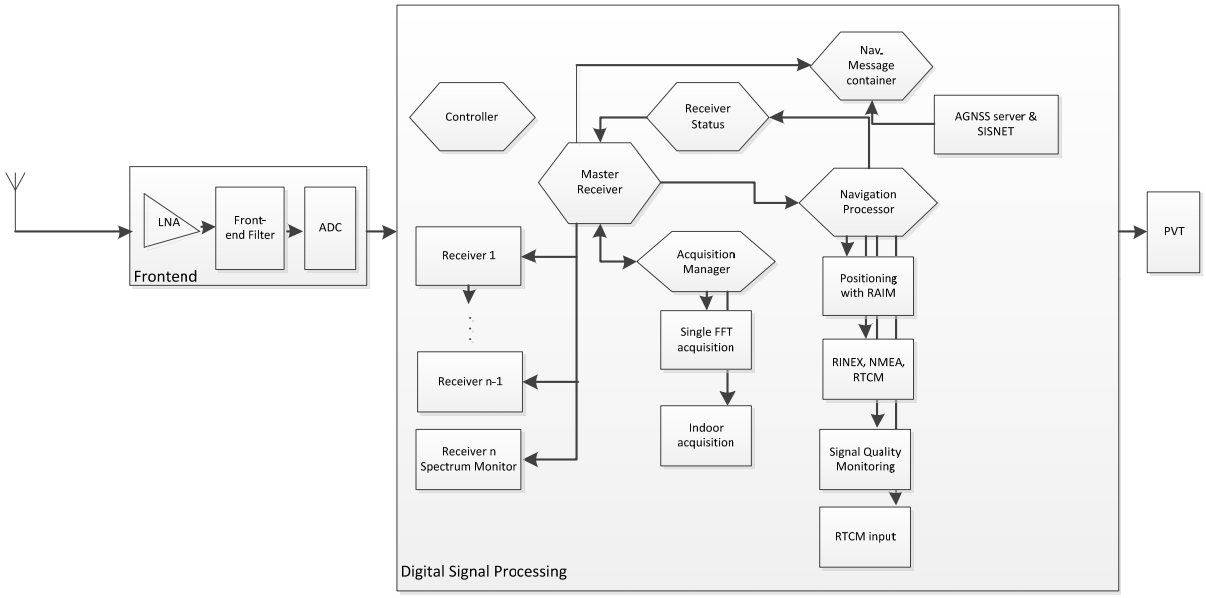


Figure 2-2: Flow diagram of ipexSR SDR unit [37]

The acquisition unit yields coarse timing and carrier frequency to the master receiver which is then passed to correlators. A feedback loop composed of numerous correlators then starts the tracking process providing fine timing, carrier frequency and code phase estimates. The master receiver passes results to the navigation processor which is then sent to one or more navigation modules defined in the configuration file. These modules perform single point positioning, RINEX output and signal quality monitoring to obtain position, velocity and time (PVT) solution.

### 2.4.1 Antenna Characteristics

In general, the GNSS signal is picked up with a RHCP antenna due to RHCP feature on GNSS satellites. Reflected signals from the ground, buildings or obstacles contain large Left Hand Circular Polarization (LHCP) energy and RHCP type antennas are utilized to suppress reflected signals. Certain antennas that feature dual-polarization RHCP/LHCP is used to improve signal detectability in indoor multipath channels as stated in [38]. Interference handling is another feature that can be designed to the antenna by introducing frequency selectivity to avoid the

desired signal from out of band interferers, i.e. base stations, node-Bs or cell phones, etc. GNSS antennas can be classified into three; geodetic, rover and handheld receiver antennas. Geodetic antennas provide high precision on accuracy, multiband and used for fixed site applications. On the other hand, rover antennas are utilized in portable applications and hand-held antennas are single band antennas comprising patch, helical antennas that are the most commonly used ones. In the thesis, Trimble Zephyr Geodetic 2 antenna is used.

### 2.4.2 Front-end Architecture

There are different front-end architectures e.g. superheterodyne, low IF, direct RF to baseband (homodyne) used together with SDR. In the front-end architecture, the sample rate, number of ADC bits, number of frequency bands and bandwidth of signals influence the SDR performance. The RF front-end consists of a broad band LNA, bandpass filters, a mixer, an oscillator and an ADC. The signal is amplified by the LNA and filtered by the RF filter. LNA has a significant effect on the overall system noise figure (NF), since mostly it is located near the antenna. It is required for LNA to keep the desired signal power while adding small noise and distortion to optimize the receiver sensitivity. For dynamic range scenarios and for high sequential stages, LNAs could be designed as a variable gain amplifier (VGA). Next, the frequency of the signal is down-converted from RF to IF domain via mixer and the local oscillator (LO). The LO is the difference between the RF and IF, $f_{LO} = f_{RF} - f_{IF}$. The IF signal can be expressed as:

$$r_{IF}(t) = A_{IF}\, cos\big(2\pi f_{IF} t + \theta(t)\big) + n(t) \tag{2-2}$$

where $A_{IF}$ is the amplitude of the signal, *n(t)* is the additive noise and $\theta(t)$ is the phase of the transmitted signal. At the front-end, the mixing process splits the spectrum into components of $(-2f_{RF} + f_{IF}, -f_{IF}, f_{IF}, 2f_{RF} - f_{IF})$. Then, in the IF stage the bandpass filter passes the desired signals at $(-f_{IF}, f_{IF})$. Since with the mixing process the image frequencies are also translated to IF domain, image frequencies should be removed before the down conversion. After down conversion to IF, the signal is bandpass filtered centered at IF frequency so-called IF filter in order to remove high-frequency components and to prevent aliasing. The ADC takes place after IF filtering and samples the signal at a sampling rate of $f_s = {}^{1}/_{T_s}$ with determined number of bits of quantization. GNSS SDRs requires high sample rates, however it is tried to keep the rate as low as possible due to computational purposes [39].

### 2.4.3 Signal Processing Block

After digitization of the IF signal, it is fed to one of the receiver channels. Each channel is utilized to acquire and track the signal of a single GNSS satellite. In general, receivers impose between 12-20 channels. Acquisition is the initial and coarse synchronization process following the front-end. Acquisition process identifies if the satellite signal is present at the receiver antenna and estimates unknown signal parameters of the visible satellite, code phase offset, Doppler frequency offset and carrier phase offset. After determination of coarse values of synchronization parameters, the receiver passes these values to tracking module to lock on the respective satellite signal. The goal of tracking is to keep tracking of synchronization parameters of the detected satellites. Tracking loops provide fine estimates of synchronization parameters so that they are able to lock on the corresponding parameters by continuously adjusting the locally generated code to match with the received signal. At the end, the signal processing unit provides pseudo-range and carrier phase.

### 2.4.4 Positioning Block

In GNSS positioning, the positions of satellites are known and the aim is to specify the ranges to satellites and solve the proper receiver position. Basically, the navigation solution can be achieved either by solving GNSS observation equations by applying least-squares method or by means of more advanced method of *Kalman* filtering. If previous positions are available then it is possible to update the navigation solution even with less than four satellites. With *Kalman* filtering, this idea is further developed. Positioning module is the final step in the GNSS receiver and hence the accuracy of this module is directly related to the estimation accuracy of the synchronization parameters of code phase, carrier phase and Doppler frequency.

# CHAPTER 3. ACQUISITION PROCESS FUNDAMENTALS

Acquisition is the initial and coarse synchronization process in GNSS receiver following RF to IF conversion in the front-end. It is a combination of detection and estimation process; it is a detector to identify if the satellite signal is present at the receiver antenna using Hypothesis testing problem; meanwhile it is an estimator to estimate unknown signal parameters of the visible satellite, namely satellite PRN ID, code phase offset $\Delta\tau$, Doppler frequency offset $\Delta f_d$, initial carrier phase offset $\varphi_{rec}$ and navigation data bit sign. After determination of coarse values for synchronization parameters, the receiver passes these values to the tracking module to lock on the respective satellite signal.

## 3.1 Correlation and Coherent integration

Since the transmitted signal is embedded within noise in the transmission channel, a method called correlation is performed to detect the signal in the receiver. The correlation operation synchronizes the Rx signal with locally generated code. In general, two main types of correlation can be performed; the first correlator type relies on time domain techniques (TD) and second type performs the correlation in frequency domain (FD). Both correlator types have performance tradeoffs. TD correlators make use of massive parallel correlator or matched filter techniques and correlation is performed for each code phase. FD correlation is performed for all code phases in one step and this reduces the number of arithmetic operations using Fast Fourier Transform (FFT). For both correlation types, the process is repeated for all possible Doppler shifts. The input signal of acquisition process is the digital IF signal after analog to digital conversion (ADC) which can be defined as;

$$r_\mu = s_\mu p_\mu + n_\mu \tag{3-1}$$

Let $r_\mu$ be explicitly modeled as

$$r_\mu = Ac\left(t_\mu f_{c,sat} - \tau_{sat}\right) d\left(t_\mu f_{c,sat}\frac{f_{data}}{f_{c,0}} - \tau_{sat}\right) cos\left(2\pi\left(f_{IF} + f_{D,sat}\right)t_\mu - \emptyset_{sat}\right) + n_\mu \tag{3-2}$$

where c is the PRN code, $\tau_{sat}$ is the code delay in chips, $f_{data}$ is the data rate, $f_{c,sat}$ is the code rate in chips/sec of the satellite, $f_{IF}$ intermediate frequency in Hertz, $f_{D,sat}$ is the Doppler frequency, $t_\mu$ is the time of sample in seconds, $p_\mu$is the carrier component, $s_\mu$is the multiplication of signal amplitude, navigation data and the PRN code, $\emptyset_{sat}$ is the delay of navigation signal in radian, $n_\mu$ is the real valued white Gaussian noise, μ is the sample index and $A$ represents amplitude of the signal. The locally generated code samples are given by

$$c_\mu = c\left(t_\mu f_{c,sat} - \tau_{rec}\right) \tag{3-3}$$

Different techniques in time and frequency domains to correlate $s_\mu$ and $c_\mu$ are stated in the following sections. The first step of acquisition process is to down convert the IF signal into baseband. The down converted signal comprises the Doppler shift and carrier phase effect caused by the relative motion of the satellite and receiver. The baseband signal is given by;

$$r'_\mu = r_\mu exp\left(2\pi f_{IF} t_\mu\right) \tag{3-4}$$

where $t_\mu$ is the sample time. In the next step, decimation, namely low pass filtering, is performed in order to decrease the original sample rate since the required sample rate for acquisition is lower than the original sample rate. The decimated signal samples take the form of

$$r'_v = \sum_{\mu=vd}^{(v+1)d-1} r'_\mu \tag{3-5}$$

where d is the decimation factor and v represents the sample index after decimation. The decimated samples are resampled to adapt the length of samples to FFT length which have the form of $2^n$, where n is the FFT order. Thus, the resampled samples can be written as;

$$r'''_K = r''_{round\left(K\frac{f''_s}{f'''_s}\right)} \tag{3-6}$$

where $K$ is the sample index. Relatively,

$$f''_s = {f_s}/{d} \tag{3-7}$$

$$f_s''' = {L'''}/{T_{coh}} \tag{3-8}$$

where $f_s''$ is the decimation sample rate, $f_s'''$ is the sampling rate of resampling process, $T_{coh}$ is the coherent integration time, $L'''$ is the FFT length and $f_s$ is the sampling frequency. After the preprocessing step, correlation and coherent integration processes are performed over resampled samples.

Coherent integration time is integer multiple of PRN code periods. Coherent integration process can be applied after either time or frequency domain correlation. In Figure 3-1, coherent and non-coherent integration processes is represented. In non-coherent integration block, P denotes number of non-coherent integrations.

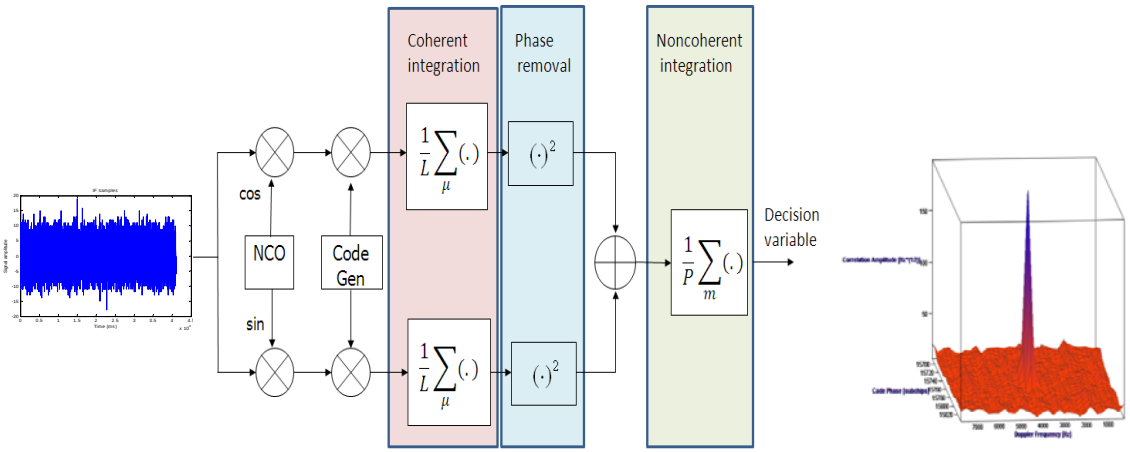


Figure 3-1: Coherent and non-coherent integration processes

As shown in Figure 3-1, acquisition is a two-dimensional search of code phase and Doppler frequency of the satellite signal until maximization of acquisition criterion is achieved. For this purpose, a range of code phase and Doppler frequency values and search step size are defined. For each code-frequency bin, the following criterion is calculated:

$$S(\hat{\tau}, \hat{f}_D) = \frac{1}{L}\sum_{\mu=1}^{L} r_\mu c(t_\mu - \tau)\exp(i2\pi f_D t_\mu) \tag{3-9}$$

where $L$ is number of samples.

The purpose of acquisition is to give coarse estimates of $\hat{f}_D$ and $\hat{\tau}$ for each visible satellite signal. When the locally estimated $\hat{f}_D$ and $\hat{\tau}$ values match with the received $f_D$ and $\tau$, then correlation output reaches its maximum value. In order to find the correlation peak, the circularly shifted resampled samples and complex conjugate of locally generated code are multiplied in FFT domain as outlined in the following algorithm:

**Input:** $S_K'''$ resampled samples
**Output:** $\hat{f}_D$ and $\hat{\tau}$
1: **for** *each Doppler bin* **do**
2: **for** *each FFT-frequency index* **do**
3: *ShiftedSamples = CircularShift(FFTresampled samples)*
4: *FFTResult[FFT-frequency index] = FFTlocal code[FFT-frequency index] x ShiftedSamples [FFT-frequency index]*
5: **end for**
6: *IFFTResult = IFFTFFTResult*
7: **for** *each code phase bin* **do**
8: **if** *current ( IFFTResult[code phase bin] ) > MaxPeak*
9: *MaxPeak = current ( IFFTResult[code phase bin] )*
10: *CodePhaseIndex= current(code phase bin)*
11: *DopplerIndex = current(Doppler bin)*
12: **end if**
13: **end for**
14: **end for**
15: *Maximum likelihood estimation of $\hat{f}_D$ and $\hat{\tau}$ depending on code phase and Doppler frequency index*

Algorithm 3-1: Correlation and Coherent integration

The operation of the acquisition unit is outlined in Figure 3-2. Correlation is performed for N-point FFT length of samples by multiplying circularly rotated FFT domain pre-processed signal and complex conjugate of FFT domain locally generated code. After despreading operation in frequency domain, N-point IFFT is used to convert the signal into time domain. The absolute values of N outputs of IFFT operation are considered to choose the largest peak and store the location of the peak as a code phase index and also store the amplitude of the peak and the index of corresponding Doppler bin. Then, the amplitude of the largest peak from the previous Doppler

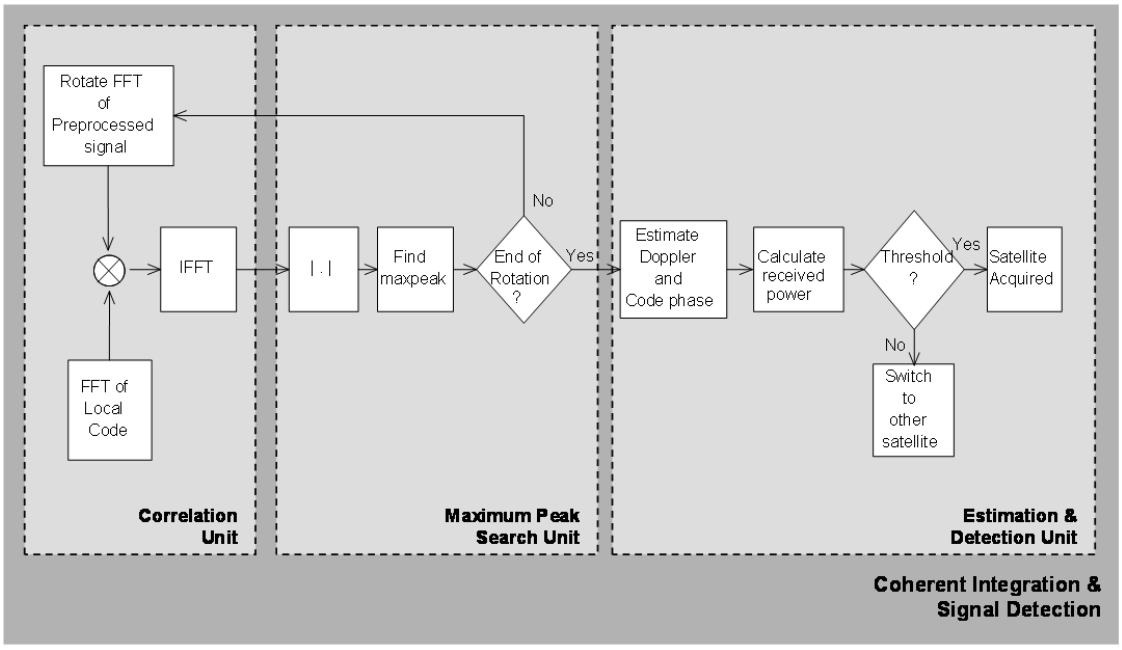


Figure 3-2: Flow diagram of acquisition unit

bin is compared with the current largest peak and the maximum is chosen. This process is repeated until all Doppler search bins are completed. After all Doppler bins are searched within the estimated interval, the Doppler frequency, code phase and received signal power are estimated by using maximum likelihood criteria. If the estimated received power exceeds the predefined threshold value, then signal detection is declared as *acquired*, otherwise acquisition is failed. Then a new satellite signal is considered and the process is repeated.

## 3.2 Maximum Likelihood Code Phase and Doppler Shift Estimator

Among parameter estimation techniques; so-called Minimum Mean Square Error (MMSE), Minimum Squared Error (MSE), Maximum Likelihood Estimation (MLE) and Bayes estimation, MLE is utilized for estimating unknown parameters from observations vector and minimizing the estimation loss. The MLE principle presents an optimal norm to obtain a parameter estimator that at least asymptotically achieves its lower variance bound (the Cramer-Rao Bound), if the sample size goes to infinity. Correspondingly, in the acquisition module signal parameters $f_D$, $\tau$, $\varphi$ and $A$ are estimated from likelihood cost function based on the MLE criteria. In MLE principle, it does not require a-priori information and assumes that unknown $f_D$, $\tau$, $\varphi$ and $A$ are constant over the

observation period, typically hundreds of ms or multiple seconds for high sensitivity receivers [39].

$$\hat{\tau},\ \hat{\omega},\hat{\varphi},\hat{A} = argmin_{\tau,\omega,\varphi,A}\sum_{\mu=0}^{L-1}\left(r_\mu - Ad_\mu c\left(t_\mu f_c - \tau\right)cos\left(\omega t_\mu + \varphi\right)\right)^2 \tag{3-10}$$

By extending (3-10), the coarse synchronization parameters yield:

$$\hat{\tau},\ \hat{\omega},\hat{\varphi},\hat{A}\ = argmin_{\tau,\omega,\varphi,A}\sum_{\mu=0}^{L-1}\left({r_\mu}^2 - 2r_\mu Ad_\mu c\left(t_\mu f_c + \tau\right)cos\left(\omega t_\mu + \varphi\right) + A^2 c\left(t_\mu f_c + \tau\right)^2 cos\left(\omega t_\mu + \varphi\right)^2\right) \tag{3-11}$$

After applying simplifications by neglecting constant terms in (3-11), this gives:

$$\hat{\tau},\ \hat{\omega},\hat{\varphi},\hat{A}\ = argmin_{\tau,\omega,\varphi,A}\left({LA^2C^2}/{2} - 2AR(\tau,\omega,\varphi)\right) \tag{3-12}$$

where $R(\tau,\omega,\varphi)$ is the correlation function in the acquisition process [39] and defined as

$$R(\tau,\omega,\varphi) = \sum_{\mu=0}^{L-1}\left(s_\mu D_\mu c\left(t_\mu f_c + \tau\right)cos\left(\omega t_\mu + \varphi\right)\right) \tag{3-13}$$

In order to estimate the signal amplitude, the derivative of A is applied onto (3-12) giving us the amplitude estimate as

$$\hat{A} = \frac{2R(\tau,\omega,\varphi)}{LC^2} \tag{3-14}$$

In the next step, code phase offset $\Delta\tau$ and Doppler frequency offset $\Delta f_d$ is estimated by taking the derivative of carrier phase offset $\varphi$ in the complex correlation function $R(\tau,\omega,\varphi)$.

$$\hat{\tau},\hat{\omega} = arg\ max_{\tau,\omega}\ |R(\tau,\omega)|^2 \tag{3-15}$$

In the module, the purpose is to find the maximum of the two-parameter correlation function in a certain search range. This is rather a time-consuming and computationally expensive process in the signal processing module of the GNSS receiver.

## 3.3 Long Coherent Integration Times

In standard GNSS receivers, a received signal sample $r_\mu$ is modeled for a short period signal [39].

$$r_\mu = \mathrm{A}c(t_\mu - \tau)exp\left\{i\left(\omega\left(t_\mu - \frac{L+1}{2f_s}\right) - \varphi\right)\right\} \tag{3-16}$$

where $L$ is the number of samples used in coherent integration time (CIT), A is the signal amplitude, $\tau$ is the code phase [s], $\varphi$ is the carrier phase [radians], $\omega$ is the angular frequency and Doppler [radian/s]. Eqn. (3-16) corresponds to a linear carrier phase dependency on time during CIT [39]. For long coherent integrations in a few second range, if linear phase model is considered, a number of physical effects limit the coherent integration time which are explained in section 5.3.1. These physical effects cause non-linear variations on the carrier phase which cannot be captured by the linear model. In that subsection, the effect of non-linear carrier phase variations in long CITs is explained.

The eqn. (3-10) tries to match the code phase and carrier phase of the locally generated signal to the code and carrier phase of the received signal. Thus the minimization can be rewritten for the code phase estimate as

$$\hat{\tau} = arg\,min\sum_\mu\left(\tau_{true,\mu} - t_\mu f_c + \hat{\tau}\right)^2 \tag{3-17}$$

and for the Doppler estimate as

$$\hat{\omega} = arg\,min\sum_\mu\left(\varphi_{true,\mu} - t_\mu\omega - \varphi\right)^2 \tag{3-18}$$

Both equations can be interpreted that the acquisition process is similar to a fitting procedure [40]. If we consider eqn. (3-17), the acquisition process fits the code phase $\hat{\tau}$ under the assumption that the code rate $f_c$ equals to the code rate of the received signal. For long CITs, it should be noted that this code rate $f_c$ needs to be adjusted according to the currently search Doppler bin. This procedure is called code Doppler compensation and is easily implemented when the replica signal is generated.

The most critical issue when long CITs are considered is the handling of residual carrier phase error. Analyzing eqn. (3-18) we recognize that the acquisition procedure can adjust two

parameters (namely ω and $\varphi$ ) in a way to optimally reproduce the true carrier phase of the Rx signal during the coherent integration interval. This can be seen as a linear fit, where the slope corresponds to the estimated Doppler frequency [40].

The offset $\varphi$ is a nuisance parameter of the acquisition process and is not considered further. The difficulty in coping with long CITs is that line-of-sight accelerations, receiver oscillator jitter and propagation channel effect cause non-linear variations of the carrier phase, which cannot be captured by the linear model. Those non-linear variations effectively cause a reduction of the correlation amplitude described by

$$L_{non-lin} = \frac{1}{T_{coh}} \left| \int_{t=0}^{T_{coh}} exp\{(\varphi_{true}(t) - t\omega - \varphi)\} dt \right|$$

$$L_{non-lin} = \frac{1}{T_{coh}} \left| \int_{t=0}^{T_{coh}} exp\{(\varphi_{res}(t))\} dt \right| \quad (3\text{-}19)$$

where $\Delta\varphi_{res}(t)$ is non-linear phase variations within the CIT. It is expected that if the non-linear phase variations are approximately smaller than *π/2* (or equivalently one quarter of the carrier wavelength which evaluates to about 6.1 cm in case of the L2 signal) then the correlation loss due to non-linear phase variations is small. If the non-linear phase variations are larger than π, the variations potentially cancel the correlation peak and the acquisition procedure may fail.

## 3.4 Statistical Requirements

In consideration of the requirement to acquire heavily attenuated signals in GNSS receivers, it is inevitable to integrate signals within 1s or more integration time. The modernized GPS and Galileo signals mostly provide longer ranging and lower power codes with respect to GPS L1 C/A signal. The long ranging code limits the integration time in case of integrating the code for the integer multiple of the code length. With short codes it is straightforward to integrate the codes for multiple numbers of code periods. However new signals provide greater cross correlation protection with reduced interference level, on the other hand acquisition time is increased. In acquisition, the performance of different signals in certain detection architecture is related to the parameters which settle the dimension of the search space. As acquisition is a two-dimensional search, in frequency dimension, the number of Doppler bins can be derived assuming FFT approach.

$$n_{f_d} = T_{coh}(f_{dmax} - f_{dmin}) \tag{3-20}$$

where $n_{f_d}$ is the number of Doppler bins.

The Doppler shift of the carrier $f_d$ is given by:

$$f_d = -f_{RF}\frac{(V_s - V_r)}{c} \tag{3-21}$$

Relatively, the maximum and minimum Doppler range can be settled as

$$f_{dmax} = V_{max}\, f_{RF}/c \tag{3-22}$$

$$f_{dmin} = V_{min}\, f_{RF}/c \tag{3-23}$$

where $f_{RF}$ is the radio frequency [Hz], $c$ is the speed of light [m/s] and $V_{min}$ and $V_{max}$ represents the minimum and maximum Doppler range rate [m/s] respectively. Likewise the Doppler effect on the carrier, there is also the code Doppler effect on the PRN code. This can be represented by:

$$f_{cd} = f_c f_d / f_{RF} \tag{3-24}$$

Since $f_{cd} \ll f_d$ and the difference is large, it is mostly ignored. However, for long CITs code Doppler effect is significant. Among existing civil signals, it is critical especially for GPS L2C pilot signal and this effect should be compensated in the receiver. For instance for a CIT of 1.5 s and code length of 3069000 subchip, $f_c$ be 2046000 subchip/s and the code Doppler shift becomes greater than 3 Hz if the Doppler frequency is 2 kHz and hence in that case acquisition process may fail.

The size of the time dimension depends on the ranging code length, FFT length and oversampling factor. The oversampling factor is the ratio of number of samples to the number of BOC subsamples, which means one chip consists of $N_s$ number of subsamples. In general, time bin step size of ½ chips is used due to the minimum precision requirement of ½ chips for code phase in the tracking process.

$$n_\tau = f_{chip} T_{PRN} N_s \tag{3-25}$$

where $n_\tau$ is the number of code delay bins, $f_{chip}$ is the chip rate[chip/s] , $T_{PRN}$ is the duration of one ranging code period [s] and $N_s$ represents the oversampling factor. As explained in the previous section, signals within different frequency bands have different data rates and code lengths causing a significant effect on the acquisition performance. In data channels, data bit duration limits $T_{coh}$. In Galileo E1 OS, each time the code period changes, the data bit sign varies as well whereas in GPS L1 C/A code, bit sign varies with a rate of twenty times of the code length. This requires new data bit mitigation techniques in the acquisition structure.

### 3.4.1 Threshold determination

The detection threshold is used to compare with received signal power to decide on the satellite signal detection. The threshold can be calculated for a determined false alarm probability ($P_{fa}$) by using two different approaches either from statistical derivations or simulations. Note that $P_{fa}$ is the probability of at least one noise bin in a search space exceeding a given threshold value $\gamma$. The amplitude of a noise bin is a central chi square distributed variable with $2m$ degrees of freedom and variance of $\sigma^2/m$ whereas the amplitude of a signal bin is a non-central chi-square distributed random variable with 2m degrees of freedom and variance of $\sigma^2/m$. $P_{fa}$ can be expressed as derived by [41].

$$P_{fa} = 1 - \frac{1}{2}\int_0^{\infty} \left(\frac{u}{E/\sigma^2}\right)^{\frac{m-1}{2}} e^{-\frac{E/\sigma^2+u}{2}} I_{m-1}\left(\sqrt{\frac{uE}{\sigma^2}}\right) P\left(m, \frac{u}{2}\right)^{N-1} du \tag{3-26}$$

where $u = mx/\sigma^2$, $I_k(x)$ is the modified Bessel function of the first kind of order $k$, $m$ is the number of non-coherent integrations, $\sigma$ is the standard deviation of noise, $\mathrm{P}\left(m, \frac{u}{2}\right)$ is the cumulative distribution function (CDF) of the maximum of noise bins amplitude using incomplete Gamma function and $N$ gives the number of search bins.

$$E = 2RT_{coh} \tag{3-27}$$

where $E$ is the signal energy after a coherent integration time of $T_{coh}$, $R$ is the autocorrelation function value.

The probability of detection can be defined as the probability of signal bin values exceeding noise bin values and the detection threshold $\gamma$. It can be written as

$$P_d(\gamma) = \int_{\gamma}^{\infty} \left(1 - P_{fa}(x)\right)^{N-1} f_A(x)dx \tag{3-28}$$

where $f_A(x)$ is the probability distribution function (PDF) of the signal bin using non-central chi square distribution and can be denoted as

$$f_A(x) = \frac{m}{2\sigma^2}\left(\frac{mx}{E}\right)^{\frac{m-1}{2}} e^{-\frac{E+mx}{2\sigma^2}} I_{m-1}\left(\frac{\sqrt{mxE}}{\sigma^2}\right) \tag{3-29}$$

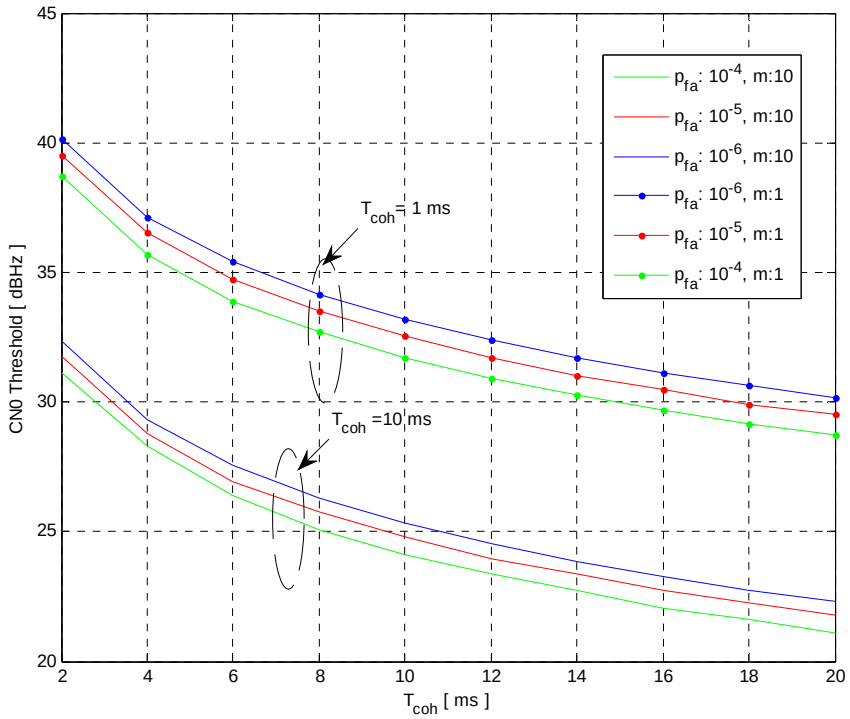


Figure 3-3: Threshold values as a function of coherent integration time

The model in (3-28) is extended to

$$P_d(\gamma) = \frac{1}{2}\int_{\frac{mq}{\sigma^2}}^{\infty}\left(\frac{u}{E/\sigma^2}\right)^{\frac{m-1}{2}} e^{\frac{E/\sigma^2+u}{2}} I_{m-1}\left(\sqrt{\frac{uE}{\sigma^2}}\right) P\left(m,\frac{u}{2}\right)^{N-1} du \tag{3-30}$$

where $P$ is the signal power in dBHz scale.

In Figure 3-3, the threshold values as a function of coherent integration time $T_{coh}$ by using different false alarm probabilities $P_{fa}$ and number of PRN code periods $m$ are represented. Practically, these threshold values could be set for determined CITs.

### 3.4.2 Sampling Requirements

Hereinbefore, the code phase $\tau$ and Doppler frequency $f_d$ are the main parameters to be coarsely estimated in the acquisition process. Code phase is a phenomenon caused by time misalignment of the received and locally generated code. Likewise, Doppler frequency is caused by the relative velocity between the transmitter and the receiver. The code phase can be written as

$$\tau = kT_{code} + \xi T_{chip} \tag{3-31}$$

where $T_{code}$ is the code period, $T_{chip}$ is the chip duration, $k$ is the number of code sequences, $\xi$ is the code phase uncertainty $\xi\epsilon(0, L)$. Let there be $L$ chips and $N$ samples in one code period of data, then the code phase resolution is $\Delta\xi = L/N$ chip/sample. The parameters of chip rate, sampling rate and signal modulation scheme determines the requirement of code phase resolution. The code phase resolution has an effect on signal power due to the sampling rate. This effect incurs an offset between the true peak index and the maximum peak index found in the correlation output as shown in Figure 3-4. The larger the true peak offset, the larger the signal power attenuation.

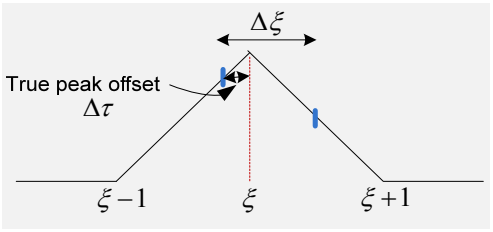


Figure 3-4: True peak offset on the correlation output due to the sampling rate [42]

$$|\Delta\tau| \leq \frac{\Delta\xi}{2} - 1 \tag{3-32}$$

where $\Delta\tau$ is the true peak offset.

$$G(\Delta\xi) = R(\Delta\tau) \tag{3-33}$$

where $R$ is the ACF.

Also the Nyquist criterion should be considered in the sampling process. Less sample rate w.r.t Nyquist rate causes further signal power losses. However, in the acquisition process the sample rate can be chosen less than or equal to the Nyquist rate and this is a reasonable assumption for the signal detection. In other words, it is not necessary to retrieve the whole information of the navigation signals and instead, it is sufficient to reconstruct the signal autocorrelation function [43]. This leads to a signal power loss of about the ratio of sample rate over Nyquist rate. Autocorrelation function is used to define the self-similarity of the signal versus delay and this is the reason why autocorrelation functions are the common usage in the synchronization process.

In terms of modulation scheme effect on code phase resolution, the BPSK modulation scheme requires 1 sample/chip resolution; whereas BOC modulation needs phase resolution of 2 sample/chip. The Doppler search space consists of bins and each bin covers a section of the frequency residual $\Delta f_d$. The time needed to acquire the signal is directly proportional with number of bins. Doppler resolution (bin width) is the reciprocal of $T_{coh}$, therefore increase in $T_{coh}$ reduces the width of the main lobe of sinc function and causes an increase in number of Doppler bins. Doppler frequency bin width has an effect on the signal power due to $T_{coh}$. This is related to the frequency response approximation of the correlator gain given by [42]

$$G(f_d) = \left|\frac{sin(\pi f_d T_{code} k)}{\pi f_d T_{code} k}\right|^2 \tag{3-34}$$

In the following figure, the signal power loss considering different $T_{coh}$ (equals to the product of $k$ and $T_{code}$) values are illustrated. Obviously, the power of the signal is concentrated in the center of the frequency band and the PSD has nulls at the multiples of the code chip rate. A larger $T_{coh}$ causes a narrower main lobe of sinc function and this implies an increase in the number of Doppler bins.

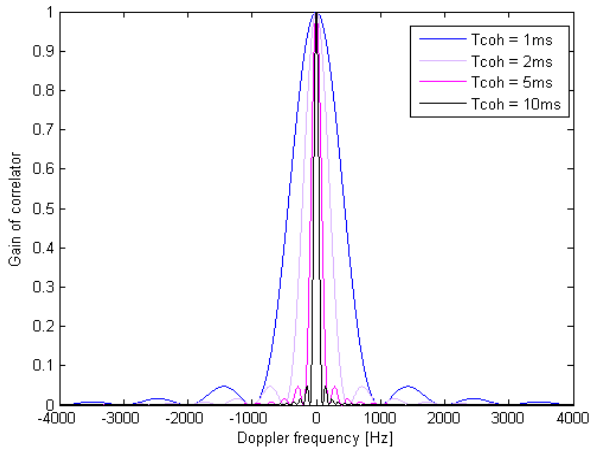


Figure 3-5: Correlator gain as a function of coherent integration time

### 3.4.3 Acquisition Search Range

The signal acquisition is a two dimensional search process as shown in Figure 3-6. The Doppler search space consists of bins and each bin covers a section of the frequency residual $\Delta f_d$. Thus, for a Doppler search range of $\Delta F_d$, there are $\Delta F_d / \Delta f_d$ number of Doppler bins. In code phase search space, if $L$ chips exist in one code period of data, then there are $L$ minimum different code phases to be searched. However, usually a certain oversampling factor is used to increase the code phase resolution. The number of search bins $N_s$ depends on three factors: length of code period, the number of Doppler bins and the oversampling factor is derived as

$$N_s = L\left(\frac{\Delta F_d}{\Delta f_d}\right) \tag{3-35}$$

where $\Delta F_d$ is the Doppler search range, $\Delta f_d$ is the Doppler bin width and $L$ is the number of chips which exist in one code period of data multiplied with the oversampling factor.

The number of search bins can be reduced by providing external aiding information about code phase, Doppler frequency and navigation data. Typically the external data contains the initial position estimate, satellite ephemeris, reference frequency and time. The reduction of the search space would increase the sensitivity of the receiver in terms of possibility to prolong the CIT and also a decrease in the probability of false alarm.

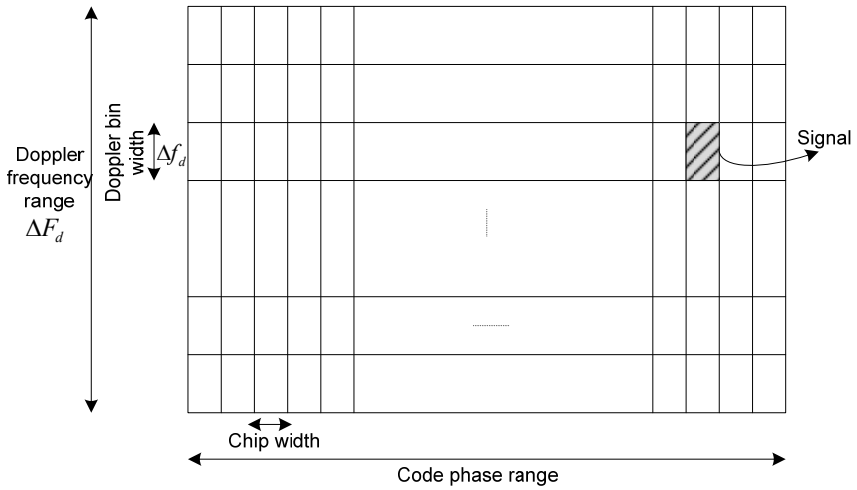


Figure 3-6: Acquisition search process

### 3.4.4 Reduction of Doppler bins

The number of Doppler bins is directly related to $T_{coh}$ since the Doppler bin width is the reciprocal of $T_{coh}$. If the Doppler bin width $\Delta f_d$ is large, then this reduces $N_s$. Reduction of Doppler bins using external aiding information requires high stability clocks to obtain the reference time and frequency for estimation of Doppler frequency. This can be provided by cellular base stations which have high quality oscillators. It can also be obtained from a local crystal oscillator, however in this case the reference frequency may not be accurate enough to estimate the Doppler frequency.

### 3.4.5 Reduction of code phase bins

The possibility to reduce the code phase search range is critical mostly in the presence of long PRN codes (e.g. L2C pilot). In this case, the code length may strain the receiver to integrate the signal for unnecessarily long integration time. Therefore, integrating the signal without completing the whole code length (without damaging the correlation properties of the code under certain limits) could be possible. Reduction of number of code phase bins using reference time from external system requires a synchronized network such as CDMA cellular telephone systems.

Otherwise, with asynchronous networks such as GSM and UMTS, the code phase estimate is not always accurate enough due to the lack of system components to synchronize the cellular network to the GNSS system time. The code phase search range can be reduced to a few chips in urban conditions with accurate reference time provided from a synchronous network. The more accurate reference time (within a few microseconds) can be provided by using pilot signals. Besides, a few hundred microsecond time accuracy would still be enough to coarsely estimate the secondary (overlay) code phase [44].

### 3.4.6 Data bit transition effect

In data signals case, during CIT, data bit transition may occur causing 180° carrier phase shift. Data transitions are synchronized to the code periods and occur only once every navigation data bit duration. In other words, if the transition occurs in a certain one millisecond of data, the successive one data bit duration of data cannot contain another data bit transition. For instance, to acquire the GPS L2CM signal, 20 ms of data are compared. During this period with a probability of 50%, a data bit transition may occur synchronized with the beginning of the PRN code. This effect can be compensated by multiplying the code samples with half of complex *sine/cosine* wave during acquisition process. The worst case of this effect appears when the data bit transition occurs at half the length index of the code length. The data bit reversal needs to be accounted in the PRN code, since it gives performance degradation when acquisition is applied directly to the algorithm which does not take into account the effect of data bit transition.

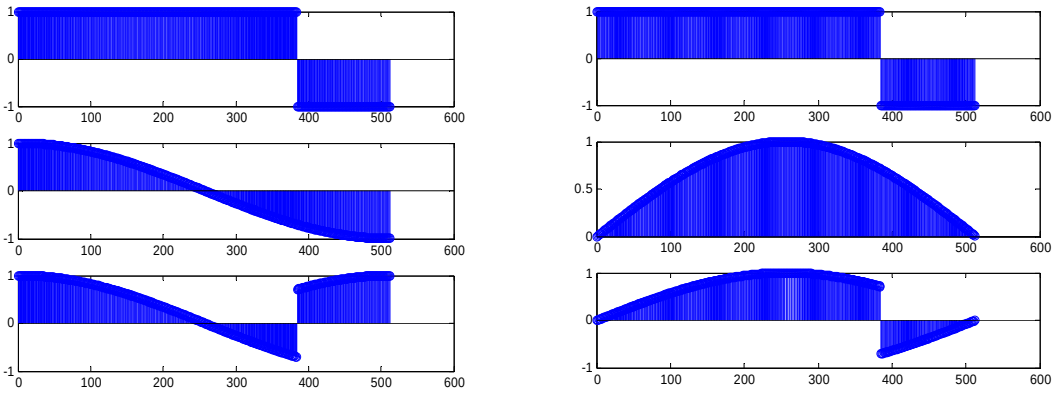

Figure 3-7: The navigation data bit transition

The effect of one half of a complex sine/cosine wave is represented in Figure 3-7. The navigation data bit is represented at the upper plot, the real-part is in the middle-left and the imaginary-part is shown in the middle-right plot of a half of complex sine/cosine wave. The real-part and the imaginary-part of the multiplication of navigation data bits and half sine/cosine function are represented at the lower part of the plot.

## 3.5 Dual Channel Acquisition

Modernized GNSS signals within various frequency bands have different data rates, code lengths and composed of two components, namely data and pilot. In data channels, data bit duration limits $T_{coh}$. In case of pilot channels, the secondary code causes the same effect as the navigation data bit. Only difference is that the secondary code is known and once the receiver is synchronized with the secondary code, it could be removed from the Rx signal. With the presence of pilot signals, the signal acquisition structure can be implemented in two ways:

- Either the data or pilot signal acquisition (especially pilot signal acquisition is applied which provides long coherent integrations and data signal is ignored)
- Both data and pilot (dual) signal acquisition is processed and signal energies are summed providing an increase in the signal power and a decrease in the threshold value

The signal detection process is simplified with pilot signals due to the absence of navigation data bit providing long CITs if the secondary code is removed from the Rx signal. This provides gain for high sensitivity applications since sensitivity depends mainly on $T_{coh}$. However, the main problem on pilot signal acquisition is the large search space dimension and an increase on the false alarm probability. The search dimension could be reduced by using assistance data to drop off the Doppler range. In the presence of data and pilot signals, one solution to acquire the visible satellite signal is to process the pilot signal only and ignore the data signal. Even processing either data or pilot channel is sufficient to detect the visible satellite signal; dual channel acquisition is used to increase the Rx signal power. Both channels are multiplexed before transmission to the wireless medium so that they are subjected to the same Doppler effect and the time delay. In this case, when processing both channels the correlation output would be doubled and theoretically 3 dB gain (if the power split is 50% - 50% between data and pilot channels) is achieved over the processing of single channel only. On the other hand, it requires double number of correlators causing an increase in the implementation complexity.

Table 3.1: Single versus dual channel acquisition difference

| Single channel | Dual channel |
|---|---|
| Rx signal is correlated with either data or pilot signal local code | Data and pilot signals experience the same transmission channel, hence have the same time delay and Doppler frequency |
| Only half of the available power is used | Reliable signal detection using all available power |
| Lowest computational load | The required computational load depends on the use of the "sign recovery" in the method |

In general, three different methods are studied to detect the dual channel signal. These are:

- *Non-coherent combining*
- *Differentially coherent combining*
- *Coherent combining*

At the receiver, the relative sign between data and pilot signals is not known due to the presence of navigation data and secondary codes. The last method given above takes into account the sign recovery. One of the proposed dual channel acquisition techniques ignoring the sign recovery is the classical non-coherent combining method [45], [46]. The Rx signal is correlated with data and pilot components separately and then correlation outputs are squared and combined.

$$T_{nc}(f_d,\tau) = |R_D(f_d,\tau)|^2 + |R_P(f_d,\tau)|^2 \tag{3-36}$$

where $R_D$ and $R_P$ are respectively cross correlations of the input signal with the locally generated code of the data and pilot signals modulated by $\tau$ and shifted by $f_d$. In the conventional differentially coherent combining method, the current sample after coherent integration is multiplied with the complex conjugate of the previous sample in complex domain and then products are accumulated for the number of non-CITs. In this case, data and pilot signals are used instead of two consecutive samples. Due to phase difference between data and pilot signals a modification is applied to the conventional differentially coherent combining method. Hence, only the imaginary part of the product of signals is considered.

$$T_{dc}(f_d,\tau) = \left|Im\left(R_D(f_d,\tau)R_P^*(f_d,\tau)\right)\right| \tag{3-37}$$

where $R_P^*$ is the complex conjugate of the cross correlation of the Rx signal with the pilot replica code modulated by $\tau$ and shifted by $f_d$.

Another dual channel acquisition method proposed is the coherent combining [47] and in this scheme, the Rx signal is correlated with two versions of both signals (summed data and pilot replicas, subtracted data and pilot replicas) and the maximum of the cross correlations is decided as the correct one.

$$T_{sc}(f_d, \tau) = max(|R_{D+P}(f_d, \tau)|^2 + |R_{D-P}(f_d, \tau)|^2) \quad (3\text{-}38)$$

where $R_{D+P}$ and $R_{D-P}$ are the cross correlations of the summed and subtracted data and pilot replica codes shifted by $\mathrm{f_d}$ and modulated by $\tau$. Among all these methods,

- For low level $C/N_0$, the sign recovery is not reliable and hence the performance of coherent and non-coherent combining methods gives the same performance and differentially coherent method has similar performance as well [48].
- For high level $C/N_0$, the coherent combining method outperforms other methods but leads more computational load according to the first two methods due to the search on the sign combinations.

## 3.6 Modulation Scheme Effects

In general, in order to detect the main peak of the ACF, the step size to search time bins should be half of the width of the main peak. In case of a BPSK modulated signal, the search time bin step value is selected as half chip. In BOC modulated signals it should be smaller to detect the main peak and it is around 0.35 chip. Increasing the time bin step value deteriorates the performance because the probability to find the correct peak decreases. However, decreasing the time bin step size increases the search space since the complexity on search space is inversely proportional with time bin step size. Considering relative Rx signal power levels of Galileo signals with various modulation schemes, the detection curves with respect to $C/N_0$ is presented in Figure 3-8 and the related integration parameters for the simulations are tabulated.

Table 3.2: Assumptions for sensitivity with various modulation schemes for Galileo signals

| Signals | Rx signal power [dBW] | Signal bandwidth [MHz] | Code phase range [chips] | Integration parameters |
|---|---|---|---|---|
| E1b-CBOC(6,1,1/11) | -160 | 14 | [-1/28, +1/28] | 4x5000 |
| E5a- BPSK(10) | -158 | 20 | [-1/4, +1/4] | 20x1000 |
| E5b-BPSK(10) | -158 | 20 | [-1/4, +1/4] | 4x5000 |
| E6a-BOC(10,5) | -155 | 30 | [-1/12, +1/12] | 10x2000 |

The main difference between GPS and Galileo signals is the Binary Offset Carrier (BOC) modulation scheme used in Galileo E1 signal which provides better spectral separation to GPS signals. Compared with BPSK ACF, main lobe of the BOC modulation is narrower and besides there exist two side peaks which causes ambiguity within 2 chip interval and challenges in the acquisition process. In the literature, three different techniques take part to overcome the ambiguity on the envelope of BOC modulation challenge, namely *sideband technique* [18], [19], *BPSK-like technique* [20], [21] and *unsuppressed adjacent lobes (UAL)* [23].

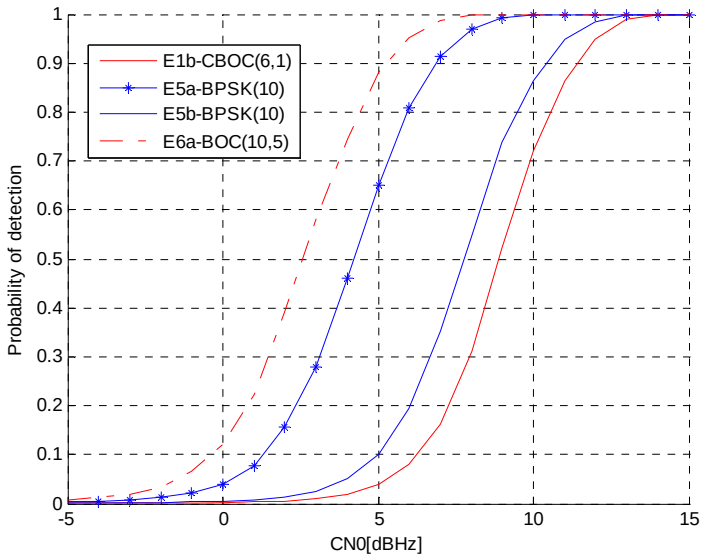


Figure 3-8: Probability of detection versus $C/N_0$ for signals using the scenario on Table 3.2 signals

## 3.7 Time Domain Acquisition

In GNSS receivers, in order to perform the correlation of the incoming signal with a locally generated code over many frequency and code phase bins simultaneously, signal processing units contain different implementation approaches. They could be either in bank of correlators (taps), so-called "massive parallel correlators" or bank of matched filters. Both approaches provide equivalent results. The correlation operation is performed entirely in TD. Though with TD correlators the computation time is excessively long, they are widely used due to the simplicity of the algorithm and are implemented usually in hardware. The challenging feature of TD correlators is that limited number of code delays can be processed. A massive parallel correlator has the ability to at least correlate for the entire code delay domain of one satellite. In order to search more satellite signals in parallel, receivers comprise even more correlators. When incoming signal is weak, then with increased number of search bins, it is impractical to use massive correlators. Accordingly, FD techniques are preferred in receiver implementations due to less computational complexity and cost of the receiver. The generic massive parallel correlator for one satellite signal with *N* different chip shifts is illustrated in Figure 3-9.

$$y_n = \frac{1}{T_{code}} \int_0^{T_{code}} s(t) c_n(tf_c - \tau_n) dt \tag{3-39}$$

where $c_n$ is the *n*-chip shifted local code.

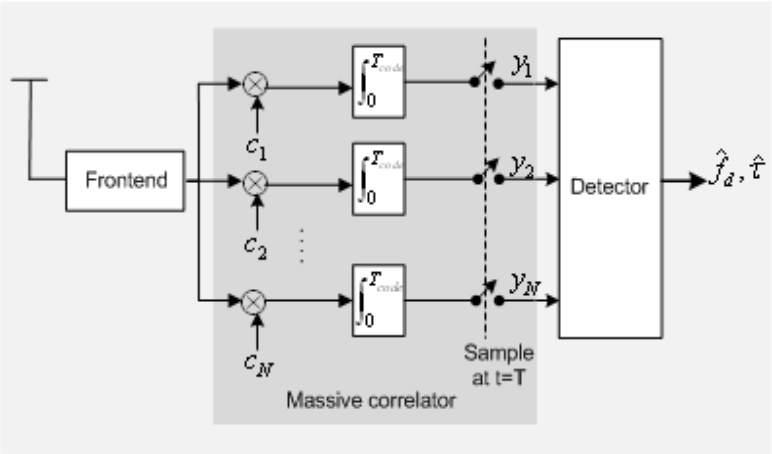


Figure 3-9: Generic massive parallel correlator

Another TD correlator is the matched filter which correlates a known PRN signal for optimum detection in AWGN. In general, the matched filter with an impulse response of $h(t)$ is equal to time reversed and shifted impulse response of the transmitted signal. The matched filter is realized as FIR filter such that the filter coefficients are equal to the desired code sequence and the number of delay units that is equal to code sequence length. A bank of matched filters coherently combines the samples to estimate the delay and Doppler using a sliding approach as shown in Figure 3-10. The output of the front-end is passed through a filter with impulse response of h(t), $0 \leq t \leq T_{code}$ and its output is sampled at $T_{code}$.

The convolution operation $(*)$ of the impulse response of the optimum matched filter with the Rx signal gives the idea of the matched filter.

$$r(T) = h_{opt}(t) * s(T_{code}) \tag{3-40}$$

where $h_{opt}$ is the optimum matched filter. The impulse response of the filter is the time reversed shifted version of the transmitted signal.

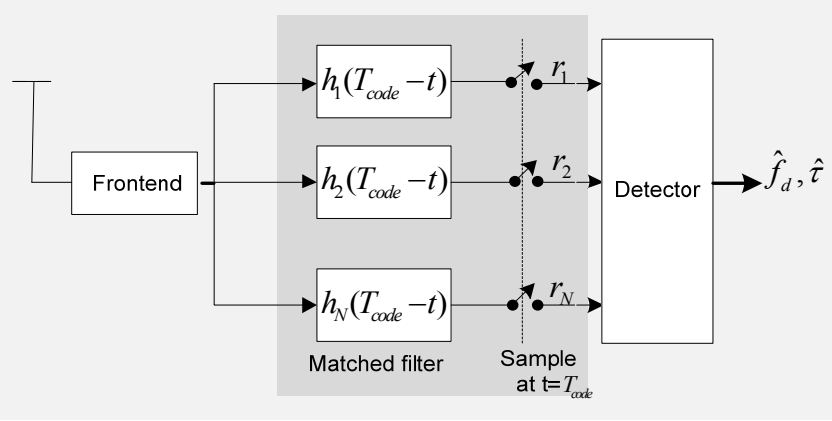


Figure 3-10: Matched filter

$$h_n(t) = h_{opt}(t) = r(T_{code} - t) \qquad 1 \leq n \leq N \tag{3-41}$$

where $r(t)$ is the transmitted signal. The matched filter has an important property that it maximizes the signal power to noise ratio (SNR) at the output of the FIR filter when the signal is corrupted by AWGN.

## 3.8 FFT Acquisition

Briefly, FFT acquisition process is outlined in Figure 3-2. The time convolution theorem states that correlation in TD is equal to multiplication in FD in which either the locally generated code or the Rx signal is conjugated. One shortage of FD methods is that FFT provides approximate results because of coefficient rounding, where TD correlations yield accurate outputs. The first FD correlation technique is the *circular correlation* where the multiplication of FFT of the Rx signal with a complex conjugated FFT of the local signal or vice versa. The correlation output will be

$$R = IFFT\{FFT(r).\overline{FFT(c)}\} \tag{3-42}$$

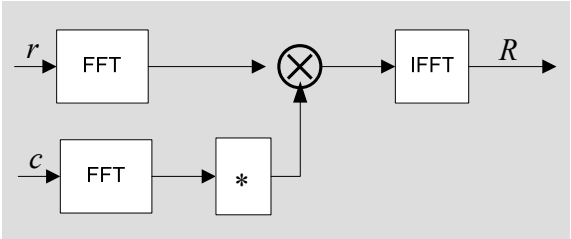


Figure 3-11: Block diagram of circular correlation

The second method is the *zero padded FFT* where correlation is performed for two code periods of samples by multiplying the FFT of a zero padded c with r̃. The extended local code is created by appending one code period of zeroes after one code period of PRN code. This operation could be applied to the local code in order to diminish the correlation degradation due to the navigation data bit transition. It is certain that navigation data bit transition exists in two code periods. *Frequency search by spectral shifting* is the third method where spectral shifting is a direct manipulation on the FFT spectra of one of the sequences. For different number of Doppler bins, $f_d$ search is performed in spectral shifts of $\Delta f_d$ . Frequency domain signals are multiplied in a certain Doppler bin and transformed into time domain. For the following Doppler bin, the signal in frequency domain is circularly rotated for a certain $\Delta f_d$ and multiplied with the other signal in frequency domain. On the contrary to the conventional FFT acquisition scheme, in *post correlation FFT,* correlation is performed in TD and then FFT is used, in this way, a fine Doppler frequency search is performed in one step in parallel.

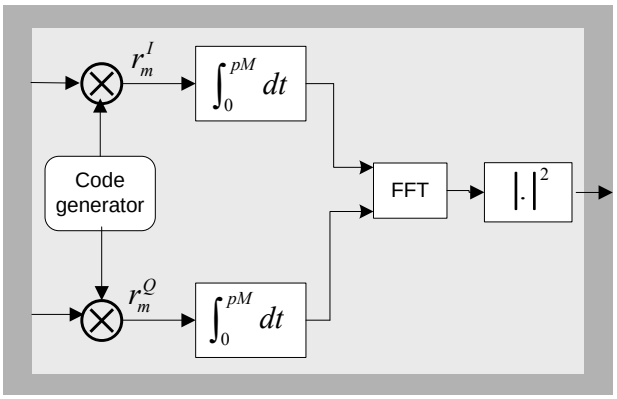


Figure 3-12: Block diagram of post correlation FFT

One disadvantage of this method is the dependency on the frequency resolution. In this way, if the actual Doppler frequency falls into the center of Doppler bins rather than in one of the Doppler bins, than signal power is spreaded into neighboring bins and leads to degradation on the peak. Further differences between conventional FFT search and post-correlation FFT are described in [3].

## 3.9 Sensitivity Limits

Acquisition sensitivity is the minimum signal power level that the signal is acquired. The reception sensitivity can be generally increased by extending the CIT. Doubling the coherent integration and non-coherent integration times, acquisition gives sensitivity gain of around 3 dB and 1.5 dB respectively. Note that for search range calculations, serial search acquisition is considered. With modernized GPS and Galileo signals, the computational burden to find coarse estimates of $f_d$ and $\tau$ became higher due to long code periods requiring increased number of samples. With increased number of search bins, the receiver searches through the entire code length for a fixed code phase resolution and also through Doppler frequencies with the increment of $1/T_{coh}$, then complexity increases further. In frequency search, the relative number of Doppler bins compared to different signals depends on $T_{coh}$ and carrier frequency $f_{RF}$. The code period and the number of PRN code sequences has a linear dependency with $T_{coh}$. As $T_{coh}$ increases, the number of Doppler search bins also increases. This triggers an increase in the false alarm probability, so that assistance data is required to allow reducing the Doppler search space. Since Doppler frequency bins are related to $T_{coh}$, corresponding $T_{coh}$ values are tabulated in Table 3.6.

The number of search bins is the multiplication of number of code phase bins and Doppler frequency bins. For BPSK and BOC modulated signals, the code phase resolution of 1 sample/chip and 2 samples/chip are considered respectively. If the correlation properties of the code remains within acceptable ranges, then CIT can be selected as a non-integer multiple of the code period and this would shortens the computational burden and the acquisition time as well. With short code lengths as in the case of GPS L1 C/A, the CIT can be extended over several code periods. However, in case of long code lengths, the coherent integration could be applied without any need to complete the full code period. In Table 3.3, complexity of signals in terms of number of search bins (Doppler frequency and code phase bins) is tabulated for a Doppler search range of $\pm$ 5 kHz for various scenarios namely S1 indicating soft indoor, S2 implies deep indoor and S3 refers to the urban environment scenario.

Table 3.3: Acquisition search complexity of GNSS signals

| Signals | Code phase Bins | Doppler frequency bins | | |
|---|---|---|---|---|
| | | S1 | S2 | S3 |
| L1 C/A | 1023 | 200 | 200 | 200 |
| E1 Data | 8194 | 40 | 40 | 40 |
| E1 Pilot | 204600 | 10000 | 100000 | 200 |
| L2 CM | 20460 | 200 | 200 | 200 |
| L2 CL | 1534500 | 10000 | 100000 | 200 |
| I5 Data | 10230 | 100 | 100 | 100 |
| Q5 Pilot | 204600 | 10000 | 100000 | 200 |
| E5a Data | 204600 | 200 | 200 | 200 |
| E5a Pilot | 1023000 | 10000 | 100000 | 200 |
| E5b Data | 40920 | 40 | 40 | 40 |
| E5b Pilot | 1023000 | 10000 | 100000 | 200 |

If the correlation properties of the code remains within acceptable ranges, then CIT can be selected as a non-integer multiple of the code period and this would shortens the computational burden and the acquisition time as well. With short code lengths as in the case of GPS L1 C/A, the CIT can be extended over several code periods. However, in case of long code lengths, the coherent integration could be applied without any need to complete the full code period.

### 3.9.1 Simulation Results

The acquisition structure to process new civil GNSS signals is conceptually shown in Figure 3-13. For the simulations of all signals, the acquisition performance is analyzed using the structure in Table 3.4. In the simulations, the code delay $\Delta\tau$, the Doppler frequency $\Delta f_D$ and the carrier phase $\emptyset_{rec}$ parameters are considered as uniformly distributed random variables. For uniformly distributed random varieties, the range of code phase is illustrated in Table 3.4 and the range of frequency and carrier phase are written in eqn. (3-43) and (3-44).

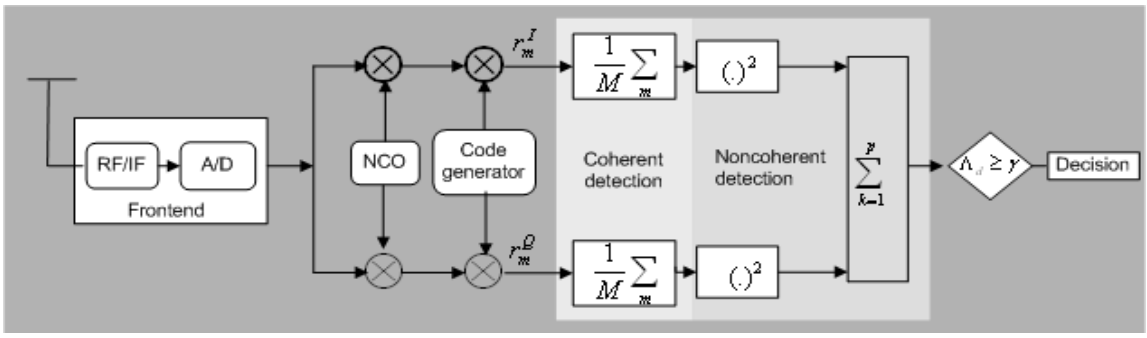


Figure 3-13: Block diagram of standard signal detection

Table 3.4: Code phase ranges

| Signals | Code phase |
|---|---|
| GPS L1CA/L2, Galileo E1 | $\Delta\tau \in [-1/20, +1/20]$ |
| GPS L5, Galileo E5a/E5b | $\Delta\tau \in [-1/48, +1/48]$ |
| Galileo E5 (AltBOC) | $\Delta\tau \in [-1/140, +1/140]$ |

$$\Delta f_D \in \left[-\frac{1}{2T_{coh}}, +\frac{1}{2T_{coh}}\right] \quad (3\text{-}43)$$

$$\emptyset \in [0, 2\pi] \quad (3\text{-}44)$$

The performance of specified signals are evaluated for three different scenarios as a function of dwell time, signal bandwidth, user dynamics and estimated Rx signal power levels. In the simulations when considering GPS L2C data and L2C pilot signals, the $C/N_0$ offset value compared to GPS L1 C/A code is taken as -1.5 dB and for Galileo E5b data and pilot signals, the $C/N_0$ offset value is taken as +0.5 dB. The signals analyzed are bandlimited to 10 MHz for

BPSK(1) and BOC(1,1) signals including main lobe and two side lobes, 24 MHz for BPSK(10) signals. Detection probabilities are plotted against $C/N_0$. The threshold is chosen for a fixed false alarm probability of 0.1% for all signals. The CIT (the first value) and number of non-coherent integrations, $p$, (the second value) are given in Table 3.6. The $T_{coh}$ value is determined for the duration of one navigation data bit for data signals. However, in terms of pilot signals $T_{coh}$ is set as the maximum CIT (for GPS L2CL signal, though one code period lasts for 1.5 s, the maximum $T_{coh}$ is considered). The combination of $T_{coh}$ and $p$ is same for all pilot signals; however for data signals same signal averaging time with different $T_{coh}$ and $p$ is used.

Table 3.5: Scenario definitions

| Indoor cases | Definition | $C/N_0$ for acquisition [dBHz] | Max. coherent integration time [s] | Dwell time [s] |
|---|---|---|---|---|
| S1 (Soft indoor) | User has been in upper floors of the building | 16.11 | 1 | 2 |
| S2 (Deep indoor) | Away from window and first or mid-store of the building. Signal strength is weak. There is no LOS. | 2 | 10 | 100 |
| S3 (Urban) | User is inside partially-obstructed places or very close to buildings | 25 | 0.02 | 1 |

Table 3.6: GNSS signal coherent and non-coherent integration parameters for different scenarios

| Signals | S1 | S2 | S3 |
|---|---|---|---|
| | Coherent integration time x Number of non-coherent integ. | | |
| GPS L1 C/A | 20 ms x 100 | 20 ms x 5000 | 20 ms x 50 |
| E1 Data | 4 ms x 500 | 4 ms x 25000 | 4 ms x 250 |
| L2C Data | 20 ms x 100 | 20 ms x 5000 | 20 ms x 50 |
| I5 Data | 10 ms x 200 | 10 ms x 10000 | 10 ms x 100 |
| E5a Data | 20 ms x 100 | 20 ms x 5000 | 20 ms x 50 |
| E5b Data | 4 ms x 250 | 4 ms x 25000 | 4 ms x 250 |
| Pilot signals | 1 s x 2 | 10 s x 10 | 20 ms x 50 |

Detection probabilities are plotted against the estimated received signal power level ($C/N_0$). The threshold is chosen for a fixed false alarm probability of 0.1% for all signals.

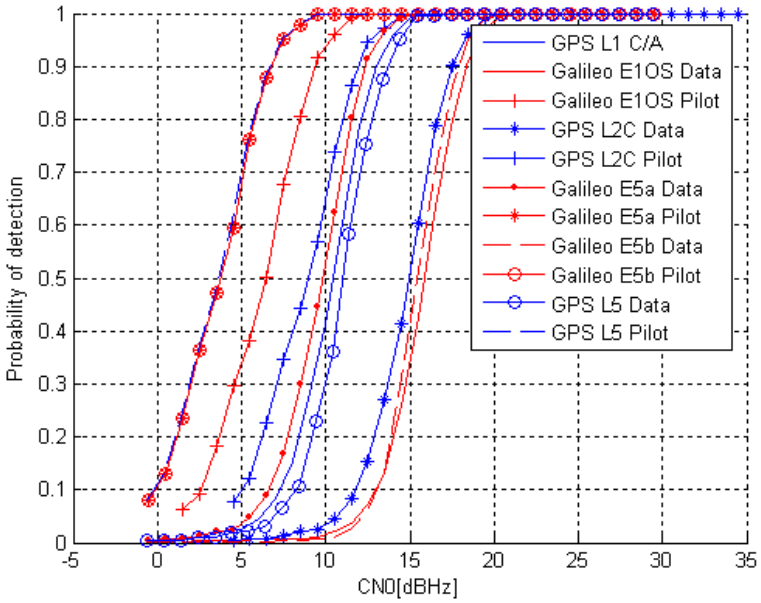


Figure 3-14: Detection probability against estimated Rx signal power with different signals for scenario S1 with static user

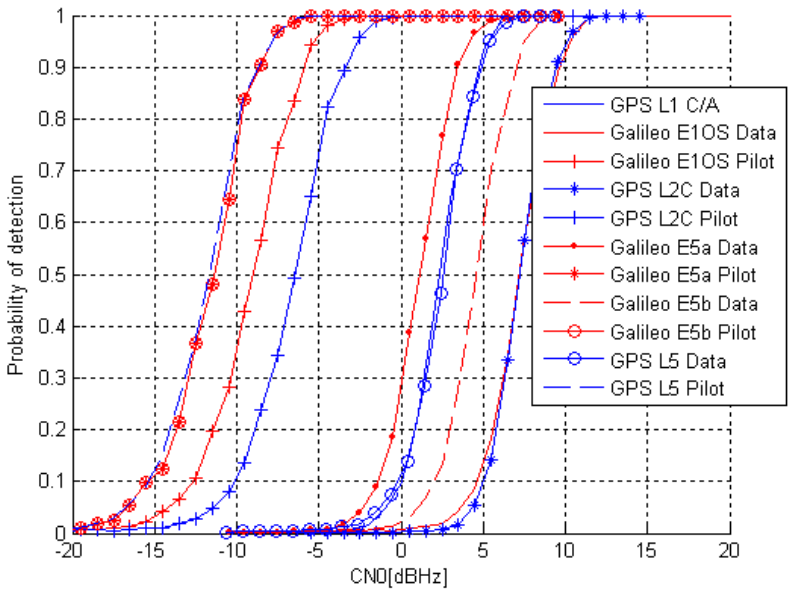


Figure 3-15: Detection probability against estimated Rx signal power with different signals for scenario S2 with static user

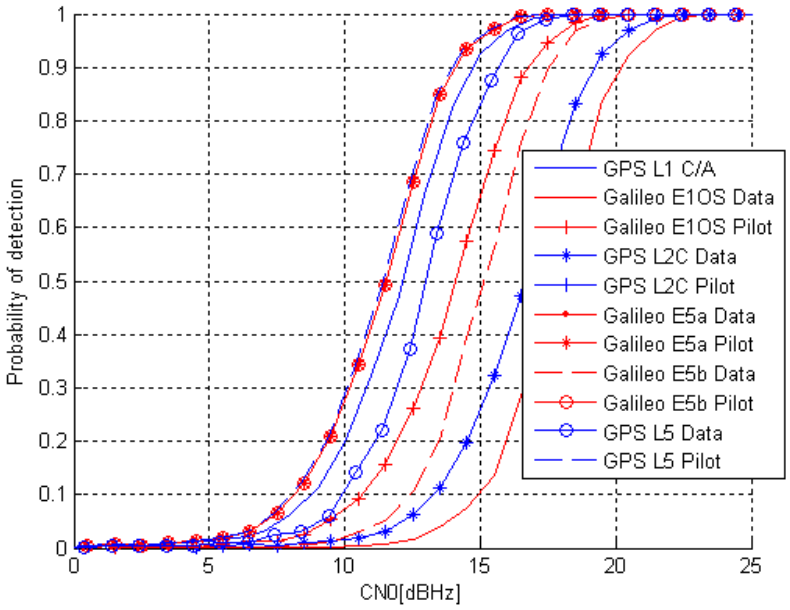


Figure 3-16: Detection probability against estimated Rx signal power with different signals for scenario S3 for static user

In Table 3.7, sensitivity levels of all specified signals for a detection probability of 90% and a false alarm probability of 0.1% are tabulated.

Table 3.7: Estimated Rx signal power levels in [dBHz]

| Signals | S1 | S2 | S3 |
|---|---|---|---|
| GPS L1 C/A | 12.974 | 4.75 | 14.72 |
| E1 Data | 18.39 | 9.6525 | 20.242 |
| E1 Pilot | 9.34 | -5.9 | 16.79 |
| L2C Data | 17.47 | 9.41 | 19.228 |
| L2C Pilot | 11.945 | -3.378 | 19.228 |
| I5 Data | 14.85 | 5.874 | 16.56 |
| Q5 Pilot | 7.54 | -7.3 | 15.22 |
| E5a Data | 13.509 | 4.59 | 15.319 |
| E5a Pilot | 7.642 | -7.2 | 15.319 |
| E5b Data | 18.34 | 8.214 | 18.257 |
| E5b Pilot | 7.642 | -7.2 | 15.319 |

## 3.10 Conclusion

Plots in Figure 3-14 - Figure 3-16 present the detection performance of specified signals considering estimated Rx signal power levels listed in Table 3.7. In scenarios, different high sensitivity simulations are performed due to indoor environment requirements. In figures, pilot signals show better detection performance than data signals. Pilot signals are used for the same scenario so that among pilot signals the sensitivity gain depends on the nominal signal power level and modulation scheme of the signal. As can be seen the difference in sensitivity gain among data and pilot signals is caused by the use of shorter CIT which is limited by the navigation data bit in data signals. In S1 scenario, with an averaging time of 2 s, although GPS I5 signal having a higher nominal signal power, presents a lower margin than some of data signals. Within L1 C/A, L2C data and E5a data signals that are running for the same scenario, Galileo E5a data signal gives the best sensitivity gain of about 0.6 dB. In terms of pilot signals, L2C pilot has the least sensitivity of around 11.94 dB. In S2 scenario, 100 s dwell time is used to achieve an ultra-high sensitivity gain from Rx signals.

Galileo E1 OS data signal has the minimum $T_{coh}$ with the largest number of non-coherent integrations having the same dwell time with all signals; however it reveals the worst sensitivity among all signals. Obviously, this is due to the stabilization of gain and squaring loss when using large number of non-coherent integrations hereby providing no gain. On the average, in ultra-high sensitivity case, pilot signals can be acquired about 10 dB lower than matching data signals. In S3, the lowest dwell time of 1 s is used for all signals so that the sensitivity levels between data and pilot signals are small and the average sensitivity level of 17 dB is achieved. For all scenarios, it can be concluded that the difference in signal sensitivity levels becomes higher when the CIT is large. Since CIT specifies the main sensitivity gain. With pilot signals, the sensitivity gain is higher compared to data signals of about 10 dB for large signal dwell time with longer CIT. In case of small dwell time, the sensitivity gain with pilot signals is about 5 dB compared to data signals. However, in pilot signal acquisition it is critical to reduce the search space by assistance data since sensitivity depends not only on CIT but also search space dimension because of the false alarm probability increase.

# CHAPTER 4. DETECTORS IN GNSS RECEIVERS

In general, the detection problem is to decide whether the GNSS signal is embedded in the background noise or if only noise is present. The detection analysis is based on binary hypothesis tests $H_0$ and $H_1$. The decision on $H_1$ when $H_0$ is true and vice versa causes a false alarm. In the presence of only noise, for a given probability of false alarm, the threshold value $\gamma$ is computed with hypothesis $H_0$. Then in the presence of signal, using hypothesis $H_1$, the probability of detection is computed.

*Hypothesis* $H_0$: Only Gaussian distributed white noise is considered without presence of the desired signal. Then, $\gamma$ is computed for a given desired probability of false alarm ($P_f$).

$$H_0: s_l = n_l \qquad l = 0,1,2,\dots,L-1 \tag{4-1}$$

where $s_l$ is the Rx signal sample, $n_l$ is the noise sample and $L$ is the number of samples used for Hypothesis decision.

*Hypothesis* $H_1$: In this case, the desired signal is present and embedded in noise. The probability of detection ($P_d$) is determined by counting the values which are greater than γ for certain number of trials.

$$H_1: s_l = u_1 + n_l \qquad l = 0,1,2,\dots,L-1 \tag{4-2}$$

where $u_1$ is a known signal sample.

Hypothesis testing was initially defined by Bayes [49] and improved from Neyman-Pearson [50]. Considering Neyman-Pearson based signal detection, for a fixed false alarm probability the optimal detection is formulated by using likelihood ratio test

$$T = \Lambda(s) = \frac{p(s;H_1)}{p(s;H_0)} > \gamma \tag{4-3}$$

where $\Lambda(s)$ is the likelihood ratio, $p(s;H_i)$ is the PDF under $H_i$. If PDFs of hypothesis depends on some unknown parameters then, the optimal Neyman-Pearson detection can be extended to [51]

$$T = \Lambda(s) = \frac{\int p(\boldsymbol{s}|\theta_1;H_1)p(\theta_1)d\theta_1}{\int p(\boldsymbol{s}|\theta_0;H_0)p(\theta_0)d\theta_0} > \gamma \quad (4\text{-}4)$$

where $\theta_i$ is the unknown parameter vector.

In the framework of Neyman-Pearson method, for a fixed false alarm rate, in order to set the detection probability for any test, the PDF of the decision variable information under $H_0$ is required. In general, the noise PDF is known but the noise variance is unknown. For this purpose, usually constant false alarm rate (CFAR) detectors are used [51]. All detection methods explained below are based on hypothesis tests.

## 4.1 Single coherent detector

Single coherent detection is performed after the correlation operation for single CIT of samples to enhance the sensitivity of the receiver. The correlation samples are integrated $M$ times. The output of coherent detection $P$ will be

$$P = \sum_{m=1}^{M} r_m^I + r_m^Q \quad (4\text{-}5)$$

where M is the number of samples equals to the product of $T_{coh}$, the sampling frequency $f_s$ and $r_m^I, r_m^Q$ are the inphase and quadrature components of complex correlation output samples. The amplitude of the accumulation process, $T_{stc}$ is

$$T_{stc} = |P| \quad (4\text{-}6)$$

The detection period is limited due to navigation data bit transition; therefore the SNR gain is restricted with respect to non-coherent squaring. In addition, oscillator stability, line of sight dynamics and channel effects are the other issues that limit the CIT.

## 4.2 Non-coherent squaring

Non-coherent squaring is a common method to detect GNSS signals. It is not influenced by navigation bit sign change during integration due to squaring operation. However this triggers SNR loss induced by squaring inphase and quadrature components of the complex baseband signal. The test statistic with $H_0$ is computed as follows:

$$T_{st}|H_0 = \sum_{k=1}^{p}(N_k^I)^2 + (N_k^Q)^2 \quad (4\text{-}7)$$

where $N^I, N^Q$ are the Gaussian distributed inphase and quadrature components of correlator output (only noise) respectively and $p$ is the number of non-coherent integrations. In hypothesis $H_1$, magnitude of correlation outputs are squared for number of non-CITs.

$$\mathrm{T_{st}|H_1} = \sum_{\mathrm{k=1}}^{\mathrm{p}}(\mathrm{P_k^I})^2 + (\mathrm{P_k^Q})^2 \quad (4\text{-}8)$$

where $P^I, P^Q$ are the inphase and quadrature components of the sum of desired signal and noise. Squaring loss is the main problem for weak signals. By squaring correlation outputs, noise components are squared as well and cannot be cancelled during accumulation. With small number of p, the standard non-coherent integration method provides gain and it is computationally efficient. However, if the number is large, gain and loss almost become stabilized and hereby provide minimum gain. In weak signal detection, performance with non-coherent integration is rather stringent. This effect can be reduced using other integration methods.

## 4.3 Differential detector

One method to partially mitigate squaring loss problem is to use differential detectors (DD). In this method, statistically independent signal samples are multiplied, in other words the current sample after coherent integration is multiplied with the complex conjugate of the previous sample in complex domain and then products are accumulated $p$ times. Operations are illustrated in Figure 4-1.

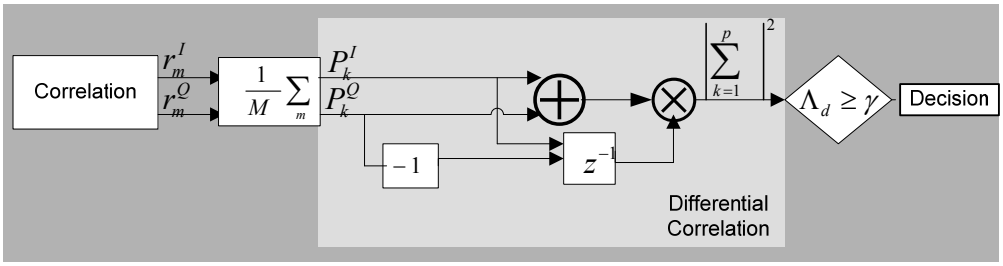


Figure 4-1: Block diagram of a differential detector

The test statistic is

$$T_d = \sum_{k=1}^{p} P_k P_{k-1}^{*} \tag{4-9}$$

Since the result is still complex, envelope square of the accumulation result is applied.

$$\Lambda_d = |T_d|^2 \tag{4-10}$$

The multiplication of adjacent noise samples are statistically independent when only noise exists, which is defined as:

$$\Lambda_{d|H_0} = \left|\sum_{k=1}^{p} N_k N_{k-1}^{*}\right|^2 \tag{4-11}$$

Hence, inner products of adjacent noise samples have zero mean.

$$E\left(\Lambda_{d|H_0}\right) = 0 \tag{4-12}$$

The correlation output is squared by using non-coherent squaring method and noise components are squared as well. Hence, we can say that noise power of differential correlation method is less than non-coherent squaring.

## 4.4 Other detectors

Different detectors are studied in the literature to optimize the computational complexity and reduce the performance loss due to squaring signal components as well as squaring noise terms. Commonly used ones are summarized in the following:

- *Dot product method*: Integrates the product of adjacent two samples sampled at different time instants [52]. The approach provides gain in terms of squaring loss, however performance gain is severely affected in the presence of Doppler frequency shifts. This method can be implemented with the same computational complexity as standard non-coherent squaring method.

  $$T_{dp} = \sum_{k=1}^{p} P_k^I P_{k-1}^I + P_k^Q P_{k-1}^Q \tag{4-13}$$

- *Differential real detection method*: Integrates the product of consecutive terms skipping one product among two other products [8]. This approach avoids the excessive computational requirement of the standard and dot product method. However, the performance gain is diminished in the presence of Doppler effect.

$$T_{difr} = \sum_{k=1}^{p/2} P_{2k}^{I} P_{2k-1}^{I} + P_{2k}^{Q} P_{2k-1}^{Q} \tag{4-14}$$

- *Post detection correlation combining technique*: An enhanced detection technique, proposed by [53] yields sensitivity gain over aforementioned differential detection techniques. The architecture is a generalized estimator-correlator described in [51].

## 4.5 Performance comparison of detectors

The performance of DD and NCS is compared for the GPS L1 C/A signal using different scenarios illustrated in Table 4.1. Two cases are considered for code delay $\Delta\tau$, Doppler frequency $\Delta f_D$ and carrier phase $\phi$ parameters which are either zero or uniformly distributed random variates. An exemplary dwell time of 10 s is chosen due to indoor environment requirements. For uniformly distributed random variates, corresponding parameters are generated in the range of

$$\Delta f_D \in \left[-\frac{1}{2T_{coh}}, +\frac{1}{2T_{coh}}\right] \tag{4-15}$$

$$\Delta\tau \in [-1/8, +1/8] \tag{4-16}$$

$$\phi \in [0, 2\pi] \tag{4-17}$$

Table 4.1: Simulation scenarios

| Scenario | Prob. of false alarm | Zero valued parameters | Uniformly distr. parameters |
|---|---|---|---|
| I | $10^{-3}$ | $T_{coh}$=500 ms, m=20 | |
| II | $10^{-3}$ | $T_{coh}$=5 s, m=2 | |

For an identical dwell time, various $T_{coh}$ and m values are Monte-Carlo simulated for zero valued acquisition parameters. It is noteworthy that no other effects have been considered in this simulation such as user-satellite line-of-sight dynamics, oscillator jitter or multipath channel effects. Those effects are touched upon in section 5.3.1. In this sense, presented simulation results are somehow overly simplistic but clearly demonstrate a possibility to achieve high sensitivity gain using long CITs. The obtained sensitivity loss for the first case compared to the second case is about 3.3 dB with NCS and 2.5 dB with DD as illustrated in Figure 4-2. Hence, DD suffers less squaring loss (0.8 dB) than NCS. Furthermore, for a low number of non-coherent integrations m=2, DD and NCD practically give identical performance.

Within a more realistic scenario, using same dwell time for different $T_{coh}$ and $m$ with uniformly distributed acquisition parameters is investigated. Again the squaring loss effect is more evident when using shorter $T_{coh}$ in the integration process as shown in Figure 4-3. Uniformly distributed delay, Doppler and phase variates (compared to zero values) affect DD and NCS detection identically.

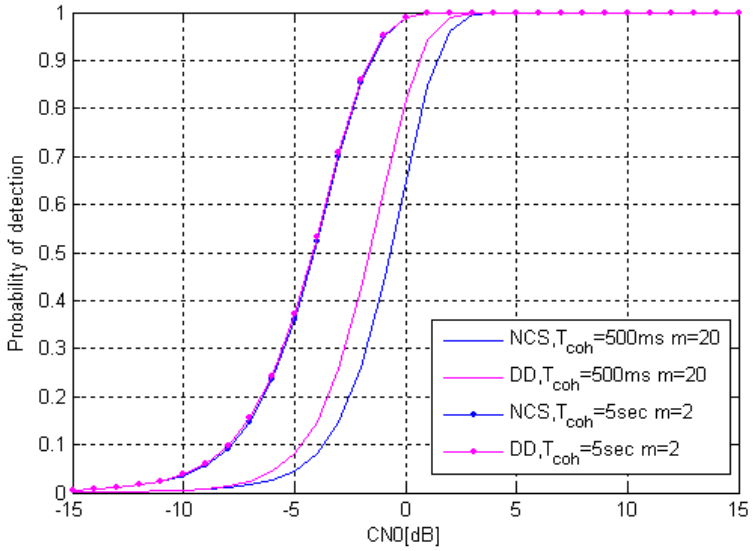


Figure 4-2: Probability of detection versus $C/N_0$ with zero valued code delay, Doppler frequency, carrier phase

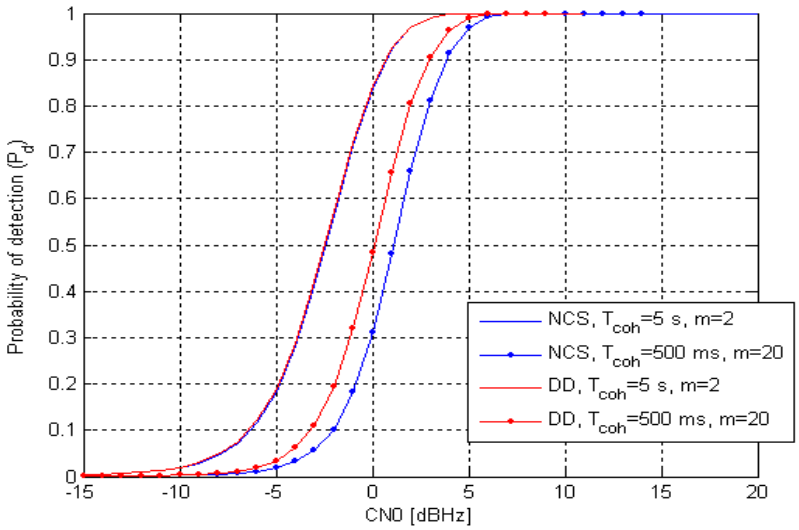


Figure 4-3: Probability of detection versus $C/N_0$ with uniformly distributed code delay, Doppler frequency and carrier phase

## 4.6 Conclusion

In this chapter, possible signal detectors in GNSS receivers are summarized and the most commonly used differential detector and non-coherent squaring detectors are compared. Non-coherent detection involves squaring of the coherent integration output to improve the detection sensitivity. Due to squaring, it is robust against data bit transition and frequency errors. On the other hand, it is also delicate to uncertainty in the noise variance and this may limit the sensitivity gain in detecting weak signals. The sensitivity gain is improved via differential correlation due to multiplication of statistically independent signal samples despite squaring identical samples. This gives gain of around 1 dB with respect to non-coherent squaring method for a dwell time of 10 s.

# CHAPTER 5. HIGH SENSITIVITY AND ASSISTED GNSS ACQUISITION

Navigation systems play a significant role in today's location based services. As the number of GNSS users increase, the indoor localization domain is getting more attention. Requirement of indoor location was initially declared in the context of Enhanced-911 system [54]. A large number of further applications require indoor localization capabilities: M-commerce, firefighting, military, surveying of vehicles in underground car parks and surveying of children and elderly people. In Europe, there are considerations to establish the E-112 emergency call in a similar way [55]. In the early 1980's, investigations have been carried out which rely on external Doppler and ephemeris assistance. The transmission of measured pseudo-ranges from a mobile unit to a processing center was already patented by Navysis. Indoor localization on the basis of a high sensitivity GPS receiver was demonstrated by the USCG Academy [56] and Snap Track [57] using FFT. Indoor-capable GPS chipsets are mass market products since 2001: Global Locate AGPS chip with 16,000 correlators, SnapTrack, GPSOneTM AGPS Chip, SiRFStar IITM and IIITM. The latter one is equipped with 200,000 parallel correlators and available since 2004.

There was a widespread opinion that it is impossible to receive GNSS signals in places like underground car parks. Particularly, low cost products are not capable to meet the indoor requirements due to using cheap solutions. Although the low GNSS outdoor signal level after penetrating a wall will be further reduced, the physics of propagating electromagnetic waves in the L-band states that a measurable GNSS signal level has to be still available even in an underground environment. However, using GNSS in an indoor environment is still a challenging task due to channel characteristics such as large attenuation and multipath fading. Under these channel conditions, it is difficult to estimate coarse code phase and Doppler frequency using standalone acquisition algorithms.

## 5.1 Indoor Channel Model

Although high sensitivity GNSS technology of the current state of the art can cover car navigation and dense urban canyon area, the core indoor area is still a big challenge due to its physical limits. Therefore, in the literature a considerable amount of work has been spent to analyze the

indoor channel, performing either field tests [32], [58], [20], [59], [60] or simulated channel models [61], [62]. In indoor conditions, the line of sight (LOS) signal is not very probable to be available or partially available and the signal reaches the receiver through concrete walls that causes significant degradation on the signal power. Usually less than signal level of 25 dBHz is received. Due to the effect of multipath propagation the signal experiences distortion and attenuation. Concerning the multipath effect, the signal correlation function shape is destroyed that is used to estimate acquisition parameter of code delay. Besides the correlation function, the Rx signal amplitude, phase, time of arrival (TOA) and angle of arrival (AOA) also varies. In indoor environment, the Doppler shift caused by the motion of the receiver is smaller with respect to the outdoor environment and this makes Doppler estimation more challenging. In addition, the cross-correlation problem should also be considered due to the possibility of signal reaching the receiver at different signal power levels; one through concrete wall, the other through a window. In this section, Lutz channel model [60] that well reflects satellite channel's features and real indoor environment has been used for the analysis of acquisition process.

## 5.2 Advanced Indoor Acquisition Methods

### 5.2.1 Zero-padded FFT method

In acquisition process, parallel search in the code delay domain method is implemented via FFT correlation. In assisted acquisition, zero padding method is used. Since C/A code is a 1 ms periodic code, linear correlation is performed by circular correlation. In case of C/A code assisted acquisition, the local code is multiplied with the navigation data bit before correlation, hereby the C/A local code can be considered as a non-periodic code. As a result, circular correlation is performed with zero padding for non-periodic codes; otherwise applying only circular correlation cannot provide correct results. As illustrated in Figure 5-1, the correlation is performed by taking FFT of both signals. First, *N* samples of the incoming signal is padded with user defined points of zeros. The same length of the product of local code and the navigation data is then transformed using FFT operation. The complex conjugate of FFT of the product of local code and navigation data is realized. With zero padding, the frequency spacing of FFT bins is reduced from $1/T_{coh}$ to $1/2T_{coh}$. In this way, bin spacing loss is reduced by using zero padded FFT. The algorithm is as follows:

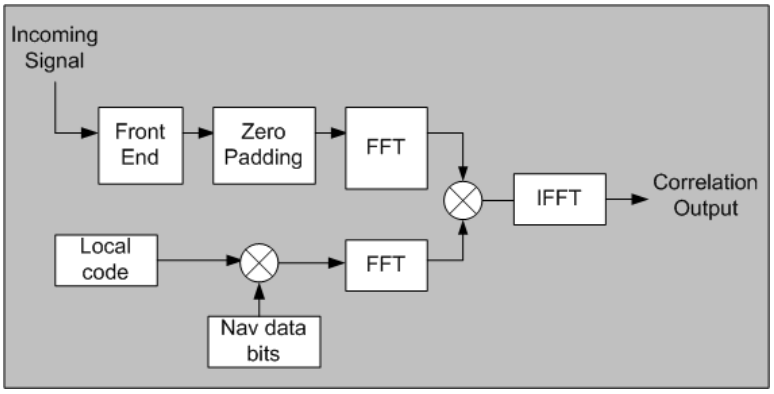


Figure 5-1: Block diagram of zero padded acquisition method

**Input:** $r_\mu$ *digitized IF signal*
**Output:** $\hat{f}_D$ and $\hat{\tau}$

*1: Take N samples of the Rx signal*
*2: Pad with zeroes for a user defined uncertainty time* $T_{unc}$ *for both side of the Rx signal*
*3: Take the FFT operation on overall samples*
*4: Multiply the local code with the navigation data bit retrieved from a reference network and take the FFT operation*
*5: Multiply the FFT of shifted resampled samples with complex conjugate of the FFT of the local code multiplied with the navigation data bit*
*6: Take the inverse FFT operation of the multiplication and save the corresponding index of the Doppler frequency and code phase where the maximum correlation peak is achieved*
*7: Repeat the circular rotation for the overall frequency uncertainty region and get the maximum of the maximum correlation peak amplitude*
*8: Estimate the Doppler frequency, code phase and* $C/N_0$ *based on the maximum likelihood criteria*

Algorithm 5-1: Zero padded FFT algorithm

### 5.2.2 Neyman-Pearson method

As stated in CHAPTER 4, the detection threshold $T_d$ is determined by using Neyman-Pearson criterion. The probability of detection $P_d$ is maximized by choosing the minimum detection threshold $T_d$ provided not exceeding the maximum probability of false detection.

**Input:** $r_\mu$ *digitized IF signal*
**Output:** $\hat{f}_D$ and $\hat{\tau}$
*1: Take N samples of the Rx signal*
*2: Pad with zeroes for a user defined uncertainty time* $\mathrm{T_{unc}}$ *for both side of the Rx signal*
*3: Take the FFT operation on the overall samples*
*4: Add square envelope of coherently integrated samples for a number of non-coherent integrations*

Algorithm 5-2: Neyman - Pearson algorithm

### 5.2.3 Parallel Intra-Frequency Interference Cancellation

In real life scenarios, the signal propagates over different paths from satellites to GNSS receiver such that it arrives with different time delays and phase rotations. At the receiver, only the superposition of all weak and strong signals is observed. In order to detect strong signal components, the receiver uses conventional one coherent acquisition algorithm with a detection threshold value of 35 dBHz. Furthermore, in weak signal detection, the receiver is making use of coherent and non-coherent integrations with a detection threshold value of 25 dBHz or less. However, one main problem with weak signal detection is due to cross correlation between weak signal and strong interfering signal components which lead to false acquisition or incorrect correlation peak location. When Rx signal power of one or more satellites is stronger than the desired signal to be detected, then non-zero cross-correlation peaks mask the desired signal. This phenomenon is known as multiple access interference (MAI).

One of the approaches to combat with strong interfering signals is to use parallel interference cancellation (PIC) method. In this method, a two level parallel interference cancellation based acquisition (PICA) is modeled. The main idea of PICA is based on the estimation of all strong interfering signals and then subtracting these interfering signals from the Rx signal. In the first level of PICA, the receiver performs conventional one coherent acquisition algorithm to acquire all strong satellite signals. Afterwards, strong signal components of Doppler frequency, code delay, signal amplitude and data bit are regenerated as I/Q complex baseband components and subtracted from the down converted Rx signal in the baseband domain. Then the system runs for the second level of PICA in order to acquire weak signal components. In this level, the system uses coherent and non-coherent integrations. In non-coherent integration, detection algorithms of

either Neyman-Pearson or differential complex correlation can be used. In indoor environments, the number of strong signals is not supposed to be high, i.e. a few strong signals at most. The model contains only two signals, one strong and one weak signal for the sake of simplicity. The complexity of PICA is directly proportional with the number of acquired strong satellite signals. This can be noticeably reduced by simplifying the configuration of the proposed detector. In this case, after the first level acquisition, when number of acquired strong signals exceed a predefined value (i.e. three strong satellite signals), then only the first three strongest signals are regenerated and then subtracted from the down converted Rx signal. The explanation for this simplification is that the first three strongest signals have the most significant cross correlation interference effect among all strong signals. Rest of the acquired strong signals are excluded and not considered for the signal regeneration process. As a result, cross correlation gives an effect of large pseudo-range errors since peaks take place at random delays.

***Input:*** *Superposition of interference plus desired IF signal*
***Output:*** *Weak signal*

*Step 1:*
*1: Detect the strongest signals* $\widehat{s_1}$, $\widehat{s_2}$ *and* $\widehat{s_3}$ *in acquisition and tracking processes.*
*2: Regenarate only max. 3 strongest signals since they have the most cross correlation effect.*
*3: Regenerate an estimate of the strongest signals, using knowledge of time, phase and amplitude which are derived from the tracking output. Ignore the rest of the strong signals to be regenerated.*
*4: Subtract regenerated signals* $\widehat{s_1} + \widehat{s_2} + \widehat{s_3}$ *from the total Rx signal* $\mathrm{r(t)}$.

*Step 2:*
*1: Acquire weak signals by using coherent and non-coherent integrations*
*2: if (*$C/N_0$ *(*$\widehat{s_1} + \widehat{s_2} + \widehat{s_3}$*)<24 dB) break*
*3: else continue*
*4: end if*

Algorithm 5-3: PICA algorithm

The Rx signal can be written as:

$$r(t) = \sum_{k=1}^{K} \sqrt{2P_k}\, d_k(t-\tau_k) c_k(t-\tau_k)\, cos(w_k(t-\tau_k) + \phi_k) + n(t) \quad (5\text{-}1)$$

where $d_k(t)$ is the $k$-th satellite's information bearing signal, $c_k(t)$ is the corresponding spreading code information, $w_k$ is the frequency of the signal with Doppler frequency offset, $\phi_k$ is the phase of the $k$-th signal, $P_k$ is the average Rx signal power of the $k$-th signal and $\tau_k$ is the

time delay of the *k*-th signal. For simplicity, assuming the scenario with perfect code phase and carrier frequency recovery, the Rx signal for the *k*-th satellite is given by:

$$r(t) = \sqrt{2P_k}d_k(t-\tau_k)c_k(t-\tau_k) + \sum_{\substack{j=1 \\ j\neq k}}^{K} \sqrt{2P_j}d_j(t-\tau_j)c_j(t-\tau_j)\cos(w_j(t-\tau_j)+\phi_j) + n(t) \quad (5\text{-}2)$$

The first term is the desired signal, the second term is the MAI and the last term is the AWGN component. In order to cancel the effect of MAI from the Rx signal, PICA is used. In Figure 5-2, the receiver structure for PICA is shown where signal parameters of frequency, code phase and the signal amplitude are estimated through the tracking module and by using these parameters the signals are regenerated and subtracted from the Rx signal. The rest of the signal containing weak signals is detected by the indoor acquisition block.

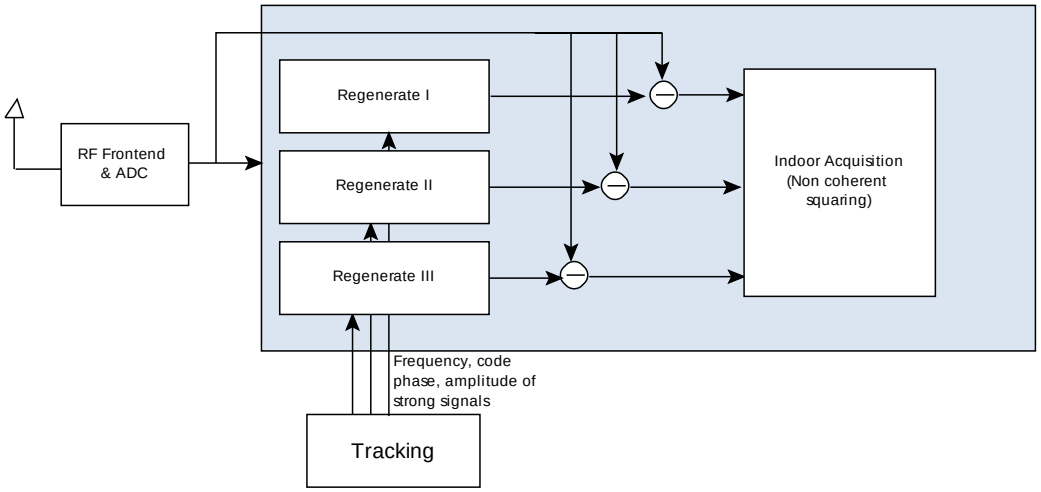


Figure 5-2: PICA structure

## 5.3 Assisted Acquisition

Standalone GNSS may not work appropriately when received signal does not involve the LOS signal component. Using cellular based positioning solutions such as cell ID or the Angle of Arrival (AOA) techniques, a position solution is achieved with accuracy far less than satellite based positioning. The cellular based positioning depends on the size of the transmitting BS and

Node-Bs. In rural areas, the number of BS is poor, accordingly the position estimation error is in the order of 30 km [34]. In urban areas, cellular networks have a deficiency in synchronization which degrades the positioning performance. Due to these shortcomings, assisted GNSS is used. Assisted GNSS is a hybrid positioning technique, where the cellular network provides satellite constellation information directly to the GNSS system.

Another reason to use assisted acquisition is to improve the sensitivity of the receiver. In the consideration of the requirement to acquire heavily attenuated signals in GNSS receivers, it is inevitable to integrate signals within 1 s or more integration time. The sensitivity increase depends mainly on $T_{coh}$. In general, reference networks provide direct additional information to receivers about Doppler frequency $f_d$, code phase $\tau$ and navigation data bit sign and location. By providing assistance to receivers, the search space is reduced and in this way the computational complexity is reduced to a limited frequency and time range. In *indirect assistance*, Doppler frequency and code phase is derived from the receiver itself. In this case the navigation data bit information is retrieved from the network to allow unlimited integration time in the correlation process. For a *full assisted* case, the receiver gets the following assistance from a reference network:

- Navigation data symbols
- List of visible satellites (already tracked or acquired satellites)
- Expected Doppler and code phase
- Nominal satellite time for the corresponding navigation data bits in GPS week/sec

The navigation data bit is retrieved with a timing uncertainty. By retrieving the navigation data bit as an assistance data, the integration time can be extended. In this thesis, weak signals are detected using indirect assistance information of navigation data by coherently integrating for unlimited number of times. Acquisition module receives the assistance data via a TCP/IP connection from a dedicated reference receiver as represented in Figure 5-3. A further purpose to use assisted acquisition is to reduce the time to first fix (TTFF). Many commercial GNSS products are available in the market to provide assistance data. In the following different commercial solutions are described and performance comparison is illustrated in Table 5.1.

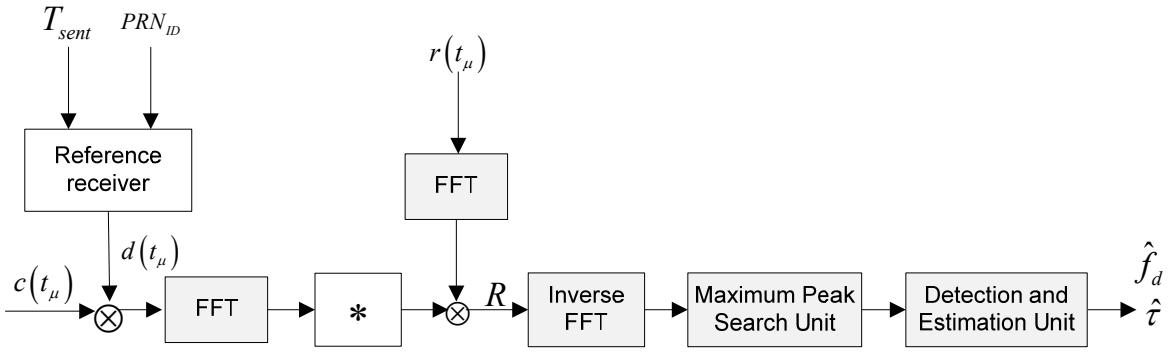


Figure 5-3: Assisted acquisition flow diagram with an assistance of navigation data bits retrieved from a reference receiver

Table 5.1: Commercial solutions

| Commercial Solutions | Chipsets | Number of corr. | Cold start sensitiv. [dBm] | Warm start sensitiv. [dBm] | Tracking sensitiv. [dBm] | Cold start TTFF [s] | Warm start TTFF [s] |
|---|---|---|---|---|---|---|---|
| SnapTrack | gpsOne | 10000 | -155 | -160 | -160 | - | - |
| GlobalLocate | Hammerhead | 20000 | -130 | -160 | -160 | 1[1] | <1[1] |
| eRide | Opus III | 44000 | -155 | -161 | -161 | 35 | 34 |
| SiRF | Star III | 200000 | -140 | -150 | -159 | 42 | 38 |
| µBlox | µBlox | 1000000 | -145 | -160 | -160 | 1 | <1 |
| Nemerix | NemeriX | 64 | -139 | -147 | -152 | 50 | 38 |

[1] *TTFF* is measured in mobile based platform

### 5.3.1 Impacts of Error Sources on Assisted Acquisition Performance

Assisted acquisition is studied under variety of scenarios including fading channel, receiver oscillator jitter and user dynamics. Signal sensitivity levels become higher when CIT is large since CIT specifies the main sensitivity gain. However, long CIT leads to problems in acquisition

depending on line of sight acceleration, receiver clock jitter and multipath fading effects. While line of sight acceleration principally causes drift on Doppler frequency which results correlation loss in the coherent accumulation, receiver clock jitter mainly leads to non-linear carrier phase variations.

#### 5.3.1.1 User dynamics

Relative velocity between moving satellite and mobile user results in Doppler shift due to random frequency modulation on the signal. Besides, relative acceleration causes a change in the Doppler shift in time and called Doppler rate which makes Doppler frequency estimation rather difficult at the receiver and causes Doppler frequency estimation errors and signal power loss. In practice, line of sight dynamics caused by the user or satellite movement limits the CIT to one second or less [41]. This would be one of the main problems for L2C pilot signals which have code length of 1.5 s. The line of sight distance at time *t* is given by

$$x(t) = x_0 + v_0 t + \frac{1}{2} a t^2 \tag{5-3}$$

where $x_0$ is the initial relative distance, $v_0$ is the initial relative velocity and $a$ is the line of sight acceleration. The acceleration causes drift on Doppler frequency and code phase which could be estimated by

$$\hat{f}_D = f_{D0} \pm f_{RF} \frac{at}{c} \tag{5-4}$$

$$\hat{\tau} = \tau_0 \pm \frac{x}{l_c} \tag{5-5}$$

where $c$ is the speed of light, $l_c$ is the code length in meters, $f_{D0}$ is the initial Doppler frequency and $\tau_0$ is the code phase. In Figure 5-4, different acceleration effects on cross correlation amplitude is studied by considering Rx signal power of -157 dBW. As can be seen, even at high signal power, with acceleration of 7 $\mathrm{m/s^2}$, there is a high correlation loss and the signal detection is not successful.

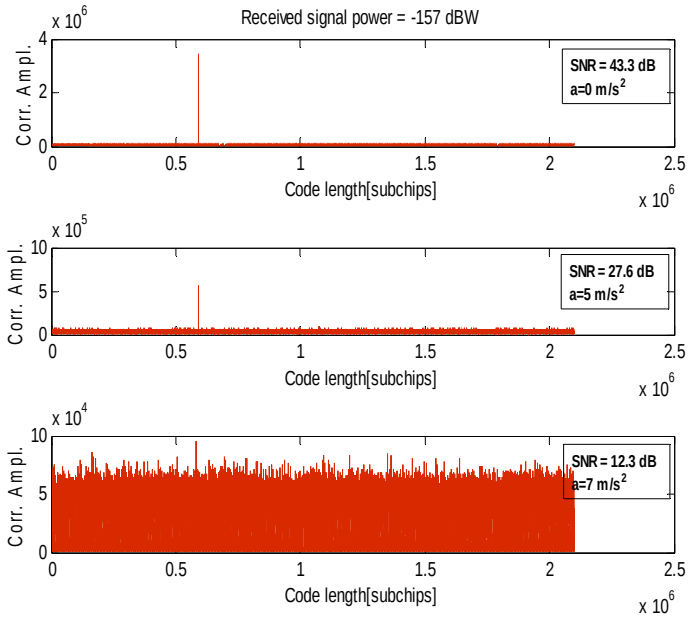


Figure 5-4: Correlation amplitude versus code length for different accelerations of 0, 5 and $7\mathrm{m/s^2}$ respectively

This correlation loss due to acceleration could be compensated in the receiver simply by frequency modulation either on the locally generated code or on the Rx signal. If the compensation is applied to the local, then the modified local code $c_{PRN}^{com}$ generation yields:

$$c_{PRN}^{com}(t) = c_{PRN}\left(t - \frac{x(t)}{c}\right) exp\left(\frac{\pi i a t^2}{c} f_{RF}\right) \tag{5-6}$$

The sign of the exponential function changes depending on the relative direction between satellite and mobile receiver. Figure 5-5 shows the compensated correlation outputs as a function of different accelerations applied to the local code considering acceleration of $7\ \mathrm{m/s^2}$ with code phase offset of half code length and without code phase offset. As can be seen, Doppler compensation method is not effective when the Rx signal has code phase offset. This is due to the relation between carrier phase change caused by acceleration and circular correlation used in the FFT based acquisition method. Strictly speaking, the circular correlation is negatively affected by carrier phase change and this effect should also be compensated by the following algorithm:

- Take local code with 2xFFT length (two code periods)
- Take Rx signal with 2xFFT length (last FFT length is zero padded)

- Rotate the local code rather than Rx signal and perform multiplication

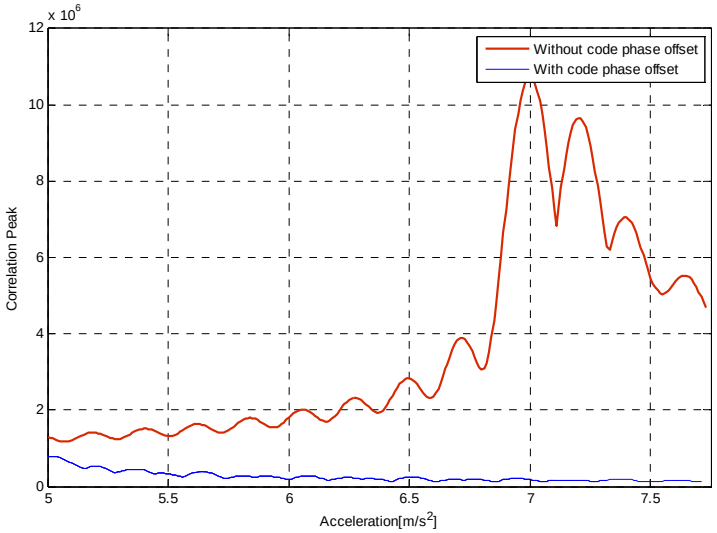


Figure 5-5: Line of sight acceleration compensated maximum correlation peaks versus acceleration values for Rx signal with $7\mathrm{m/s^2}$

The critical point is that in 1.5 s when the distance taken by line of sight accelerations is much greater than 6.1 cm that is one quarter of the wavelength of L2CL code, then the receiver could not be able to capture the non-linear carrier phase variations and therefore signal detection may not be succeeded. It should be pointed out that line-of-sight accelerations are always present due to the satellite motion. As a rule of thumb, those variations are below $0.2\ \mathrm{m/s^2}$. In Figure 5-6, carrier phase variations for an acceleration of $0.5\ \mathrm{m/s^2}$ are illustrated. In Figure 5-7, different line of sight acceleration effects on signal detection is observed. With line of sight acceleration of $0.01\ \mathrm{m/s^2}$ (5.4 km/h in 150 s) and $0.05\ \mathrm{m/s^2}$ (27 km/h in 150 s), for detection probability of 90%, estimated signal power levels are -185.8 dBW and -184.8 dBW respectively. Distances taken by all accelerations are 1.1 cm, 5.5 cm respectively in time range of 1.5 s. Results indicate that Doppler frequency is negatively influenced by the increase of the line of sight acceleration. On the other hand, the line of sight acceleration effect on code phase is rather small. The sensitivity loss with line of sight accelerations of $0.01\ \mathrm{m/s^2}$ and $0.05\ \mathrm{m/s^2}$ is about 1 dB and 2.4 dB respectively in case when there is no acceleration. The distance taken in 1.5 s with these accelerations are below the quarter wavelength of L2CL code; therefore non-linear carrier phase variations are below this limit and cause no challenge in terms of signal detection.

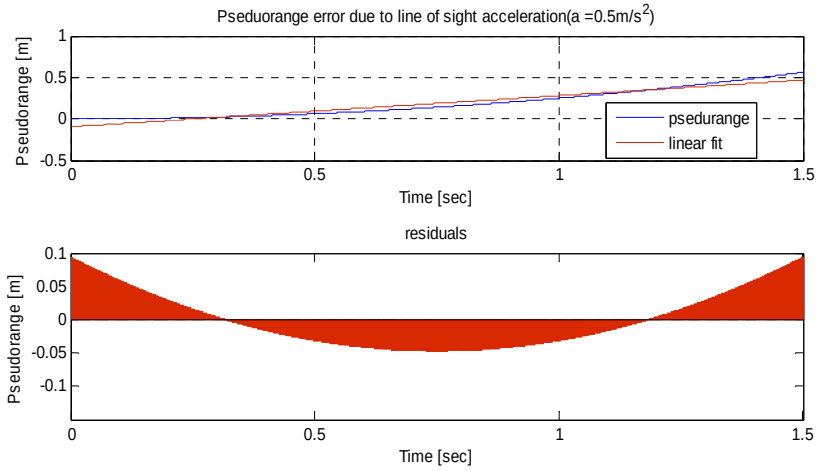


Figure 5-6: Pseudo-range error and carrier phase variations line of sight acceleration of 0.5 $m/s^2$

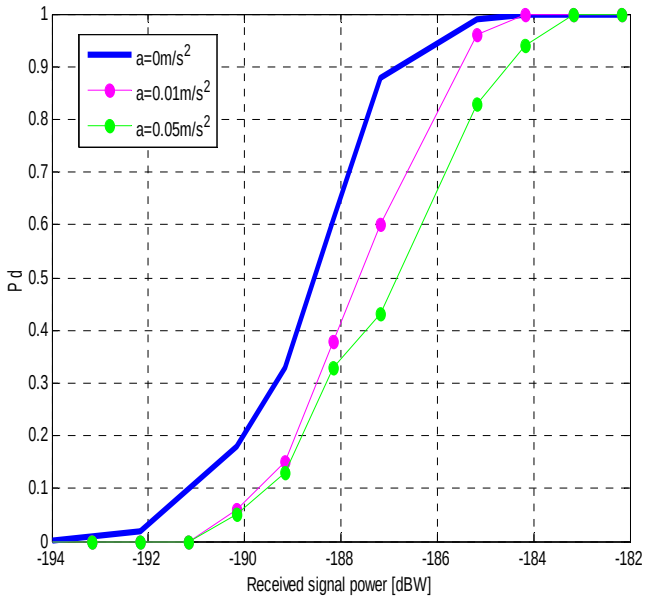


Figure 5-7: Probability of detection versus estimated Rx signal power for different line of sight accelerations

#### 5.3.1.2 Clock jitter

The clock used to down convert the signal from RF to IF domain has a significant effect on GPS receiver sensitivity. The clock stability during cross correlation is critical where clock stability results in correlation loss low. Additionally, at weak signal conditions, the loss is getting more severe. A high stability clock such as OCXO yields less drift on code phase and Doppler frequency. However, due to cost purposes, in a mass-market indoor GNSS receiver low-cost, low-power clocks are used such as standard Quartz. In practice, this effect can be compensated in the positioning process by measuring the pseudo range to four satellites rather than three satellites in view. In our simulations, the clock compensation is not considered since the purpose is to observe the clock stability effect on long coherent integration. The clock models implemented in GNSS IF Software Signal Simulator (SigSimSoft) is modeled in the form of stochastic differential equations based on [63]. For different clock modeling Allan variance parameters are used. The pseudo-range error caused by the receiver clock is plotted in Figure 5-8 as a function of time with five different instantiations of 1.5 s for a comparison of different oscillator types.

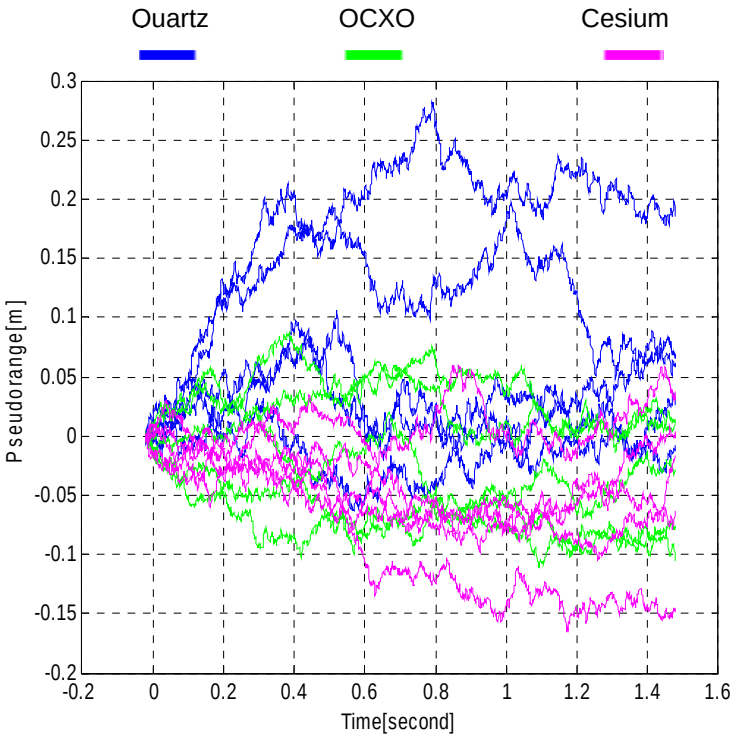


Figure 5-8: Pseudo-range error for different oscillator types

As illustrated, the OCXO clock is the most stable one. Cesium and Quartz clocks show the medium and the worst stability over 1.5 s. Although the OCXO clock shows the best performance for short period, Cesium clock is good at long-term frequency stability.

In Figure 5-9, the pseudo-range change due to Quartz clock error for one L2CL code period is illustrated. The difference between pseudo-range and linear fit provides the non-linear carrier phase variations which can be seen from the lower plot of Figure 5-9. The carrier phase variation should be less than one quarter of the wavelength to acquire the signal within one CIT of 1.5 s. The power level in Figure 5-10 relates to the full L2 civil signal. However, only the L2CL signal is acquired. In the ideal case scenario, for detection probability of 90%, the receiver sensitivity is -187 dBW. With OCXO clock, the sensitivity is -184 dBW which is better than Cesium clock by 0.25 dB and Quartz clock is worse than Cesium clock by 0.8 dB. From Figure 5-10, we can conclude that even with low cost Quartz signal acquisition with an integration time of 1.5 s is feasible, however sensitivity loss of 3 dB is observed compared to the ideal case.

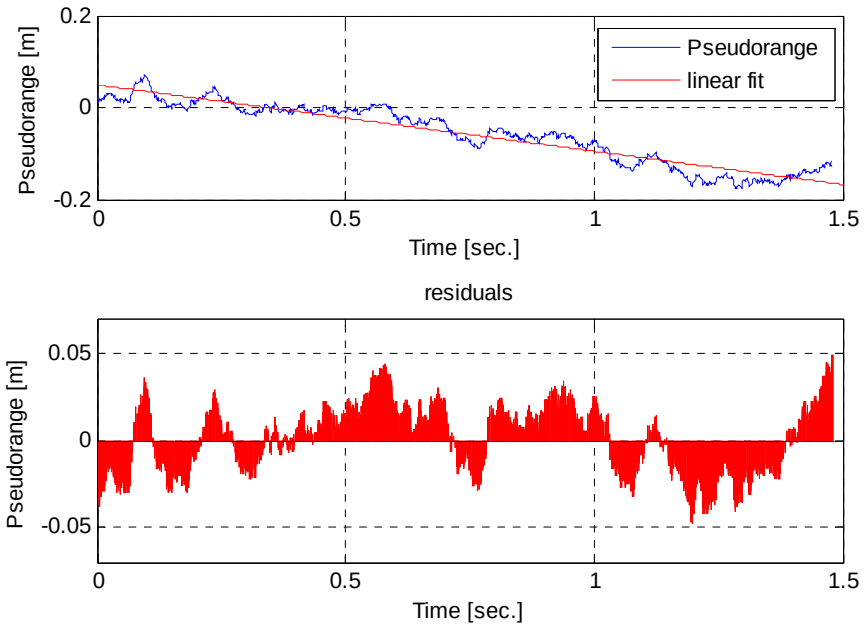


Figure 5-9: Pseudo-range error and carrier phase variations of standard Quartz clock

Results showed that with any oscillator type, signal detection is mainly effected from non-linear carrier phase variations. It has small influence on Doppler frequency and code phase change. With OCXO clock, the receiver sensitivity is 3 dB less than the receiver sensitivity with ideal clock and it gives the best sensitivity among Cesium and Quartz clocks since it is the most stable one in short time period of 1.5 s. The average sensitivity loss with Cesium and Quartz clocks are 3.3 dB and 4 dB respectively for detection probability of 90%.

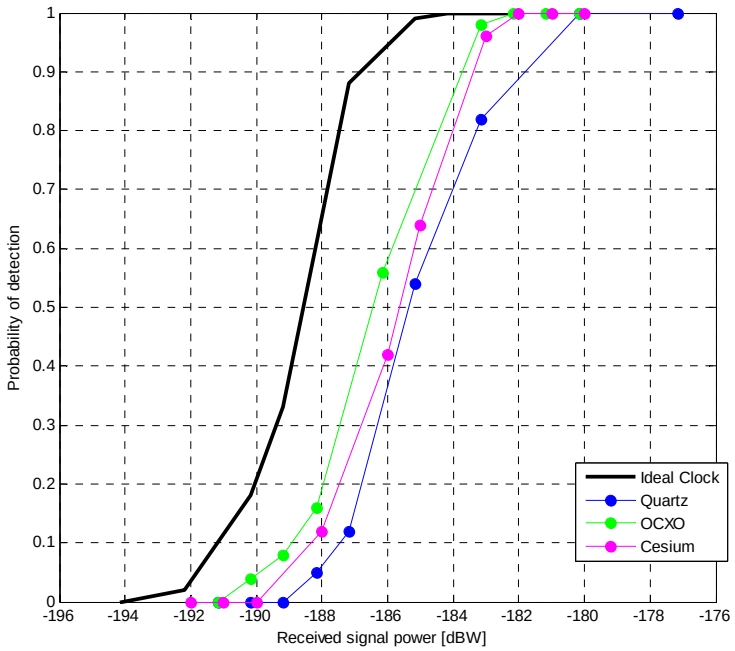


Figure 5-10: Probability of detection versus $C/N_0$ for different oscillator types

### 5.3.1.3 Channel conditions

As it is well known, the signal propagates over different paths from satellites to the GNSS receiver such that it arrives at the receiver with different time delays. At the receiver, only superposition of these signals can be observed. According to the phase shift of signals at the receiver, alternating minima and maxima of the signal amplitude is obtained. This type of channel models can be realized by considering narrowband radio channels. To investigate receiver sensitivity level in different channel conditions, narrowband empirical Lutz channel model [60] is used provided by SigSimSoft. The fading behavior of the channel is composed of two states; the

first state is the good state or unshadowed where the channel has LOS component which depicts Ricean fading distribution. The second state is the bad state, blocked or shadowed where the channel is characterized by NLOS components which give Rayleigh fading distribution. Lutz channel model statistically combines Ricean and Rayleigh fading distributions. Figure 5-11 is driven by signal shadowing and the switching between good and bad state is controlled by a continuous time Markov process.

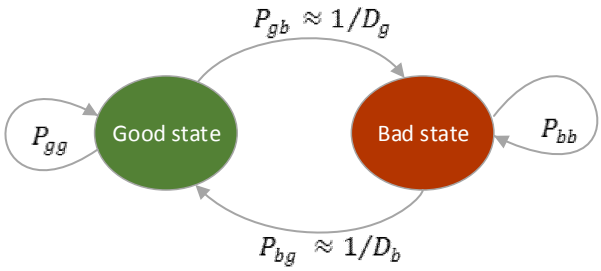


Figure 5-11: Two-state Markov process

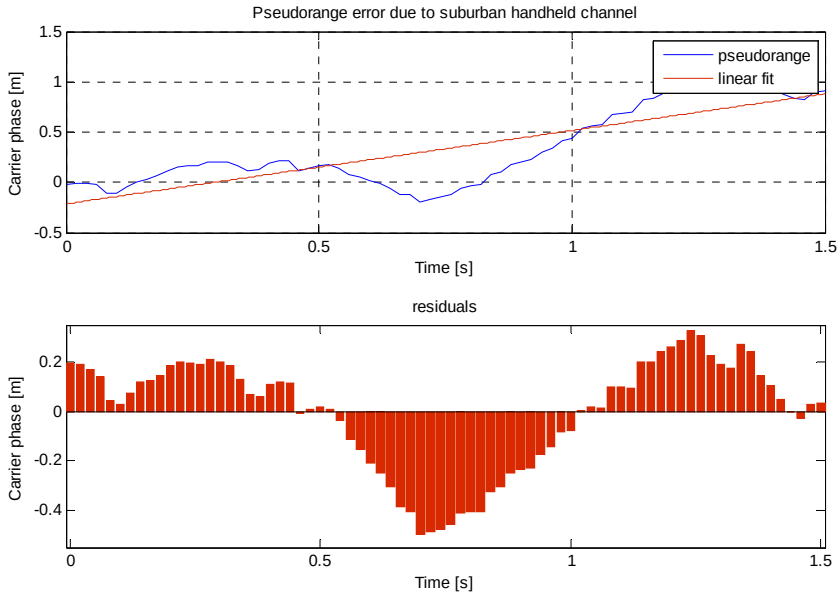


Figure 5-12: Pseudo-range error vs. time for suburban handheld channel for a user with 7 *km/h* velocity

$D_g$ and $D_b$ are mean durations in which the channel remains in the good and the bad state. $P_{gb}$, $P_{gg}$, $P_{bb}$ and $P_{bg}$ are the state transition probabilities expressing the probability of change from state good to bad or vice versa and also presenting probability of being in good and bad states. The major acquisition sensitivity loss is caused by the channel effects with multipath fading and shadowing. Figure 5-12 presents the pseudo-range error caused by Rayleigh fading effect as a function of GPS time. It can be seen that in 1.5 s, carrier phase variations cause pseudo-range error of about 40 m.

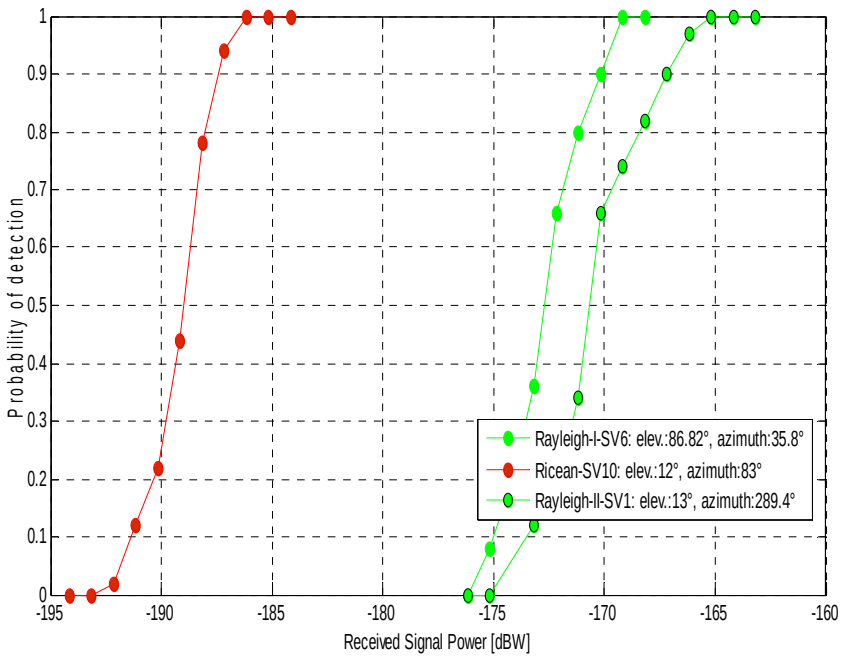


Figure 5-13: Probability of detection versus $C/N_0$ for different channel conditions

The impact of multipath on acquisition is very low and could be ignored in case the receiver is static since only amplitude has some small changes but the phase is constant, on the contrary multipath contributes significant effect when the receiver is moving. To observe the channel effect for a moving receiver, we assumed the receiver has a velocity of 7 *km/h*. In Figure 5-13, the acquisition sensitivity performance in a suburban handheld channel as a function of elevation angle is observed. The Rayleigh fading channel causes 15 dB sensitivity loss in comparison to the Ricean fading channel. Bad state-a and b curves differ in satellite elevation and azimuth values. The satelite in good state has an elevation angle of 12° and an azimuth of 83°. The satellite

position parameters for bad state a and b are elevation angle of 86°, 13° and azimuth angle of 358°, 289° respectively.

The corresponding carrier phase variations and fading envelopes are illustrated in time range of 1.5 s in Figure 5-14 and Figure 5-15. Deep fadings occur in Ricean fading channel which is about -25 dB and almost no phase variations are observed. In Rayleigh fading channel, deep fadings occur to around -40 dB level which can be observed from the upper plot of Figure 5-15 and carrier phase variations in that time range is illustrated in the lower diagram. Results show that Rayleigh fading channel causes 15 dB acquisition sensitivity loss and this is the major sensitivity loss among all error sources studied in this section. This indicates the significance of absence of line of sight signal on the acquisition performance.

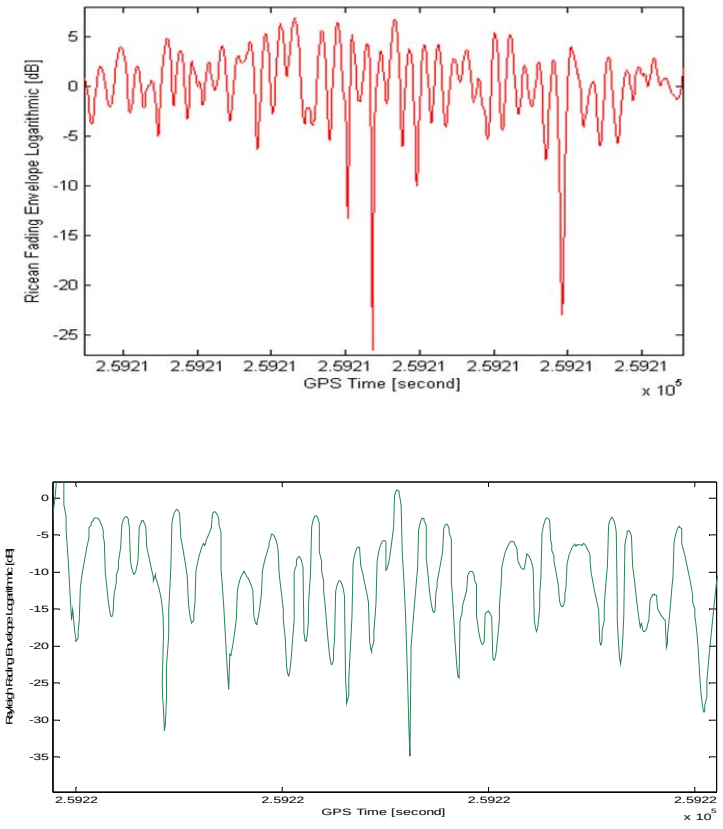


Figure 5-14: Ricean (upper) and Rayleigh fading envelope logarithmic versus GPS time

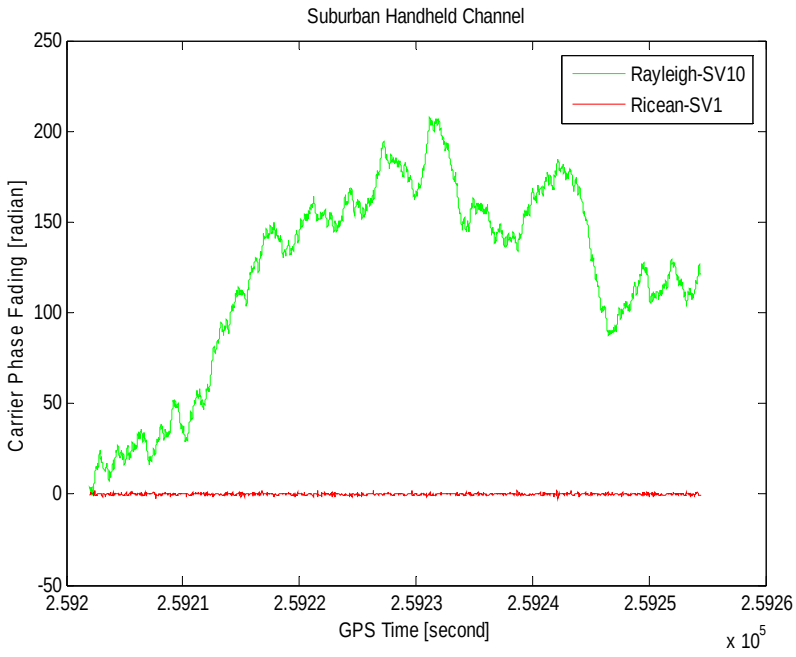


Figure 5-15: Rayleigh fading envelope logarithmic versus GPS Time (upper); Carrier phase fading versus GPS Time for bad state

### 5.3.2 Assisted acquisition field-test results

In general, in indoor environments the line of sight (LOS) signal is not available and cross-correlation of signals with different Rx signal power occurs. Cross-correlation of satellite signals penetrating through windows, namely strong signals and signals penetrating through concrete walls, namely weak signals cause the cross-correlation problem. In this case, it is difficult to acquire weak signals since the cross-correlation peak of strong and weak signals might be greater or at the same level of the autocorrelation peak of weak signals. The cross-correlation peak amplitude is related to the relative $C/N_0$ ratios between strong and weak signals. Assisted acquisition field tests are performed in an indoor environment shown in Figure 5-16. Tests are realized in a low-rise of two-store building which has a concrete material that attenuates the signal power. The ipexSR software receiver is located in the first floor of the building to record visible satellite signals with different elevation angles. The assisted navigation data for the corresponding signals is stored in a reference network.

Figure 5-16: Indoor field test environment

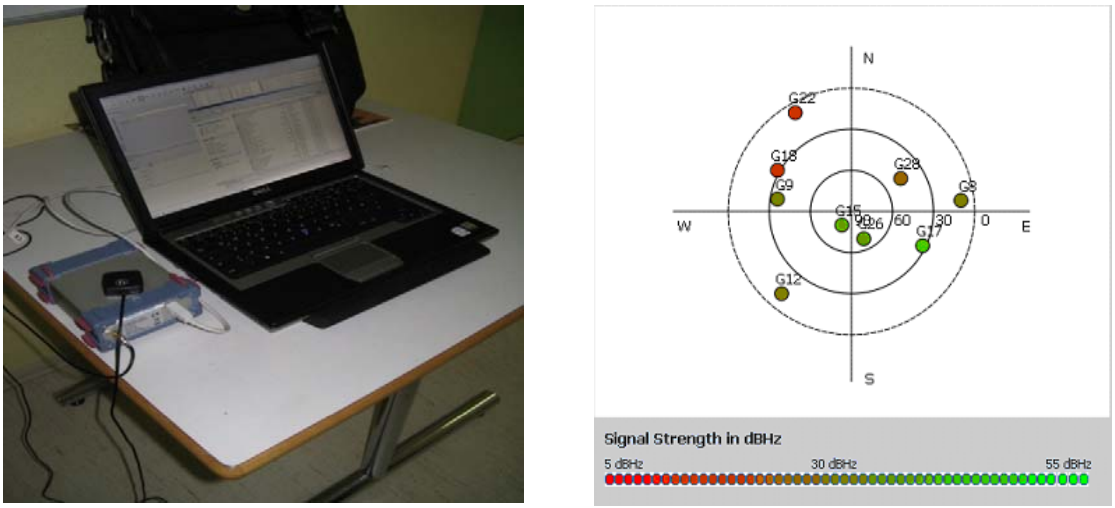


Figure 5-17: Test location and sky plot of satellites in the scenario

The test environment has three sides masked. For the scenario, zero-padded FFT acquisition technique described in 5.2.1 is evaluated with a static receiver for the PRN 26 using different $T_{coh}$ and $T_{unc}$ parameters. The acquisition performance is assessed by using the post correlation SNR, namely deflection coefficient at the output of the correlation. The post correlation SNR is calculated by

$$SNR_{post} = 10log10\left({R_{max}}^2/R_{ave}\right) \quad (5\text{-}7)$$

where $R_{max}$ is the maximum value of the correlation function and $R_{ave}$ is the post-correlation noise floor.

Correlation outputs of the PRN 26 and PRN 9 signal with respect to the FFT length is shown in Figure 5-18 and Figure 5-19. From this, optimum parameters can be determined to achieve the maximum post correlation SNR of the correlation output. Accordingly, by using same parameters except different $T_{unc}$ values (the total observation period becomes different for each case) are tested and as a result 100 ms of $T_{unc}$ provides the best performance.

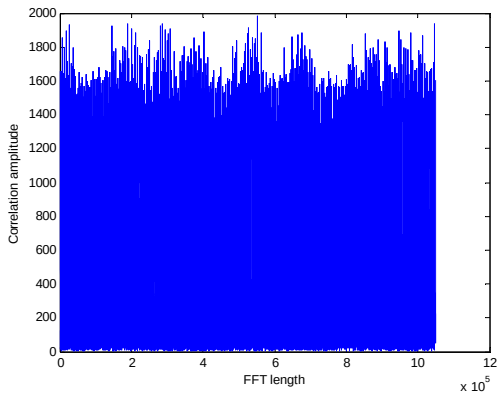


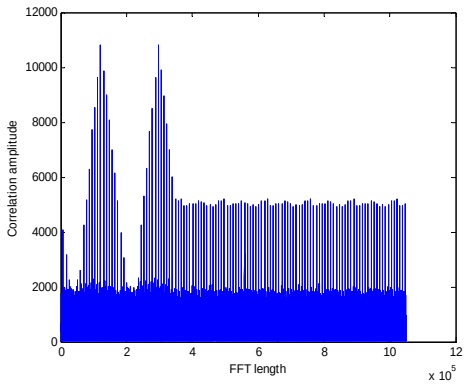


| | | | |
|---|---|---|---|
| $T_{coh}$: | 20 ms | $T_{coh}$ : | 20 ms |
| $T_{unc}$: | 200 ms | $T_{unc}$: | 100 ms |
| FFT order: | 20 | FFT order: | 20 |
| Post Corr. SNR | 10.3 dB | Post Corr. SNR: | 24.1 dB |

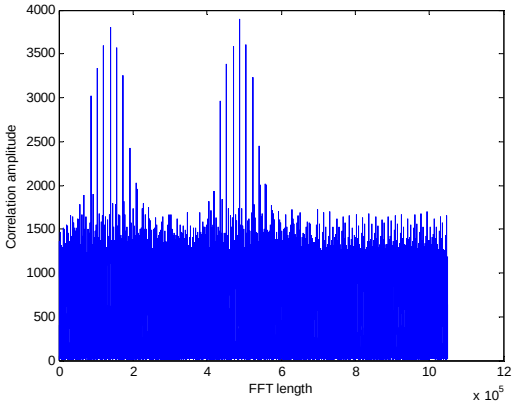


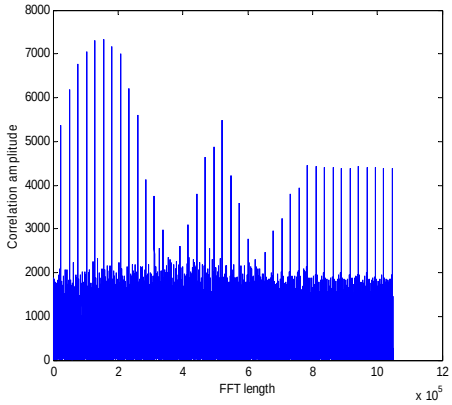


| | | | |
|---|---|---|---|
| $T_{coh}$: | 20 ms | $T_{coh}$ : | 20 ms |
| $T_{unc}$: | 40 ms | $T_{unc}$: | 20 ms |
| FFT order: | 20 | FFT order: | 20 |
| Post Corr. SNR | 11.58 dB | Post Corr. SNR: | 18.28 dB |

Figure 5-18: Amplitude of the correlator output versus FFT length for different $T_{coh}$ and $T_{unc}$ for PRN 26

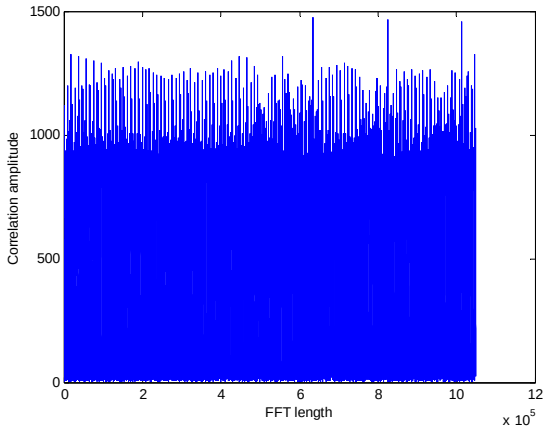


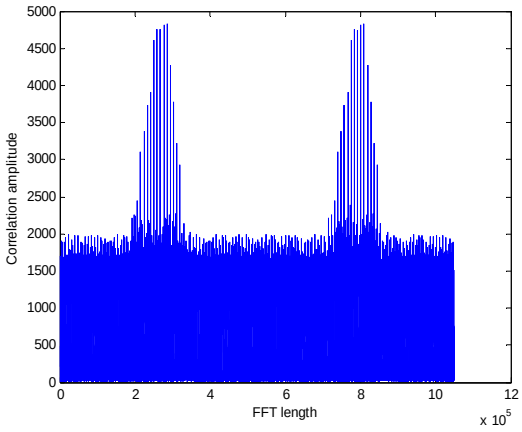


| | | | |
|---|---|---|---|
| $T_{coh}$: | 10 ms | $T_{coh}$ : | 20 ms |
| $T_{unc}$: | 100 ms | $T_{unc}$: | 100 ms |
| FFT order: | 20 | FFT order: | 20 |
| Post Corr. SNR | 14.72 dB | Post Corr. SNR: | 16.73 dB |

Figure 5-19: Amplitude of the correlator output versus FFT length for different $T_{coh}$ and $T_{unc}$ for PRN 9

## 5.4 Conclusion

Most commonly, the sensitivity of acquisition process is increased via extending the CIT. However, for signals having very long code length such as GPS L2C pilot signal, in the receiver their utilization via unassisted acquisition is tough. On the other hand, their lack of data or overlay code modulation allows theoretically unlimited integration time which gives higher sensitivity. In this chapter, the long CIT dependency on three error sources, namely clock jitter, line of sight movement and multipath fading has been presented. The analysis showed that with any oscillator type, signal detection is mainly effected from non-linear carrier phase variations. It has small influence on Doppler frequency and code phase change. With OCXO clock, the receiver sensitivity is 3 dB less than the receiver sensitivity with ideal clock and it gives the best sensitivity among Cesium and Quartz clocks since it is the most stable one in short time period of 1.5 s. The average sensitivity loss with Cesium and Quartz clocks are 3.3 dB and 4 dB respectively for detection probability of 90%.

Line of sight acceleration results indicate that Doppler frequency is negatively influenced by the increase of the line of sight acceleration. On the other hand its effect on code phase is rather small. The sensitivity loss with line of sight accelerations of 0.01 $m/s^2$ and 0.05 $m/s^2$ is about 1 dB and 2.4 dB respectively. The distance taken in 1.5 s with these accelerations are below the quarter wavelength of L2CL code, therefore non-linear carrier phase variations are below this limit and cause no challenge in terms of signal detection.

The channel results show that Rayleigh fading causes 15 dB acquisition sensitivity loss and this is the major sensitivity loss among all error sources studied. This indicates the significance of absence of line of sight signal on acquisition performance.

# CHAPTER 6. ACQUISITION IN THE PRESENCE OF INTER-FREQUENCY INTERFERENCE

GNSS dependency is increasing rapidly for many systems such as Intelligent Transport System (ITS), fisheries Vessel Monitoring System (VMS), rail transportation, precision agriculture, surface mining, GNSS based trackers, defense sector etc. These systems possess GNSS receivers in their infrastructures to report their real-time position to a related organization. Depending on the application domain, GNSS signals can be affected from different interference or jammer sources. If the interference or jammer signal power is larger than the processing gain (the resistance of the receiver to interference) of the system, then reliable transmission of GNSS signal is no more possible. The direct sequence spread spectrum (DS-SS) processing gain is around 60 dB and if the interference signal power is 40 dB higher than the noise floor, then loss of lock occurs on the GNSS receiver. There are two main approaches in order to increase the processing gain of the system; namely cross correlation protection and different interference mitigation approaches applied in the receiver. With new GNSS signals, greater cross correlation protection with reduced interference level is provided due to their code structure. However, since the noise level is higher than the GNSS signal power level by about 20 dB, various interference mitigation techniques are required in the receiver especially for Safety of Life (SoL) applications where integrity and accuracy of the signal is crucial. In addition, ICAO [64] provides requirements stating that the estimated $\mathrm{C/N_0}$ should be above the minimum required $\mathrm{C/N_0}$ depending on the desired signal characteristics and no loss of lock on carrier phase tracking occurs in the receiver. The aforementioned processing gain metric can be calculated by using the margin of DS-SS systems as:

$$M_i = G_p - L_{imp} - C/N_{0_{acq}} \tag{6-1}$$

where $\mathrm{G_p}$ is the processing gain, $\mathrm{L_{imp}}$ is the system implementation loss and $\mathrm{C/N_{0_{acq}}}$ is the acquisition sensitivity (i.e. minimum required $\mathrm{C/N_0}$).

In the front-end, the interference directly affects the operation of automatic gain control (AGC) unit and LNA. In the baseband, it gives degradation on acquisition correlation magnitude and affects the code and carrier tracking loops. There are two types of interferences sources; namely

unintentional and intentional sources such as jammers/spoofers [65], [66], [67], [68], [69]. Unintentional sources cover inband pulse signal interference (PSI) e.g. DME/TACAN, UWB, ATC/radar. Continuous wave interference (CWI) signals are classified under both type of interference. In terms of unintentional interference sources, CWI is more challenging to mitigate at the receiver compared to PSI signals. Harmonics from Very High Frequency Communications (VHF), amateur radio harmonics and TV sound/video carrier harmonics can be modeled as CWI. Another interference source, chirp jammers (CJ) are non-stationary signals and classified under intentional sources. Chirp signals present a change in frequency with time, that is characterized by the slope of the chirp signal (rate of change on the frequency) and its initial frequency. Other than chirp jammers, spoofers are also a threat, however spoofing attacks are rarer. The spoofing waveform might be a replica of the GNSS signal, appearing like a true signal and cause slowly varying time, phase and pseudo-range errors.

In the literature, a number of interference excision algorithms have been presented. In [22], [23] pulse blanking is proposed due to the lack of pulse detector requirement to identify the beginning and end of pulse and simple to implement which is convenient for a real-time GNSS receiver design. In [70], hybrid blanking which combines main features of blanking and notch filtering is proposed against pulse interference. In [24], a combination of pulse blanking and wavelet based mitigation algorithm is proposed and in the presence of strong DME signal, wavelet based method reveals worse than blanking. This is due to the Daubechies mother function that is not a perfect match to the DME signal characteristic and hence the residual interference remains which increases the noise floor. In case of a low DME interference, the contrary takes place. However, in the majority of the related literature, processing time analyses of methods are not considered which is essential for a real-time receiver.

This chapter aims to analyze the effect of unintentional interference sources and jammers on GNSS receivers. In order to provide some interference immunity at the receiver, against CWI adaptive time filters (e.g. notch filters) and against PSI, pulse clipping/blanking and wavelet transformation based techniques and against chirp jammer (CJ) Fractional Fourier Transform (FrFT) based excision are analyzed considering processing time.

## 6.1 Signal Model

The interfered signal $r_m$ of the i-th satellite after front-end can be modeled as

$$r_m = \sqrt{2P_i}c(t_m f_{c,i} - \tau_i)d(t_m f_{c,i} - \tau_i)cos(2\pi(f_{IF} + f_{D,i})t_m - \phi_i) + \sqrt{2J_i}cos(2\pi f_j t_m - \phi_{j,i}) + n_{IF,m} \quad (6\text{-}2)$$

where $m$ is the sample index, $d$ is the navigation data message, $\{P_i, \tau_i, \phi_i\}$ stands for the power, code delay in chips and carrier phase of the i-th satellite signal and $\{J_i, \phi_{j,i}\}$ stands for the power and carrier phase of the interference signal. $c$ is the PRN code, $f_{c,i}$ is the code rate in chips/s, $f_{IF}$ is the IF frequency, $f_j$ is the interference frequency, $f_{D,i}$ is the Doppler frequency, $t_m$ is the time of sample in [s], $n_{IF,m}$ is the real valued white Gaussian noise. The worst case interference occurs when the whole power of the interference is located in the coordinates of the GNSS signal, namely the phase and the carrier frequency. Hence, in the worst case $f_{IF} + f_{D,i} = f_j$ and $\phi_i = \phi_{j,i}$ and the Rx signal becomes

$$r_{w,m} = [\sqrt{2P_i}c(t_m f_{c,i} - \tau_i)d(t_m f_{c,i} - \tau_i) + \sqrt{2J_i}\,]cos(2\pi(f_{IF} + f_{D,i})t_m - \phi_i) + n_{IF,m} \quad (6\text{-}3)$$

Later, $r_{w,m}$ signal is processed in pre-correlation mitigation module as represented in Figure 6-1.

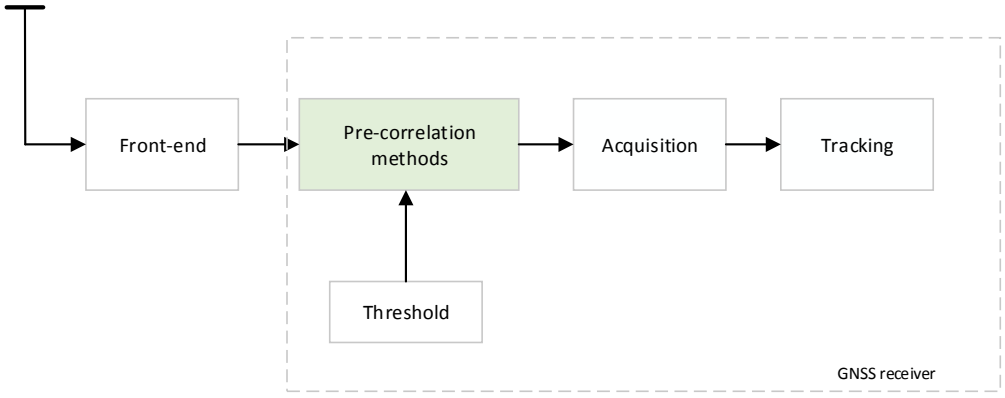


Figure 6-1: Block diagram of pre-correlation mitigation

## 6.2 Interference Signal Types

In real environments, there are various types of interference signals. It can be narrowband, broadband, wideband depending on the receiver's bandwidth or it can be pulsed, or having a changing frequency like chirps. The potential sources of interference on GNSS signals are summarized in Figure 6-2. Among them three types of interference signals are considered and analyzed which is pulse, continuous wave and chirp interference.

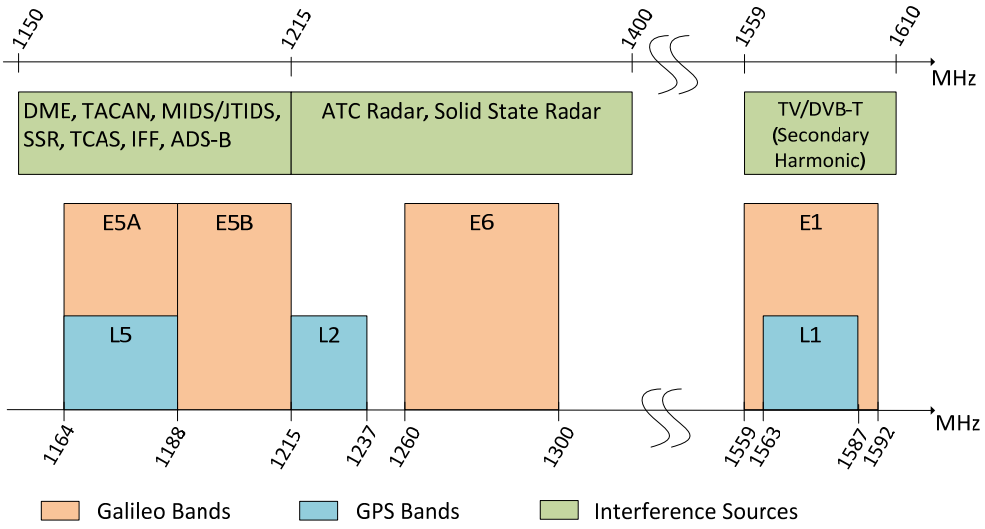


Figure 6-2: Interference Sources on GNSS L-band

Recently, commercial in-car jammers become frequently used. They are intentionally used in critical applications according to the Volpe report [71] that prevents a tracking device in the vehicle for determining location/speed, road tolling but also disrupting GNSS signals. Most of them have a chirp signal characteristic and only a few of them are continuous wave signals. The intentional and unintentional interference signals in the GNSS band are tabulated in Table 6.1.

Table 6.1: Interference signals on GNSS L-band

| Interference type | System | Interfered signal band | Types |
|---|---|---|---|
| LTE | Light squared | E1/L1 | Light-Squared-like |
| ARNS (Aeronautical) | DME | E5/L5 | Pulse |
| | Tactical Air Navigation (TACAN) | | |
| | JTIDS/MIDS | | |
| | Multifunction Information Distribution System (MIDS) | | |
| RADAR | Air traffic control radar (ATC) | L5/E5/E6 | Pulse |
| Harmonics | TV channels | E1/L1 | CWI |
| | Terrestrial Trunked Radio | | |
| | Digital Video Broadcasting - Terrestrial (DVB-T) | | |
| Commercial jammers | In-car jammers | L1/L2 | CWI/Chirp |
| Others | Ultra Wide Band (UWB) | L1/E6 | Pulse |

### 6.2.1 Pulse Interference

Pulse interference occurs only for a short time; however it may affect GNSS receivers in a large extent if the interference signal is characterized by high power with a large duty cycle. The impact on the GNSS signal can be kept at a minimum by applying proper signal processing techniques such as pulse blanking, clipping or some advanced techniques like Wavelet transformation based excision. The potential pulse interference sources on GNSS L-band are summarized as follows:

- *DME / TACAN*

The aeronautical L-band is branched into 1 MHz channels that are in use by aeronautical navigation aids like the DME that provides slant range distance (straight line distance from the aircraft to the ground station) to an aircraft by measuring the total round-trip time between

Gaussian pulse pair interrogations transmitted from an aircraft and replies from a ground transponder. When an aircraft is landing, the ground transponder receives interrogation pulses, regenerates and transmits pulse pairs with a time delay of 50 µs. The aircraft transmits interrogation pulses with a random pulse repetition frequency (PRF) around 120-150 Hz, however regardless of the interrogation rate, the DME ground transponder transmits 2700 pps [72], [73].

Table 6.2: DME signal characteristics

| Pulse rise | Pulse width | Pulse fall | Pulse spacing | PRF |
|---|---|---|---|---|
| 2 µs | 3.5 µs | 2 µs | 12 µs | 2700 |

An ideal DME pulse pair $S(t)$ is defined by two Gaussian pulses as follows:

$$S(t) = e^{-\frac{\alpha}{2}(t)^2} + e^{-\frac{\alpha}{2}(t-\Delta t)^2} \tag{6-4}$$

where $\Delta t$ is the pulse spacing of 12 µs and α is a constant of 4.5 x 10 $s^{-2}$.

Within four modes of DME (X, Y, W, Z), only X-mode interferes to E5 band occupying between 1151-1215 MHz. The characteristics of DME pulse pair is tabulated in Table 6.2. As different from DME, TACAN provides bearing (azimuth) and slant-range information to military aviation with more precise range information. It has the same pulse pair characteristics considering DME with a distinction of PRF of 3600 pps. The DME signal interfered into GNSS signal can be expressed as

$$S_{DME}(t) = P_I \sum_{n=1}^{N} (e^{-\frac{\alpha}{2}(t-t_n)^2} + e^{-\frac{\alpha}{2}(t-\Delta t-t_n)^2}) cos(2\pi f_{DME} t + \theta_{DME}) \tag{6-5}$$

where $P_I$ is the DME interference peak power at the GNSS receiver antenna, $f_{DME}$ is the carrier frequency of the DME signal and $\theta_{DME}$ is the carrier phase of DME signal.

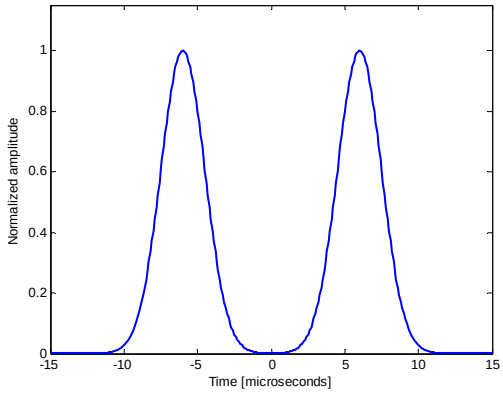


Figure 6-3: DME pulse pair

- *Ultra-Wideband*

Impulse radio – ultra wideband (IR-UWB) systems have very short duration pulses and low duty cycle with a large bandwidth, defined to be larger than 500 MHz [74]. The UWB signal generally appears as a noise floor increase in GNSS receivers deteriorating the positioning accuracy. However, in one of the recent studies [75], UWB signals with specific Pulse Repetition Frequency (PRF) of 19.94 MHz cause similar to CWI effect on GNSS receivers is illustrated.

- *JTIDS/ MIDS*

The Joint Tactical Information Distribution System (JTIDS) is an L-band TDMA system used by the armed forces of USA. The Multi-functional Information Distribution System (MIDS) is used by NATO in the frequency range of $890 - 1215$ MHz. In worst case scenarios, JTIDS system gives around 2 dB $C/N_0$ degradation on GNSS receiver sensitivity [76] .

- *ATC Radar*

The Air Traffic Control (ATC) radar transmits pulse signals consisting of two radar systems, namely the most prominent component of Primary Surveillance Radar (PSR) and Secondary Surveillance Radar (SSR). ATC PSR emits pulse signals in the frequency range of 1250-1310 MHz. The transmitted impulse signals are reflected by the target and received by the same PSR unit. On the other hand, SSR works with respect to a different principle; it transmits and receives

impulses, namely interrogation. This means that the reflection from target is not only a reflection, but also the signal is received and processed by the target by means of transponders.

### 6.2.2 Continuous Wave Interference

CWI is another type of jammer, appearing in the spectrum as an RF spike. The susceptibility from CW interference sources is much more significant than those originated at pulse interference sources. If CWI exists, it is inevitable that it blocks the process of GNSS receiver. The Jamming to Signal Ratio (JSR) of greater than 40 - 50 dB prevents the GNSS receiver to obtain a position. A narrow band CWI can be written as follows:

$$s_{CWI}(t) = Acos(2\pi f_c t + \phi) \tag{6-6}$$

where A is the interference signal amplitude, $f_c$ is the frequency offset from the carrier frequency of the desired GNSS signal and $\phi$ is the initial phase of the interference signal. The potential CWI sources on GNSS L-band are summarized as:

- *TV/ Video Harmonics*

Certain analog TV channels which are more powerful than digital TV transmitters generate harmonics which causes interference to GNSS receivers. The 2nd harmonics are UHF CH 66 in the range of [782-788] MHz, UHF CH 67 within range of [788-794] MHz. The 3rd harmonics are UHF CH 22 in the range of [518-524] MHz and UHF CH 23 in the range of [524-530] MHz. The main interference source to GNSS receivers is the 3rd harmonic of UHF CH 23 that is close to the GPS L1 frequency having a video carrier of 525.25. This corresponds to the 33 spectral line of the C/A code described in [77] and [78] .

- *Amateur Radio Harmonics*

The harmonics on GNSS band exist only due to American amateur radio band and there is no harmonics caused by European radio amateur channels on L1 band. The solely harmonics caused by European radio amateur is on military L2 band [77].

- *FM Harmonics*

Certain FM emitters in the range of 87.5-108 MHz have their harmonics on GNSS band. The 15$^{th}$ harmonics of CH at 104.9 MHz and at 105.1 MHz FM interference may have an effect in the radius of 5 km [77].

- *LDACS*

The L-band Digital Aeronautical Communications System (LDACS) is currently under development for the modernization of future Air-Traffic Management (ATM) in aviation and is foreseen to be in service for the year 2020. There is a potential interference between these systems with GNSS in the frequency range of 960-1164 MHz. The most severe scenario could be LDACS air to ground or air to air transmission into a GNSS receiver on the same aircraft [79].

### 6.2.3 Chirp Jammer

Chirp signal is a non-stationary signal that presents a change in frequency within time. It is characterized by the slope of the chirp (rate of change on the frequency). A chirp signal can be modeled as follows:

$$s_{CI}(t) = Acos(2\pi f_c(t)t + \phi) \tag{6-7}$$

where $f_c(t)$ is the time-varying frequency-offset.

The majority of commercial jammers have chirp signal characteristics such as one-saw tooth function, multi-saw tooth function and with frequency bursts as defined and analyzed in [80]. In the thesis, the most commonly used jammer that has one positive saw-tooth function for describing the instantaneous frequency is used.

## 6.3 Interference Detection and Transform Metrics

A common approach to detect the interference signal in GNSS receiver is the Automatic Gain Control (AGC) monitoring. In the receiver, AGC is used to minimize the quantization loss. It is driven by the ambient noise environment rather than the signal power [23] where the signal power is below that of the thermal noise floor; hence AGC can be used as an interference

detection tool. Further, the spectral behavior of the signal can be estimated by simply using the power spectral density or by FFT analysis. Another interference detection technique is performed by monitoring acquisition and tracking performance. Acquisition metrics in the presence of interference have been defined by [81]- [82]. The first metric $\gamma_m$ is the ratio of the largest $R_{fp}$ and the second largest correlation peak $R_{sp}$ in the search domain that is described by:

$$\gamma_m = 10\, log_{10}(\frac{R_{fp}}{R_{sp}})^2 \tag{6-8}$$

The second commonly used metric is the ratio of the largest peak to the mean peak $R_{mp}$ defined as:

$$\gamma_m = 10\, log_{10}(\frac{R_{fp}}{R_{mp}})^2 \tag{6-9}$$

Most commonly, interference estimations are measured via $C/N_0$ metric at the output of acquisition and tracking correlators.

The spectral behavior of the interference signal is estimated by various transformations. To address the problem of a changing interference, an adaptive transform unit could be used where all possible transform combinations are evaluated. For the transform domain switching metric, compression gain (or namely coding gain) can be used to measure how well a transform can suppress the interference signal. With a larger compression gain, in the transform domain more signal energy is localized into a smaller number of bins, hence it becomes simpler to excise the interference without deteriorating the desired signal. The compression gain can be computed via [83]

$$\mathrm{r_{TCG}} = \frac{\frac{1}{\mathrm{L}}\sum_{\mathrm{l}=1}^{\mathrm{L}}|\mathrm{s(n)}|^2}{\sqrt[\mathrm{L}]{\prod_{\mathrm{l}=1}^{\mathrm{L}}|\mathrm{s(n)}|^2}} \tag{6-10}$$

where $L$ is the segment length and $s(n)$ is the Rx signal either the time domain signal or the transform bin samples. Based on this metric, the best performance is chosen to excise the interference. However, this metric may lead a large computational complexity if there are many transformations used. It is noteworthy that this approach may fail if the interference is changing more rapidly than the time required to search over various transformations. If $\mathrm{r_{TCG}} = 1$, then it

means that the spectrum is flat and the transform could not be able to concentrate the interference signal.

## 6.4 Pre-correlation Interference Suppression Techniques

*Pre-correlation* techniques are applied before the acquisition stage. These techniques can provide more effective protection against interference with respect to *post-correlation* techniques and require no modification on the implementation of GNSS receiver. Pre-correlation methods give better performance and have lower complexity, however require interference-free segment of signal in order to extract statistical signal properties. These methods are based on thresholding or spatial filtering with eigenvalue decomposition or adaptive cancellation with an antenna. A summary of studied methods is presented in Table 6.3.

Table 6.3: Summary of pre-correlation interference suppression methods

| Interference signal | Transform domain | Methods used |
|---|---|---|
| Pulse | Time, FFT, Wavelet | Clipping, Blanking, STFT-FCME, Wavelet based blanking |
| Continuous Wave | FFT | STFT-FCME, Notch filtering |
| Chirp | FFT, STFT, FrFT | FrFT based blanking |

In this section, it is assumed that the receiver has no a-priori information about interference signal power and blind acquisition is performed to acquire the GNSS signal. In the following, mitigation techniques against PSI, CWI, chirp jammers are introduced. The performance of algorithms is analyzed based on parameter optimizations of the computational complexity, the threshold determination and the efficiency of each algorithm.

### 6.4.1 Conventional Approaches of Clipping and Blanking

One of the well-known methods applied on navigation receivers to mitigate the impact of pulse interference is clipping as shown in Algorithm 6-1. In this method, peaks of interference signal with high power are cut off. The clipping method has two counteracting effects; reduction on the radiated interference signal power (not able to completely cancel the interference signal) and

impairments on the desired GNSS signal. As a consequence, this trade-off can be balanced by optimizing the threshold merit where the amplitude of samples is clipped at a certain threshold $T_{clip}$. The clipping operation on the digital IF signal $r_\mu$ yields

$$r_\mu^{clip} = \begin{cases} r_\mu & \|r_\mu\|^2 < T_{clip} \\ T_{clip} & \|r_\mu\|^2 \geq T_{clip} \quad \mu = 0, \dots, L-1 \end{cases} \tag{6-12}$$

where $L$ is the number of IF samples

After the threshold is applied, the resulting IF signal can be analyzed in two parts; namely, the deformed signal and the desired signal. This yield:

$$r_\mu^{clip} = \varphi s_\mu + y_\mu \tag{6-13}$$

where $\varphi$ is the attenuation factor due to clipping on the desired signal, $s_\mu$ is the desired IF signal and $y_\mu$ is the deformed signal. The deformed signal is the sum of the remaining interference signal, the distortion induced by clipping and AWGN. The threshold is used to clip the amplitude of interference signal samples, however it also clips the desired signal and the noise contained in the combined digitized IF signal. The threshold is determined by means of simulations with one type of interferer (e.g. DME) having different power levels. The optimum threshold value is determined by comparing the spectrum of the clipped interfered signals, namely the desired signal and various DME signal power levels with spectrum of the desired signal (without DME interference). For low clipping thresholds, the Signal to Interference plus Noise Ratio (SINR) before clipping operation can be smaller than the SINR achieved after the clipping. This is due to the strong distortion induced on the desired GNSS signal when applying clipping on the IF signal. For high clipping thresholds, the interference power is not reduced and no desired IF samples are distorted, hence almost the same SINR before and after are achieved.

In Figure 6-4, the $C/N_0$ of the interfered E5a signal is shown after applying clipping to different levels. When the signal level is set with respect to 2, then the maximum estimated received signal power is achieved.

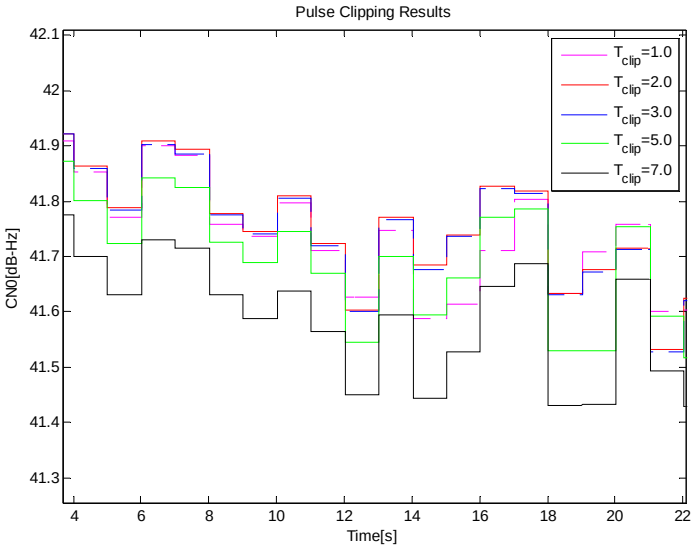


Figure 6-4 $C/N_0$ versus time of DME signal after clipping to different levels

***Input:*** $r_\mu$ *digitized IF signal*
***Output:*** $r_\mu^{clip}$ *clipped IF signal*

*1: Estimate mean power of IF samples that comprise interference and GNSS signal*
*2: Set the clipping threshold*
*3: Compare the threshold w.r.t mean power of IF samples*
*4: Clip the amplitude of peaks in which mean signal power is greater than the threshold value*

Algorithm 6-1: Clipping algorithm

Table 6.4: Computational complexity of pulse clipping method

| Computation | Operation | Size | Cost |
|---|---|---|---|
| Thresholding (e.g. $T_{clip} < \lvert r_\mu \rvert$) | L number of comparisons | L | O(L) |
| $T_{clip}$ | m number of multiplications | m | O(m) |

In Table 6.4, the computational cost of clipping is presented. *L* denotes number of time samples and *m* denotes number of samples whose values are greater than the threshold. The clipping

method essentially reduces the interference signal power and offers some advantages over blanking approach:

- Interference signal power is reduced
- For an efficient clipping, the interference signal must be detected accurately from the Rx signal
- Easy to be implemented
- For small power interferers, almost no benefit is expected from clipping process.

In time domain, pulse blanking is the commonly used approach where the signal is blanked when the average power of the signal is greater than a certain threshold $T_{blank}$. The principle of pulse blanking is:

$$r_{\mu}^{blank} = \begin{cases} r_{\mu} & \|r_{\mu}\|^2 < T_{blank} \\ 0 & \|r_{\mu}\|^2 \geq T_{blank} \end{cases} \quad \mu = 0, \dots, L \tag{6-14}$$

In GNSS receivers, mostly pulse blanking with AGC monitoring is used. Since GNSS signal is below the noise floor, the AGC is driven by the noise or the interference signal instead of the GNSS signal. In this way, interference signal is the main source that changes the AGC gain, hence can be used as a tool for interference detection. In case of pulse interference, the AGC has to charge fast to follow the rising edge of the pulse signal and avoids the saturation. In other words, in order to excise the pulse interference, AGC gain has to be adjusted such that the recovery time is small enough. Attack and recovery time is a design parameter in AGC which is typically in the range of 50 μs and 1 ms [46].

In blanking process, during the excision of interfering pulse, the desired signal is usually suppressed and thus no useful power can be extracted. However, it provides better interference signal suppression due to the deletion of interference signal rather than reduction to a certain amplitude. Similar to clipping, the blanking threshold is computed by means of simulations with pulse interferer having various power levels. The threshold is determined by comparing spectrums of blanked signals with the spectrum of the desired GNSS signal.

***Input:*** $r_\mu$ *digitized IF signal*
***Output:*** $r_\mu^{blank}$ *blanked IF signal*
*1: Estimate mean power of IF samples that comprise interference and GNSS signal*
*2: Set the blanking threshold*
*3: Compare the threshold w.r.t mean power of IF samples*
*4: Blank pulses which are greater than the threshold value*

Algorithm 6-2: Blanking algorithm

Table 6.5: Computational complexity of pulse blanking method

| Computation | Operation | Size | Cost |
|---|---|---|---|
| Thresholding and blanking (e.g. $T_{blank}<\lvert r_\mu \rvert$ ) | L number of comparisons | L | *O(L)* |

With blanking, interference signal power is reduced, however it is ineffective for weak pulse interference signal detection and thus these undetected pulses raise the noise level. There is also a strong impact on the desired GNSS signal since the power of the desired signal is attenuated. Table 6.5 shows the computational cost of the pulse blanking method.

### 6.4.2 STFT using Forward Consecutive Mean Excision

The Short-time Fourier Transform (STFT) excision method is used commonly to suppress narrowband signals; besides it can also be used against impulsive signals. STFT method namely 'windowed Fourier transform' is a time-frequency representation of the signal energy; it splits the non-stationary signal into small segments that are then assumed as stationary. This is achieved by multiplying the signal with a window function and then FFT operation is applied to the windowed signal. The windowing operation is applied to emphasize the signal around time $\tau$ and thus the Fourier transform reflect the distribution of the frequency around corresponding period of time. The excision is realized in frequency domain by applying Forward Consecutive Mean Excision (FCME) as shown in Algorithm 6-3. Then the signal is transformed into time domain by applying IFFT to enable feeding the correlation process. The FFT transformed signal can be represented as

$$R_t(w) = {}^{1}/_{2\pi} \int_{-\infty}^{+\infty} e^{-jw\tau} r(\tau) h(\tau - t) d\tau \tag{6-15}$$

where $r(\tau)$ is the received signal and $h(\tau)$ is the window function.

The time-frequency distribution P(t, w), namely spectrogram of the signal is achieved by an ensemble of spectra for different spectrum in different time sections. The time-frequency distribution at time $t$ can be written as

$$P(t,w) = |R_t(w)|^2 = \left|{}^{1}/_{2\pi} \int_{-\infty}^{+\infty} e^{-jw\tau} r(\tau) h(t-\tau) d\tau\right|^2 \quad (6\text{-}16)$$

There is a resolution tradeoff between time and frequency which is determined by the width of the window $h(\tau)$. Following the Heisenberg principle, a long window width provides good resolution in frequency domain and poor resolution in the time domain. This is due to the usage of a single window for all frequencies; hence the resolution is same for all locations in the time-frequency plane. The time domain DME interfered signal and its spectrogram is illustrated in Figure 6-5. Red bands indicate high energy frequency contents of the signal emphasizing the DME, since STFT concentrates the interference in a small area in the time-frequency domain. In Figure 6-6, the PSD of the CW interfered GIOVE E5a is represented and the CW interferer is identified with spikes. In the spectrogram, every spike is represented with the red band indicating the CW interferer.

In general, excision methods are based on the assumption that the noise variance is known a-priori or mean of the amplitude spectrum. However, such excision methods are valid if the interference power and bandwidth are fixed. As an excision method, FCME is studied.

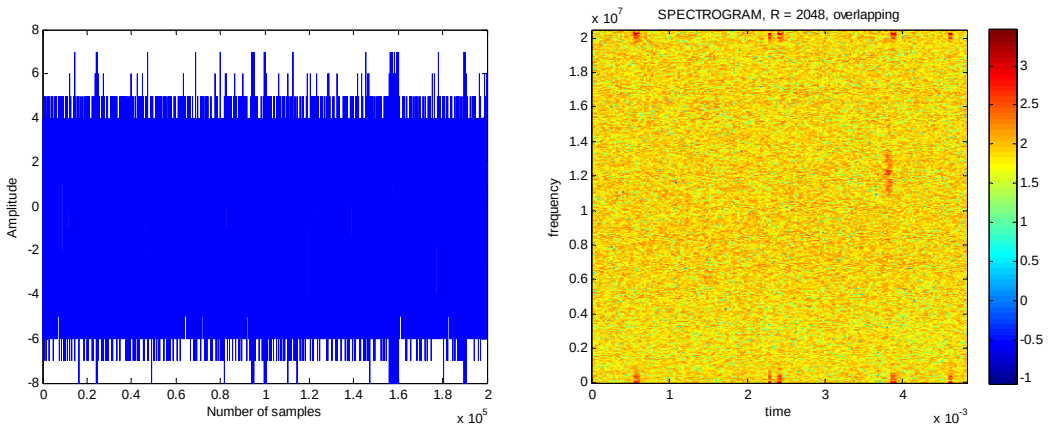


Figure 6-5: Magnitude and Spectrogram of DME plus GIOVE signal of PRN1

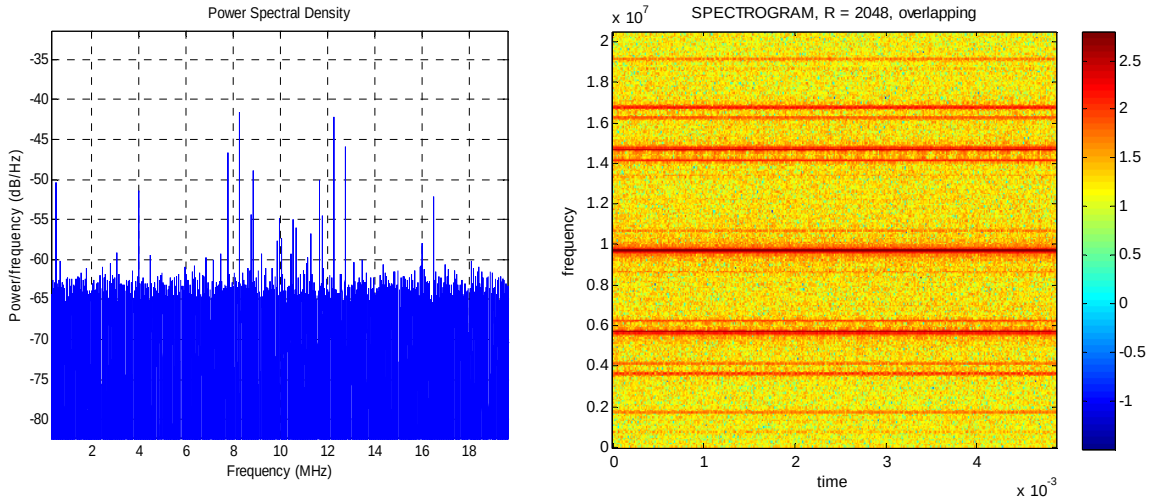


Figure 6-6: PSD and Spectrogram of CWI (-110 dBW) plus Giove signal of PRN1

The initial threshold value is calculated considering the a-priori information based on pure desired signal characteristics. Due to the iterative calculation of the threshold, performance of FCME is superior to notch filters. The FCME threshold [84] considering Gaussian distributed noise with a predefined $P_{fa}$ is calculated as:

$$T_{FCME} = \sqrt{\frac{4}{\pi}}\sqrt{-ln(P_{fa})} \tag{6-17}$$

where $P_{fa}$ is the desired false alarm probability which indicates the number of samples above the final threshold in the noise only case. If $P_{fa}$ is set to 5%, that is to say that on average 5 frequency bins are incorrectly detected to be interfered among 100 frequency bins. Note that scaling parameters of $T_{FCME}$ 1.95 and 2.97 are obtained using $P_{fa}$ of 5% and 0.1% respectively [85] within the assumption of Rayleigh distributed desired signal set. Briefly, FCME updates the threshold value in an iterative way and excise frequency bins which exceeds the threshold [85]. The FCME algorithm groups adjacent samples that are above the threshold $T_{low}$ and the largest element of this group is compared to $T_{high}$. If the largest element exceeds $T_{high}$ then it is decided that group of samples corresponds to interference. If the largest element is smaller than $T_{high}$, then it is decided that the group corresponds to the desired signal and noise.

**Input:** $R_t(w)$ *windowed FFT transformed signal*
**Output:** *Excised* $R_t(w)$ *signal*
*1: Rearrange the samples r in the ascending order (e.g. Heapsort) for the first iteration (m=0) as*
$y(0) = (y_0, y_1, \dots, y_N)$ *(6-18)*
*2: Choose M (set size) smallest samples to form the interference-free set and calculate the* $T_h$
$T_h = T_{FCME}\bar{y}(m)$ *(6-19)*
*The size of M is typically 10% of the size of the data set. Update* $y(m)$ *iteratively for the samples that are below the threshold* $T_h$ *where*
$\bar{y}(m) = \frac{1}{M}\sum_{i=1}^{M}|y_i|$ *(6-20)*
*3: Update the threshold* $T_h$ *until the maximum predefined number of iterations.*
$T_h = T_{FCME}\bar{y}_m$ *m=m+1* *(6-21)*
*4: Reset the interfered indexes exceeding* $T_h$

Algorithm 6-3: FCME algorithm

***Input:*** *Digitized IF signal*
***Output:*** *Interference-free IF signal*
*1: Read M samples of the input signal*
*2: Multiply samples point wise by the analysis window* $h(n)$ *having a length of* M
$\tilde{r}(n) \triangleq r(n)h(n) \qquad n = -\frac{M-1}{2}, \dots, \frac{M+1}{2}$ *(6-22)*
*3: Extend the windowed sequence with zeros from both ends to the length of FFT*

$$\widetilde{r'}(n) = \begin{cases} \tilde{r}(n), & |n| \le \frac{M-1}{2} \\ 0, & \frac{M-1}{2} < n \le \frac{N}{2} - 1 \\ 0, & -\frac{N}{2} \le n < -\frac{M-1}{2} \end{cases} \quad (6\text{-}23)$$

*4: Take the FFT of* $\widetilde{r'}(n)$ *to obtain the STFT of* $r(n)$
$R_k\left(e^{j2\pi k\left(\frac{f_s}{N}\right)}\right) = \sum_{n=-\frac{N}{2}}^{\frac{N}{2}-1}\tilde{r}'(n)e^{-j2\pi k(f_s/N)nT}$ *(6-24)*
*where* $f_s$ *is the sampling rate and* $k$ *is the STFT bin index*
*5: Apply the FCME algorithm to excise interfering bins in the Rx signal*
*6: Convert the signal from STFT to time domain*

Algorithm 6-4: STFT-FCME algorithm

In general, the FFT method is based on the divide-and-conquer approach and the N-point FFT takes the operation of O(NlogN). In Table 6.6, the computational complexity of STFT method with FCME is illustrated. Herein, M denotes the window width of the STFT method. With STFT-FCME, there is a resolution trade-off between time and frequency. It is difficult to identify low frequencies with short windows (poor frequency resolution) and with long windows, short pulses can be poorly localized in time.

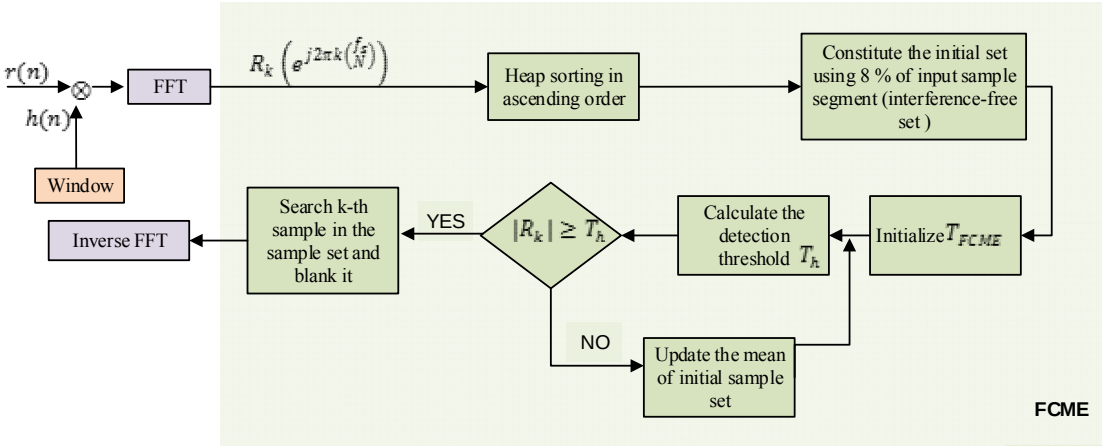


Figure 6-7: STFT-FCME flow diagram

Table 6.6: Computational complexity of STFT with FCME method

| Method | Computation | Operation | Cost |
|---|---|---|---|
| STFT | $r(n)h(n)$ | Windowing | $O(M)$ |
| | $\sum_{n=-N/2}^{\frac{N}{2}-1} \tilde{r}'(n)e^{-j2\pi k\left(\frac{f_s}{N}\right)nT}$ | FFT operation | $O(MlogM)$ |
| FCME | $(y_0, y_1, \dots, y_N)$ | Sorting (Heapsort method) sample amplitudes for *m* number of iterations | $O(mNlogN)$ $\cong O(NlogN)$ |
| | $T_{CME}\frac{(1.95)}{M}\sum_{i=1}^{M}\lvert y_i\rvert$ | Scalar multiplication and sum operation for m number of iterations | $O(mM)$ |
| | $(0.y_i, \dots, 0.y_j)$ | Reset interfered frequency bins | $O(M)$ |
| Inverse STFT | $\frac{1}{N}\sum_{p=-N/2}^{N/2}\tilde{r}'\left(e^{j2\pi k\left(\frac{f_s}{N}\right)}\right)e^{j2\pi k\left(\frac{f_s}{N}\right)nT}$ | Inverse FFT operation | $O(MlogM)$ |

### 6.4.3 Wavelet Transformation based excision

One of the sophisticated techniques used for time-frequency analysis is the wavelet transform. In comparison to the STFT method; continuous wavelet transform provides more flexibility on time and frequency resolution. In STFT, the window width is same for all locations in the time-frequency plane whereas in wavelet transform by using dilation and translation of wavelet mother function, the window width is variable. The wavelet transform uses long windows at low frequencies and short windows at high frequencies.

The theory of wavelets was described initially in [86], herein some basic notations of wavelet transformation is illustrated. Wavelet transform decomposes a signal into a set of basis functions called as wavelets that are obtained from mother wavelet by using scaling and dilation. Wavelets are mathematical functions that split data into different frequency components and then study each component with a resolution matched to its scale [87]. The continuous wavelet transformation for a function f(t) is defined as [88]

$$W(s,d) = \int_{-\infty}^{+\infty} f(t)\Phi_{s,d}^{*}(t)dt \tag{6-25}$$

where * denotes the complex conjugation and $\Phi_{s,d}^{*}(t)$ is called the wavelet. The variables *s* and $d$ are scale and dilate of the mother function $\Phi(t)$ to generate wavelets according to:

$$\Phi_{\mathrm{s,d}}(\mathrm{t}) = \frac{1}{\sqrt{\mathrm{s}}}\Phi(\frac{\mathrm{t-d}}{\mathrm{s}}) \tag{6-26}$$

The scale variable $s$ gives the width and dilation $d$ shows the position of the wavelet. The inverse transform can be obtained through

$$f(t) = \int_{-\infty}^{+\infty}\int_{-\infty}^{+\infty} W(s,d)\Phi_{s,d}(t)ddds \tag{6-27}$$

In discrete wavelet transform (DWT), the mother function modifies to

$$\Phi_{s,d}(x) = 2^{-s/2}\Phi(2^{-s}x - d) \tag{6-28}$$

where $s$ and $d$ are integers.

Due to different time and frequency resolution in DWT, Heisenberg boxes for each coefficient do not have the same height and width as shown in Figure 6-8.

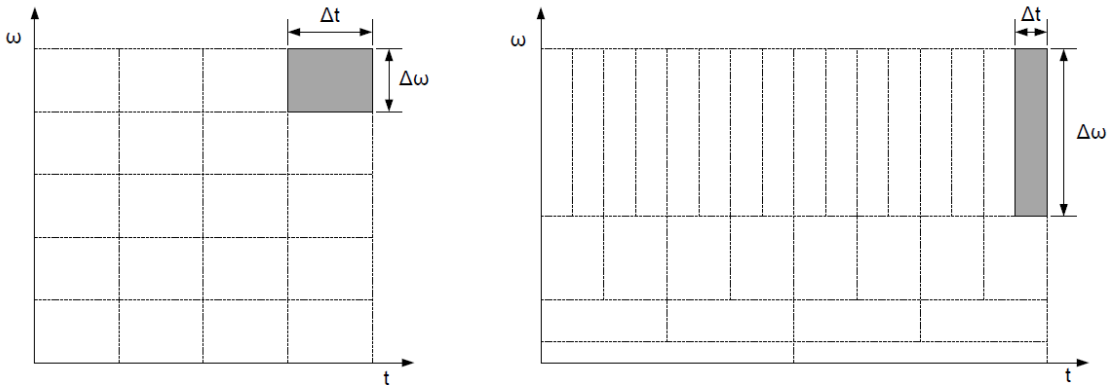


Figure 6-8 STFT (left hand) versus DWT time-frequency plane [89]

In the field of GNSS, signals transmitted from satellites reach the receiver antenna with a very low signal power and considering that the noise level is much higher than the signal power around 20 dB. The small wavelet coefficients indicate mainly the desired GNSS signal and large coefficients yield the interference signal.

***Input*:** $r_\mu$ digitized IF signal
***Output:*** Interference-free IF signal
*1: Read* M *samples of the input signal*
*2: Transform Rx signal samples to wavelet basis*
*3: Set the detection threshold*
*4: Set the coefficients that are above the predefined threshold to zero, whereas smaller coefficients representing GNSS signals are preserved*
*5: Shift the wavelet along the signal to the next block*
*6: Reconstruct the signal from excised DWT coefficients that indicates the estimate of the original signal*.

Algorithm 6-5: DWT algorithm

Briefly, using DWT, IF samples are transformed into wavelet domain and processed considering a certain wavelet mother function. Next, blanking is applied to the processed output and then inverse transform is applied. One of the outcomes of this section is that with the wavelet transform method, interfering pulses are detected with higher precision with respect to the pulse

blanking method; on the other hand it causes a big computational load at the receiver. The pseudo code of the DWT algorithm is represented in Algorithm 6-5.

### 6.4.4 Fractional Fourier Transform based mitigation

The fractional Fourier transform (FrFT) is a generalization of the Fourier transform. It was introduced by Namias [90] and mathematically defined by McBride and Kerr [91]. An alternative definition was proposed by Lohmann [92]. Later, Almeida [93] provided steps to describe the computation of FrFT. Then, optical interpretations and discrete implementation of FrFT were suggested by Ozaktas [94]. FrFT has widespread literature coverage mostly in the field of optics, but it remains completely unknown in the field of GNSS navigation.

For suppression of chirp signals, fractional Fourier transform (FrFT) is an appropriate domain since FrFT basis functions are formed by chirp signals, likewise sinusoidal signals and mother wavelet forms the FFT and DWT basis functions respectively. Briefly, FrFT is a rotation of the signal in the time-frequency plane; hence it measures the angular distribution of the signal's energy in this plane [94]. With respect to the classical Fourier transform, using FrFT a significant performance gain is achieved due to the additional degree of freedom that is the order of the transform. Every property of the classical Fourier transform is a special case of FrFT, therefore there exist an improvement potential in the areas where classical Fourier is used. Mathematically, the a-th transform order FrFT of a signal $r(t)$ can be defined as

$$R_a(u) = F^a\{r(t)\}(u) = \int_{-\infty}^{\infty} r(t)K_a(t,u)dt \tag{6-29}$$

FrFT is defined using a transformation kernel. The kernel function, namely the projection term $K_a(t,u)$ equals to

$$K_a(t,u) = \begin{cases} \sqrt{\frac{1-jcot(\alpha)}{2\pi}}\, exp\left(j\frac{t^2+u^2}{2}\cot(\alpha) - jut\ csc(\alpha)\right), & \alpha \neq k\pi \\ \delta(u-t), & \alpha = 2k\pi \\ \delta(u+t), & \alpha = (2k+1)\pi \end{cases} \tag{6-30}$$

$$a = \frac{2}{\pi}\alpha \tag{6-31}$$

where $a\{0 \leq a \leq 1.0\}$ defines the transform order and $\alpha$ is the rotation angle. The FrFT of a chirp signal at the optimum order gives an impulse that is relevant to the slope of the chirp signal and the location of the impulse is related to the initial frequency of the chirp signal.

For a special case, $F^0\{r(t)\}$ equals the time domain signal and $F^1\{r(t)\}$ gives the frequency domain signal. Accordingly, the inversion formula of FrFT is as follows

$$r(t) = \frac{1}{\sqrt{2\pi}} \int_{-\infty}^{\infty} R_a(u)\, K_{-a}(t,u) du \tag{6-32}$$

The FrFT operates as the orthonormal representation of the chirp signal. The general linear chirp expressed as $e^{j(bt^2+ct+d)}$ is the chirp rate $b$ matched to the transform order. The matching process is represented in Figure 6-9 using the derivative of signal's phase function, namely its instantaneous frequency $f_y$. Referring to Figure 6-9, considering a chirp signal with slope $2b$, optimal rotation angle $\alpha$, the optimal order parameter $a_{opt}$ is represented as $\frac{2}{\pi}\alpha$. The position of FrFT impulse $\beta$ and the initial frequency of the chirp signal $c$ can be represented as $\beta = csin\alpha$. In case the projection axis $u_a$ matches with the chirp rate of the signal, then FrFT yields its maximum response.

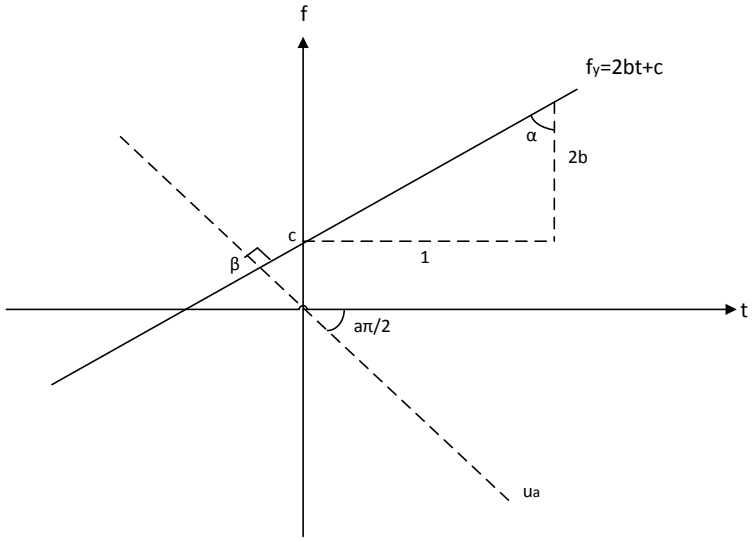


Figure 6-9: Geometric representation of FrFT [95]

At present, there is no formal definition of discrete FrFT, therefore only discrete approximations are used. In the literature, various fast versions of the discrete FrFT approximations were developed. The most commonly used version described in [94] was analyzed in [96] and accordingly discrete FrFT provides close results to the continuous FrFT. However, due to the use of discrete approximation, even in the case of without excision the inversion of FrFT does not completely recover the original signal [97], this gives additional loss on the acquisition sensitivity but this loss could be assumed as negligible. Using the method in [94], the computational complexity of FrFT is almost same as the conventional Fourier O(NlogN) coming with no additional cost for a fixed order $a$. Due to the windowing operation in Short Time FrFT (STFrFT), the complexity increases to $O(N^2 logN)$. The complexity increases further with the search of an optimal order. The order search algorithm is performed by FrFT over a range of different orders between $a = 0$ and $a = 2$.

The discrete approximation of FrFT implementation provided by Ozaktas contains one chirp pre-multiplication, one chirp convolution, one chirp post-multiplication and normalization operations. The implementation steps are as follows:

***Input*:** $r_\mu$ digitized IF signal
***Output:*** Interference mitigated IF signal
*1: Read* M *samples of the input signal*
*2: Multiply the input signal by the linear chirp whose chirp rate is stated by the transform order*
*3: Perform chirp convolution using a scaled FFT and the scaling parameter is related to the transform order*
*4: Apply a second chirp multiplication*
*5: The last step of FrFT comprises normalization by a scaling factor that also depends on the transform order*
*6: Set the detection threshold in terms of maximum value of FrFT bins of interference free segment of the input signal*
*7: Set the FrFT bins that are above the predefined threshold to zero*
*8: Perform inverse FrFT by applying the same process of FrFT with a negative transform order*

Algorithm 6-6: FrFT based mitigation algorithm following Ozaktas implementation [94]

**Short Time Fractional Fourier Transform**

The spectrogram of STFrFT implies improved resolution of chirp signals compared to conventional STFT. The principle of STFrFT based excision algorithm is illustrated in Figure 6-10. In the first step, the chirp jammer is multiplied with the window. After windowing

operation, it follows chirp multiplication, chirp convolution and a second chirp multiplication in the FrFT process which yields:

$$STFr^{a}\{r(t)\}(t,u) = \int_{-\infty}^{\infty} r(\tau)h(\tau - t)K_{a}(\tau,u)d\tau \quad (6\text{-}33)$$

Its orientation $\hat{\alpha}$ produces the most concentrated peak which is estimated by FrFT. Next, STFrFT is applied with the estimated $\hat{\alpha}$. Then, excision is applied by comparing the magnitude of FrFT coefficients to the threshold value and the ones above the threshold are excised. The threshold is set with respect to the maximum value of FrFT coefficients of the interference free section of the stream.

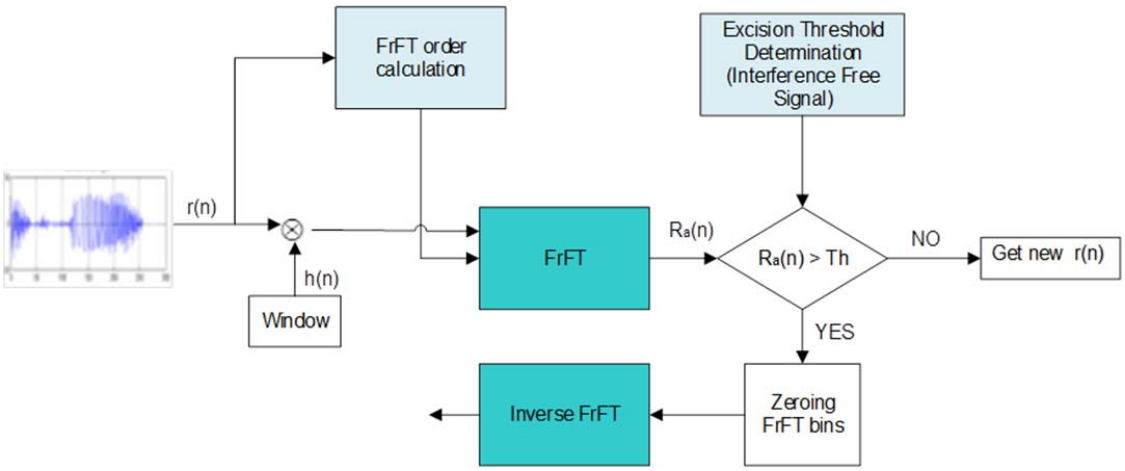


Figure 6-10: STFrFT flow diagram assuming a known optimal order

In the last step, inverse STFrFT is applied to the excised samples by rotating $R_{a}(u)$ through an angle of α with an order parameter of $-a$ which yields:

$$r(t) = \int_{-\infty}^{\infty} STFr^{a}\{r(t)\}(t,u)h(\tau - t)K_{-a}(\tau,u)d\tau \quad (6\text{-}34)$$

**Selecting the FrFT order and the threshold**

The FrFT of a chirp with a matching sweeping rate is localized as an impulse and gives its maximum peak. The order parameter has to be chosen properly for the chirp signal that tunes the transform to give an optimal response. The optimum FrFT order is decided via a search algorithm by evaluating the fractional Fourier transform of the signal over a range of different orders

between $a = 0$ and $a = 2$. The position of the peak is related to the chirp start frequency, bandwidth and chirp start position. The optimum order can be derived by using the geometrical representation in Figure 6-9 as follows:

$$a_{opt} = \frac{2}{\pi}\alpha = -\frac{2}{\pi} arctan\left(\frac{1}{2b}\right) \tag{6-35}$$

With FFT length $N$ and sampling frequency $f_s$, the optimum order for a chirp signal can be rewritten using the geometry of Figure 6-9 as [95]

$$a_{opt} = -\frac{2}{\pi} arctan\left(\frac{{f_s}^2/N}{2b}\right) \tag{6-36}$$

Eqn. (6-36) is used to calculate the optimal order for a sampled linear chirp signal with a known chirp rate $b$. The threshold is calculated using the maximum value of FrFT bins of interference-free segment of the signal.

## 6.5 Performance Results

Interference signals induce false detection in acquisition or loss of lock on tracking correlator loops. These effects are tried to be suppressed by aforementioned methods studied in section 6.4. A summary of interference signal generation scenarios and corresponding suppression methods are tabulated in Table 6.7. Hereby, algorithms are analyzed using various interference signals. Their performance is measured by 3-D acquisition and tracking sensitivity plots using $C/N_0$ metric. According to scenario $S_{I1}$, a measurement campaign was performed at Munich Airport-Franz Josef Strauss to record pulse interference signals. There were two DME stations in the vicinity of the airport and signals were recorded in the measurement bus at the time of aircraft is landing as represented in Figure 6-11. For measurement campaigns, a NovAtel GPS-704-x Passive Antenna, 16 dB Low Noise Amplifier (LNA), the IpexSR and the triple-frequency USB front-end developed by the Fraunhofer Institute are used as shown in Figure 6-12. E5a signals were recorded with ADC resolution of 4 bits. Only E5a signal is considered since E5a is more impacted from pulse interference than E5b; even E5b signal carries integrity information.

Figure 6-11: Measurement campaign at Munich-Airport

Table 6.7: Summary of interference scenario definitions

| Scenarios | Signal recording details | GNSS Signals | Methods used |
|---|---|---|---|
| $S_{I1}$ | **Pulsed interference**: Generated via a measurement campaign performed at Munich Airport. The DME signals were recorded using ipexSR at the time of plane was landing. | GIOVE E5a | Pulse clipping, blanking, DWT, Time-FCME, STFT-FCME |
| $S_{I2}$ | **CWI interference**: The superposition of CWI and GIOVE E5a signal is generated in a Matlab environment and then upconverted using hardware setup. | GIOVE E5a | Notch filtering, STFT-FCME |
| $S_{I3}$ | **Chirp interference**: Generated via commercial in-car jammers with different attenuators combined to the navigation signal (generated from NavX-NCS simulator). The data has been recorded using a USB front-end with a sample rate of 20 MHz and 8 bit. During recording, the jammer is activated after 70 s. | L1,E1 | FrFT, STFT |

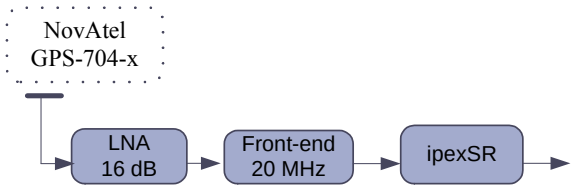


Figure 6-12: Measurement setup

The performance of mitigation algorithms are analyzed using estimated Rx signal power levels in acquisition and tracking process based on multi-correlator techniques. Settings are tabulated in Table 6.8. In STFT, overlapping (50%) segments with FFT size of N=64 and N=2048 are used for DME and CWI respectively to reduce the windowing loss to around 1 dB and Heapsort is used to rearrange FFT samples in an ascending order. The initial clean set sizes are L=8 and L=256 samples. The initial threshold was calculated with the FCME algorithm with the target probability of false alarm of $\mathrm{P_{fa}} = 1\mathrm{E} - 05$. The higher the $P_{fa}$ is, the more interference plus desired signal plus noise is suppressed. This also increases the computational load in the receiver. Due to this reason, a low $P_{fa}$ has been selected. The 3-D acquisition plot in Figure 6-13 shows the magnitude of normalized correlation function output as a function of code phase and carrier Doppler frequency. This indicates that cross-correlation peaks after mitigation via zeroing bury the signal peak into the noise which prevents acquisition. Figure 6-14 shows the tracking sensitivity of DME interfered real GIOVE E5a signal. Against pulse interference, it is shown that all algorithms present similar interference suppression gain with respect to without mitigation case. The achieved gain is between around 0.2 and 0.35 dB. However, the gain provided via STFT method is slightly higher compared to other methods.

Table 6.8: Tracking process settings

| Loop bandwidths (DLL/FLL/PLL) | Coherent integ. time | Sampling rate | Front-end bandwidth |
|---|---|---|---|
| 0.5/10/20 Hz | 20 ms | 40.96 MHz | 20 MHz |

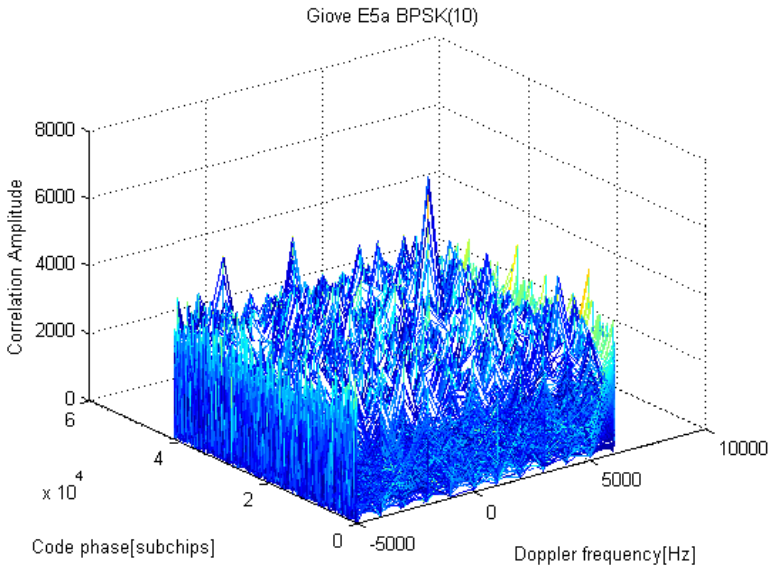


Figure 6-13: Acquisition correlation amplitude via pulse blanking applied under DME using single coherent integration time of $T_{coh}$:1 ms, with estimated $C/N_0$ of 44.6 dBHz

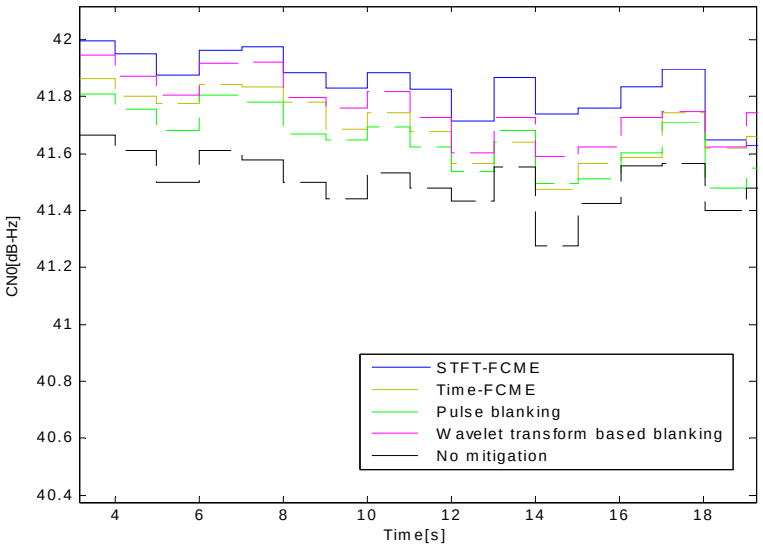


Figure 6-14: Tracking sensitivity comparison of mitigation methods for detecting DME interfered GIOVE E5a signal

In $S_{I2}$ scenario, the CWI signal is recorded in a laboratory environment with a setup depicted in Figure 6-15. The signal recording setup was based on the module used in [98]. The superposition of CWI and GIOVE E5a signal is generated in Matlab environment in the baseband. E5a BPSK(10) is generated with a sampling rate of 40.96 MHz. The Rx signal power is calibrated at 158 dBW. The interfered baseband signal is generated, stored and replayed from the signal recorder in the analog domain. Afterwards it is mixed with the local oscillator for up-converting it to the RF frequency of 1176.45 MHz and then the signal power is attenuated using a 31 dB attenuator and finally the signal is fed into the ipexSR front-end.

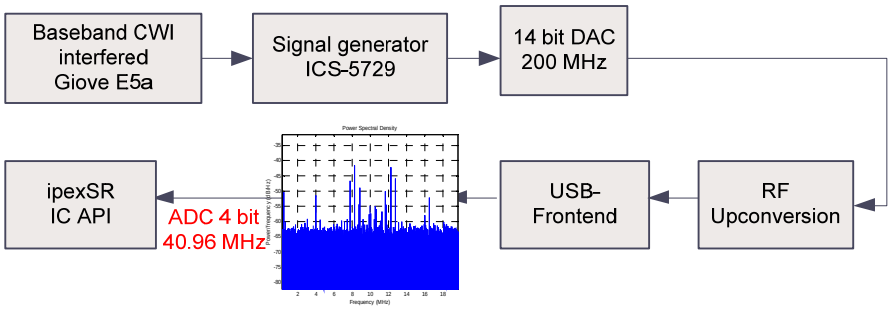


Figure 6-15: Generated CWI signal recording set up

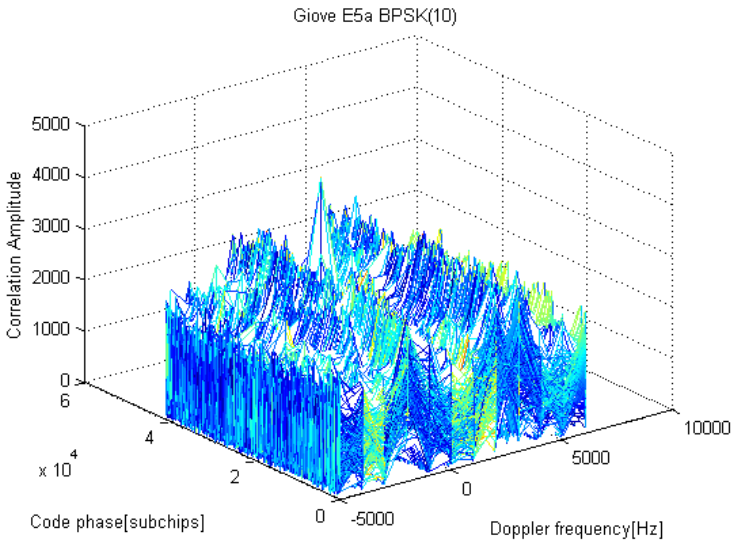


Figure 6-16: Acquisition correlation amplitude without any suppression methods applied under CWI with estimated $C/N_0$ of 40.7 dBHz

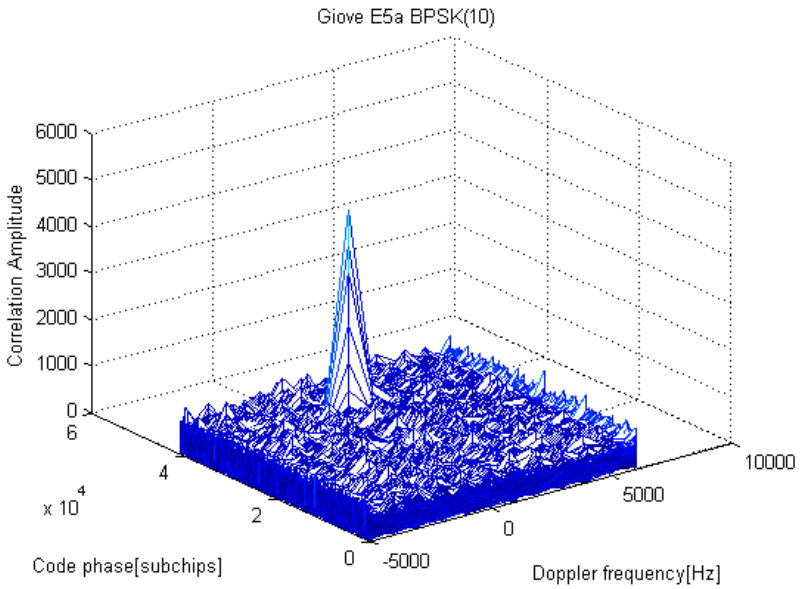


Figure 6-17: Acquisition correlation amplitude via STFT-FCME applied under CWI using single coherent integration time of $T_{coh}$: 1 ms with estimated $C/N_0$ of 49.6 dBHz, $T_{CME}$ =4.96

In Figure 6-16 and Figure 6-17, an exemplary 3-D acquisition plots are shown for CWI with/without mitigation. Using single dwell time, the achieved acquisition sensitivity gain using STFT-FCME is around 9 dB compared to no mitigation case. For tracking sensitivity comparisons, STFT-FCME is compared with conventional notch filter. Notch filter passes all frequencies except the stopband centered at the filter center frequency. In this method, IF sample spectral peaks are estimated using PSD. Considering the estimated interference power, notch filter parameters are determined and the filter is applied. The performed measurements indicated that the gain achieved with STFT-FCME compared to notch filtering is roughly 4 dB as shown in Figure 6-18. This gain could be partly due to the iterative calculation of threshold. The real-time aspect of interference mitigation modules is indicated in Table 6.9. On a PC with Intel Core 2 Quad CPU 2.66 GHz processor with four cores, the normalized computational time for a notch filter processing of one data packet corresponds to 1.0078 s. From normalized time results, as expected Wavelet transform based excision is the most computationally complex method in terms of processing time. With STFT-FCME, less complexity is achieved; however it is already high

for a real- time process. Due to high gain achieved via STFT-FCME, the time spent can be diminished by applying some implementation optimizations.

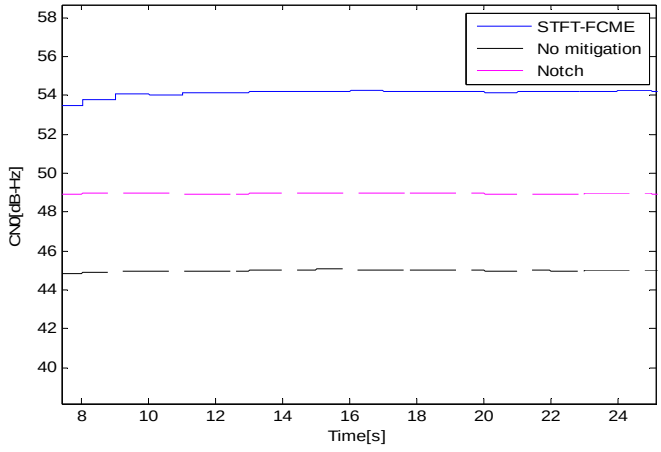


Figure 6-18: Tracking sensitivity comparison of mitigation methods for detecting CW interfered GIOVE E5a signal

Table 6.9: Comparison of mitigation methods considering normalized processing time

| Algorithm | Normalized time |
|---|---|
| Notch filtering | 1 |
| Pulse blanking | 2.18 |
| Wavelet trans. based blanking | 32.72 |
| Time-FCME | 4.911 |
| STFT-FCME | 15.511 |

According to scenario $S_{I3}$, the chirp interfered GPS L1 signal has been recorded. The source of chirp interference is the commonly used commercial in-car jammers employed in [65]. The most commonly used commercial in-car jammer has one positive saw-tooth function for describing the instantaneous frequency. It is a linear chirp signal and has a pulse-like structure as shown in Figure 6-19. In the thesis, this type of jammer is used. The bandwidth of the jammer is 11.82 MHz, the sweep time is 11.71 μs and the center frequency is 1575.07 MHz.

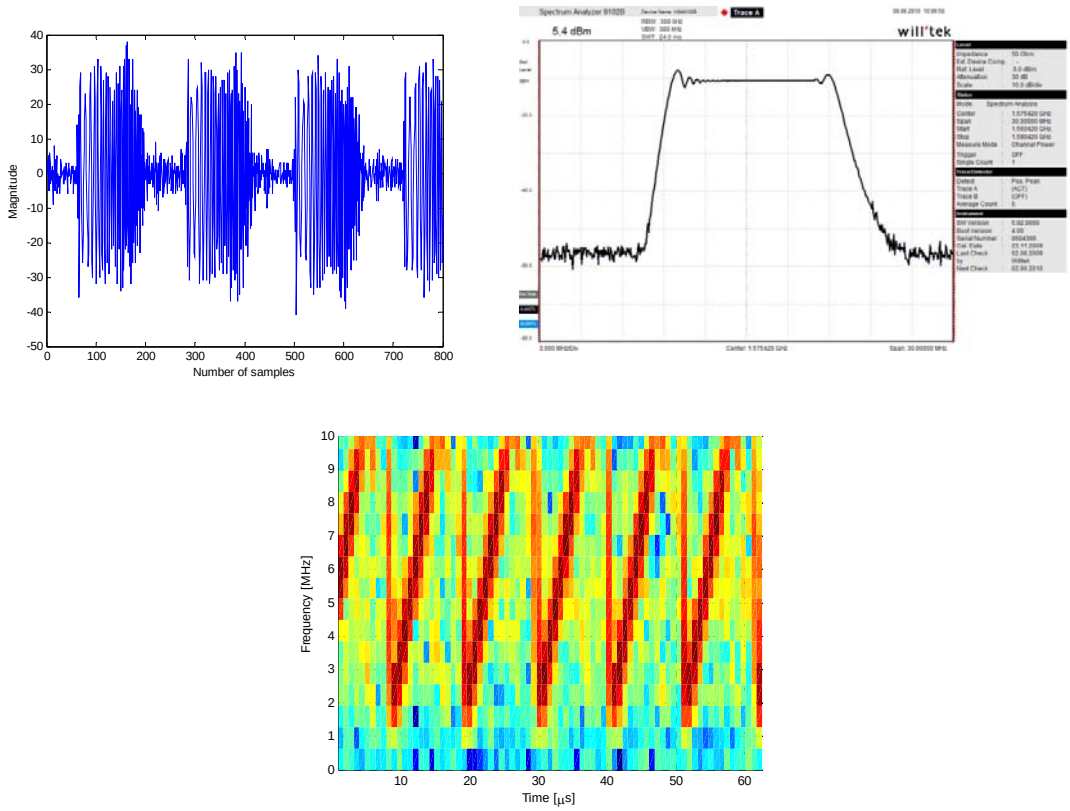


Figure 6-19: Time domain, PSD and spectrogram of the chirp jammer signal on L1 band [99]

In Figure 6-20, fractional transform of the chirp interfered signal with different orders is shown. In this example, FrFT length of 256 is selected that constitutes the whole chirp signal. The FrFT order depends on the FFT window length. Therefore, an appropriate FFT size can be 256 considering the sweep time of 11.71 μs and the sampling rate of 20 MHz. Using a=0.58, the most concentrated chirp signal is achieved, however in that case the FrFT of the chirp signal is not a perfect impulse. This can be interpreted that the energy of the chirp signal is not localized in a few bins, but it is spread through FrFT bins between 120 and 220. This spread introduces some degradation on the desired signal and gives loss on the receiver sensitivity. In that case, it is critical to choose the threshold value such that if Th1 is selected, then interference signal has a large impact on the excised signal and if Th2 is selected then the desired signal is also cut off. In both cases the sensitivity of the receiver is degraded. The method is to tune the transform in a way to concentrate the energy of the signal on its side peaks as possible in the TF representation. For this purpose, the FrFT length of 32 is utilized where the threshold can be set without degrading the desired signal with an order of 0.94. The left plot of Figure 6-21 shows that the

threshold is calculated by using the maximum value of FrFT bins of interference-free segment of the signal which is 7 in this example. In the right plot, the magnitude of FrFT bins of the signal with interference is shown using the optimum order of 0.94.

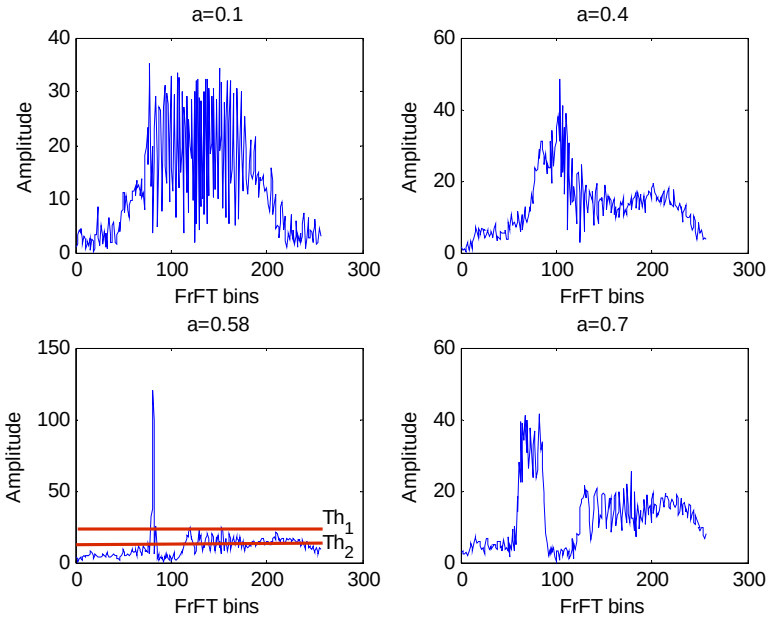


Figure 6-20 FrFT order selection with FrFT length 256

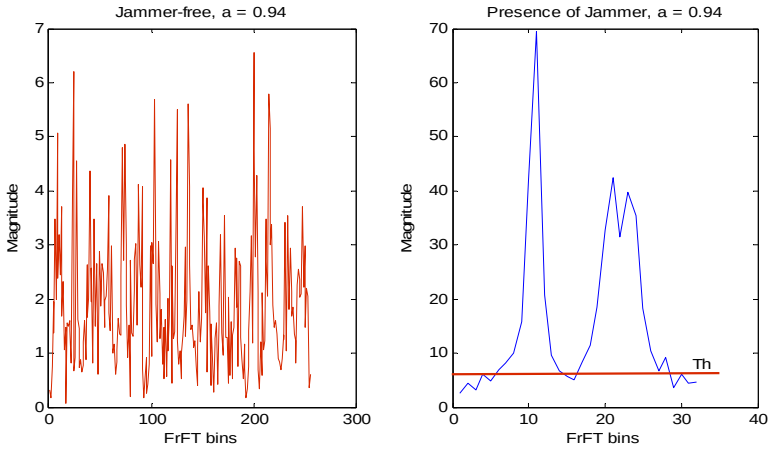


Figure 6-21 FrFT of interference-free (left), interference signal (right) using window length of 32 and order of 0.94

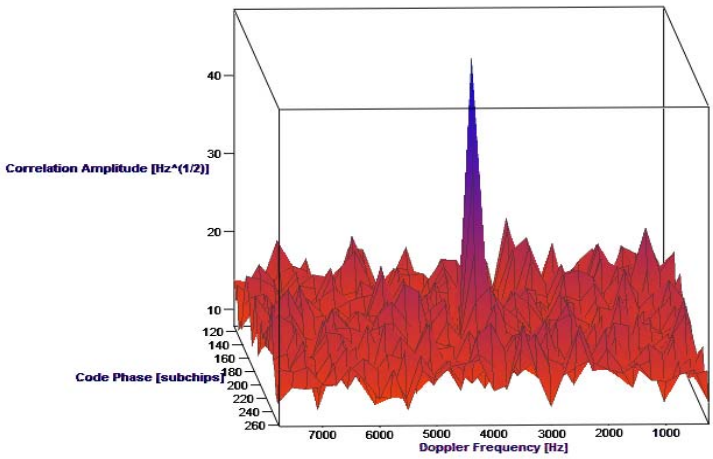


Figure 6-22 Acquisition plot in case no mitigation algorithm is applied achieving 33.7 dBHz in the presence of chirp interference

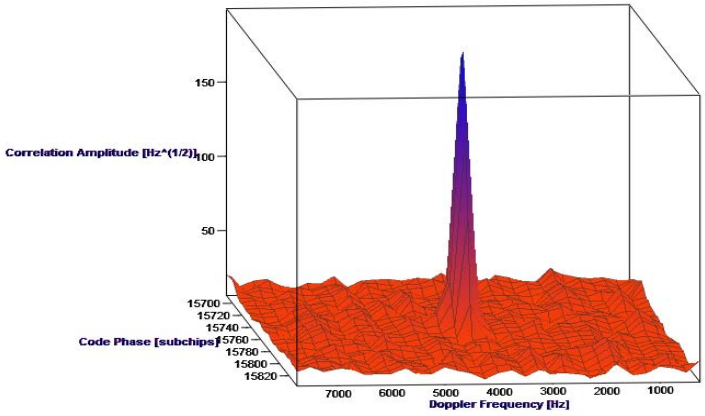


Figure 6-23: Acquisition plot in the case of STFrFT mitigation algorithm is applied achieving $C/N_0$ of 46 dBHz in the presence of chirp interference

In Figure 6-22 - Figure 6-23, exemplary 3-D acquisition plots are represented. Hereby, the achieved acquisition sensitivity gain using STFrFT is around 13.7 dB compared to no mitigation case in the presence of chirp interference. The tracking sensitivity of chirp interfered L1 band signal that has JNR value of 34 dB is shown in Figure 6-24.

Performance of mitigation algorithms are analyzed using estimated Rx signal power levels in tracking process based on multi-correlator technique. Compared to STFT, the gain provided via STFrFT method is 1.1 dB. The FrFT spectrum of a chirp signal is more concentrated than its FFT spectrum; so this makes FrFT a more capable method against chirp jammer signal analysis. During generation of the IF signal, the jammer is activated after 70 s. Thus, the receiver without interference suppression module is completely jammed after the jammer is activated and causes loss-of-lock in tracking loops. On the other hand, by using STFrFT and STFT, achieved estimated $C/N_0$ is 46.1 dBHz and 45 dBHz respectively.

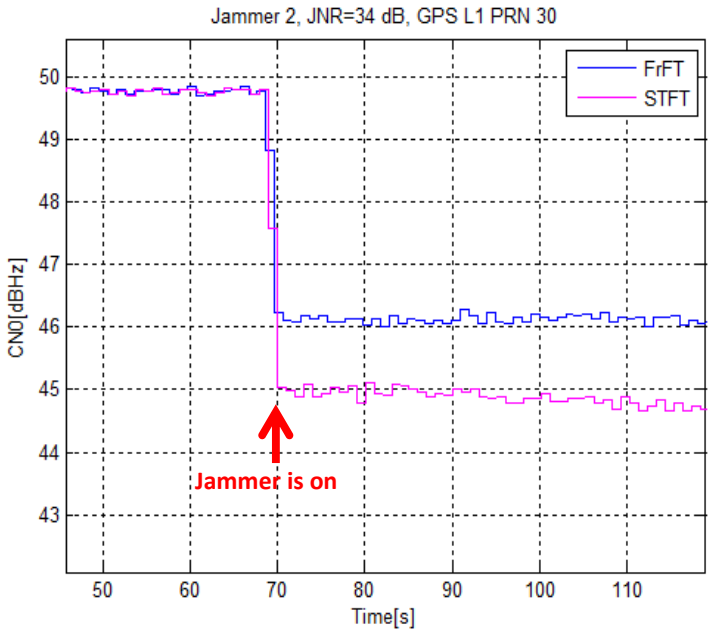


Figure 6-24: Tracking sensitivity of GPS L1 signal using STFT and STFrFT methods

## 6.6 Conclusion

In this chapter, the most promising interference suppression methods are analyzed. Besides conventional blanking, clipping, notch filtering; advanced methods of STFT, Wavelet transform and FrFT are used. According to the results, against pulse interference, STFT-FCME outperformed wavelet transform and against CW interference, conventional notch filtering is outperformed. The gain achieved from STFT-FCME detector compared to conventional notch

filtering is roughly 4 dB. The improvement on the gain could be due to the iterative calculation of the threshold in FCME, hence useless suppression of desired signal has been prevented. On the other hand, notch filtering and pulse blanking are the most computationally attractive methods nevertheless they require knowledge of the noise level. It is also noteworthy that wavelet transformation based excision method gives high computational load to the software receiver and it is almost not possible to use it in a real-time process. Hence, STFT-FCME method could be used as a common suppression module against both pulse and CW interference signals.

For chirp interference signal localization, fractional Fourier transform is an attractive method. Even though the complexity of fractional Fourier transform and FFT is almost the same, the optimum order calculation of fractional Fourier transform increases the computational cost. Searching the optimum order using estimation techniques will be a continuation of this work.

A commercial chirp jammer signal with JNR of 34 dB is used to test aforementioned methods. In case no excision method is applied, the receiver is completely jammed; hence acquisition and tracking are not achieved. The STFrFT method gives better detection capability within 1 dBHz compared to STFT. That is to say that it is better suited to localize the jammer in the transform domain and thus has to excise less bins compared to the STFT. Accordingly, it causes less degradation to the original GNSS signal power. As a result, it provides the best overall performance to excise the single component chirp signal. Against multi component chirp signal, the performance of fractional Fourier transform will be investigated in a future work.

Ultimately, what is remarkable from GNSS point of view is the realization of fractional Fourier transform for detection and mitigation of chirp interference considering computational load. Hence generalization of interference operations in the receiver cannot be reduced to FFT only, rather fractional Fourier transform offers attractive results against chirp interference.

# REFERENCES

# REFERENCES


[1] C. Van Nee, "New Fast GPS Code-Acquisition Technique Using FFT," in *IEEE Elecronics Letters vol. 27 No. 2 Internet References*, 1991.

[2] D. Lin and J. Tsui, "Comparison of acquisition methods for software GPS receiver," in *ION GPS 2000*, Salt Lake City, UT, September 19.

[3] D. Akopian, "A Fast Satellite Acquisition Method," in *ION GPS 2001, 11-14 September 2001*, Salt Lake City, UT, 2001.

[4] W. Hurd, J. Statman and V. Vilnrotter, "High Dynamic GPS Receiver Using Maximum Likelihood Estimation and Frequency Tracking," in *IEEE Transactions on Aerospace and Electronic Systems, AES-23(4)*, 1987.

[5] C. Chung., "Differentially coherent detection technique for direct-sequence code acquisition in a Rayleigh fading mobile channel," in *IEEE Transactions on Communications, vol. 43, no. 2/3/4*, 1995.

[6] A. Schmid and A. Neubauer, "Comparison of sensitivity limits for GPS and Galileo receivers in multipath scenarios," in *IEEE Position Location and Navigation*, 2004.

[7] Dettmar and H. Elders-Boll, "Efficient differentially coherent code/Doppler acquisition of weak GPS signals," in *Proceedings of the International Symposium on Spread Spectrum Techniques and Applications (ISSSTA)*, Sydney, Australia.

[8] A. Sicramaz, "Analysis of Differential Acquisition Methods by Using Monte-Carlo

Simulations," in *ION GNSS*, Long Beach, CA, 2005.

[9] M. Psiaki, „Block Acquisition of Weak GPS Signals in a Software Receiver," in *ION GPS 2001*, Salt Lake City, UT, 11-14 September 2001.

[10] E. Glennon und A. Dempster, „A Novel GPS Cross Correlation Mitigation Technique," in *ION GNSS 18th Internation Technical Meeting of the Satellite Division*, Long Beach, CA, 13-16 September 2005.

[11] P. Madhani, P. Axelrad und K. Krumvieda, „Application of Successive Interference Cancellation to GPS Pseudolite Near-Far Problem," in *IEEE Transactions on Aerospace and Electronic Systems, vol. 39, No. 2*, April 2003.

[12] P. Sagiraju, D. Akopian and H. Valio, "Fine Frequency Estimation in Weak Signals for GPS Receivers," in *ION NTM 2006*, Monterey,CA, 2006.

[13] D. Akopian, H. Valio and S. Turunen, "Fine Frequency Resolving Acquisition Methods for GPS Receivers," in *ION GPS*, Portland, 2002.

[14] L. Gottesman and L. Milstein, „On the Use of Interference Suppression to Enhance Acquisition Performance in a CDMA Overlay Scenario," in *IEEE*, 1995.

[15] E. Siess and C. Weber, "Acquisition of direct sequence signals with modulation and jamming," in *IEEE Journal on Selected Areas in Communications, vol. 4, no. 2*, 1986.

[16] J. Jang, M. Paonni and B. Eissfeller, "CW Interference Effects on Tracking Performance of GNSS Receivers," in *IEEE Transactions on Aerospace and Electronic Systems vol. 48, No. 1* , 2012.

[17] J. Iinatti, „On the threshold setting principles in code acquisition of DS-SS signals,“ in *IEEE J. Select. Areas Commun., vol. 18, no. 1*, Jan. 2000.

[18] L. Gottesman and L. Milstein, "The coarse acquisition performance of a CDMA overlay system," in *IEEE Journal on Selected Areas in Communications, vol.: 14 , Issue: 8*, 1996.

[19] J. A. Volpe, "Vulnerability Assessment of the Transportation Infrastructure relying on the Global Positioning System," John A. Volpe National Transportation Systems Center, 2001.

[20] S. Deshpande, „Study of Interference Effects on GPS Signal Acquisition,“ in *MSc Thesis, UCGE Report No. 20199, Department of Geomatics Engineering, University of Calgary*, 2004.

[21] D. Borio, "A Statistical Theory for GNSS Signal Acquisition," in *PhD Thesis*, 2008.

[22] J. Grabowski and C. Hegarty, "Characterization of L5 Receiver Performance Using Digital Pulse blanking," in *Proceedings of The Institute of Navigation GPS Meeting*, Portland, OR, 2002.

[23] F. Bastide, C. Macabiau and D. Akos, „Automatic Gain Control as an Interference Assessment Tool,“ in *ION GNSS*, 2003.

[24] E. Anyaegbu, J. Cooper and S. Boussakta, "Wavelet based Interference Detection and Suppression Algorithm for Next Generation GNSS Signals," in *The European Navigation Conference (GNSS)*, Munich, 2005.

[25] D. Borio, "GNSS Acquisition in the Presence of Continuous Wave Interference," in *IEEE Transactions on Aerospace and Electronic Systems vol. 46, No. 1*, January 2010.

[26] A. Sicramaz Ayaz, R. Bauernfeind, J. Jang, T. Pany and B. Eissfeller, "Real-time GIOVE Signal Performance using STFT based excision method in the presence of Interference," in *ION GNSS*, Portland, OR, 2011.

[27] S. Turunen, „Weak Signal Acquisition in Satellite Positioning," PhD Thesis, 2010.

[28] "BeiDou Navigation Satellite System Signal In Space Interface Control Document Open Service Signal B1I (Version 1.0)," China Satellite Navigation Office, December 2012.

[29] „Galileo Open Service Signal In Space Interface Control Document," in *GAL OS SIS ICD/D.0*, 23 May 2006.

[30] L. Ries, F. Legrand, L. Lestarquit, W. Vigneau and J. Issler, "Tracking and Multipath Performance Assessments of BOC Signals Using a Bit-Level Signal Processing Simulator," in *ION-GNSS 2003*, Portland, Oregon.

[31] „Interface Specification Navstar GPS Space Segment /User Segment L5 Interfaces," 24 October 2003.

[32] A. Steingass and A. Lehner, "Measuring the Navigation Multipath Channel– A Statistical Analysis," in *ION GNSS Technical Meeting*, 2004.

[33] H. Hashemi, "The Indoor Radio Propagation Channel," in *IEEE vol.81 no.7*, 1993.

[34] H. Al-Bitar, "Advanced GPS Signal Processing Techniques for LBS Services," in *PhD Thesis*, 2007.

[35] M. Irsigler and B. Eissfeller, "Comparison of Multipath Mitigation Techniques with Consideration of Future Signal Structures," in *Proceedings of the International Technical*

*Meeting of the Institute of Navigation, ION-GPS 2003*, Portland, 2003.

[36] W. Suwansantisuk and M. Win, "Multipath Aided Rapid Acquisition: Optimal Search Strategies," in *IEEE Transactions on Information Theory, Vol. 53, No. 1*, January 2007.

[37] C. Stoeber, M. Anghileri, A. Sicramaz Ayaz, D. Dötterböck, I. Krämer, V. Kropp, D. Sanromà Güixens, J. H. Won and B. Eissfeller, "ipexSR: A Real-Time Multi-Frequency Software GNSS Receiver," in *IEEE Elmar*, 2010.

[38] V. Dehghanian, M. Zaheri, J. Nielsen and G. Lachapelle, "Dual-polarized Synthetic Array for Indoor GNSS Handheld Applications," in *The Seventh IEEE International Symposium on Wireless Communication Systems*, York, England, 2010.

[39] T. Pany, Navigation Signal Processing for GNSS Software Receivers, Artech House, 2010.

[40] A. Sicramaz Ayaz, T. Pany and B. Eissfeller, "Performance of Assisted Acquisition of the L2CL Code in a Multi-Frequency Software Receiver," Fort Worth, Texas, 2007.

[41] S. Turunen, „Acquisition Sensitivity Limits of new civil GNSS signals," in *Coordinates, Vol.3, No.1*, 2007.

[42] C. O'Driscoll, „Performance Analysis of the Parallel Acquisition of Weak GPS Signals," PhD Thesis, 2007.

[43] T. Pany and B. Eissfeller, "Code and Phase Tracking of generic PRN Signals with Sub-Nyquist Sample Rates," in *Journal of the Institute of Navigation, Vol. 51, No.2*, 2004.

[44] J. Syrjäarinne and L. Wirola, "Setting a New Standard: Assisting GNSS Receivers That Use Wireless Networks," in *Inside GNSS*, 2006.

[45] P. Misra and P. Enge, Global Positioning System: Signals, Measurements and Performance, 2006.

[46] E. Kaplan and C. Hegarty, Understanding GPS: Principles and applications, Artech House, 2006.

[47] D. Borio and L. Presti, "Data and Pilot Combining for Composite GNSS Signal Acquisition," in *Hindawi publishing corporation, International Journal of Navigation and Observation*, 2008.

[48] D. Borio, C. O'Driscoll and G. Lachapelle, "Composite GNSS Signal Acquisition over Multiple Code Periods," in *IEEE Transactions on Aerospace and Electronic Systems, Vol. 46, Issue 1*, 2010.

[49] T. Bayes, "An essay towards solving a problem in the doctrine of chances," in *Philosophical Transactions of the Royal Society of London 53: 370-418*, 1764.

[50] P. Neyman, "On the problem of the most efficient tests of statistical hypothesis," in *Philosophical Transactions of the Royal Society of London Series A.231: 289-337*, 1933.

[51] S. Kay, Fundamentals of Statistical Signal Processing-Detection-the theory, Prentice Hall, 1993.

[52] B. Zheng and G. Lachapelle, "GPS Software Receiver Enhancements for Indoor Use," in *Proceedings of the 18th International Technical Meeting of the Satellite Division of The Institute of Navigation* , Long Beach, CA, 2005.

[53] S. Shanmugam, J. Nielsen and G. Lachapelle, "Enhanced Differential Detection Scheme for

Weak GPS Signal Acquisition," in *ION GNSS*, Fort Worth, 2007.

[54] "FCC Enhanced 911 regulations, http://www.fcc.gov/911/enhanced/".

[55] EuropeanCommision, „Survey on Implementation of Emergency Call 112," Brussel, 1999.

[56] B. Peterson, D. Bruckner and S. Heye, "Measuring GPS Signals Indoors," in *ION GPS* , Kansas, 1997.

[57] M. Moeglein and N. Krasner, "An introduction to SnapTrack Server Aided GPS Technology," in *ION GPS*, Nashville, 1998.

[58] F. van Diggelen and C. Abraham, "Indoor GPS Technology," in *CTIA Wireless-Agenda*, Dallas, 2001.

[59] A. Saleh and R. Valenzuela, "A statistical model for indoor multipath propagation," in *IEEE journal on selected areas in communications, Vol. SAC-5, No. 2*, 1987.

[60] E. Lutz, D. Cygan, M. Dippold, F. Dolainsky and W. Papke, "The land mobile satellite communication channel recording, statistics, and channel model," in *IEEE Trans. Vehic. Technol., vol. 40*, 1991.

[61] S. Mangold and M. Lott, "Indoor Radio Channel Modelling – Bridging form Propagation Details to Simulation," in *IEEE international conference on Personal, Indoor and Mobile Communications, vol.2*, 1998.

[62] A. Steingass and A. Lehner, "A Channel Model for Land Mobile Satellite Navigation," in *GNSS*, Munich, 2005.

[63] J. Winkel, "Modeling and Simulating GNSS Signal Structures and Receivers," University

of Federal Armed Forces, Munich, 2000.

[64] „Interference susceptibilities of Systems Operating in the 960-1215 Mhz Band Ap-plication to the Compatibility Analysis of the Future Communication System,“ in *ICAO WRC'07 A.I. 1.6*, Malmö, 2005.

[65] R. Bauernfeind and et.al., "Analysis, Detection and Mitigation of InCar GNSS Jammer Interference in Intelligent Transport Systems," in *DLRK*, 2012.

[66] S. Pullen and G. Gao, "GNSS Jamming in the Name of Privacy," in *Inside GNSS March-April*, 2012.

[67] H. Kuusniemi, "Effects of GNSS Jammers and Potential Mitigation Approaches," in *United Nations/Latvia Workshop on the Applications of GNSS*, Latvia, 2012.

[68] T. Humphreys, "Assessing the Spoofing Threat," in *GPS World Vol. 20, No.1*, 2009.

[69] L. Scott, "Location Assurance," in *GPS World, vol. 18, no.7*, July 2007.

[70] G. Xingxin Gao, "DME/TACAN Interference and its Mitigation in L5/E5 Bands," in *ION GNSS*, 2007.

[71] "Vulnerability Assessment of the Transportation Infrastructure relying on the Global Positioning System," John A. Volpe National Transportation Systems Center, 2001.

[72] B. Forssell, Radionavigation Systems, Artech House, 2008.

[73] R. Kelly, "System Considerations for the New DME/P International Standard," in *IEEE Trans., Vol., AES-20, No.1.*, 1984.

[74] S. Gezici, "Design and Analysis of Impulse Radio Ultra Wideband Receivers for

Communications and Geolocation," PhD. Thesis, Princetopn University, 2006.

[75] M. Luo, D. Akos, S. Pullen and P. Enge, "Interference to GPS from UWB Transmitters," in *ION GPS*, 2000.

[76] M. Raimondi, C. Macabiau and O. Julien, "Frequency Domain Adaptive Filtering Against Pulsed Interference: Performance Analysis Over Europe," in *ION NTM*, San Diego, CA, 2008.

[77] R. Landry and A. Renard, "Analysis of Potential Interference Sources and Assessment of Present Solutions for GPS/GNSS Receivers," in *4th Saint-Petersburg on INS*, 1997.

[78] I. IIie, D. Fortin, R. Landry and M. Fortin, "Real World Interference Impacts Analysis using High Dynamic Range GNSS RF/IF Signals Record and Playback," Averna The test engineering company, 2009.

[79] I. Casewell, "FCI Technology Investigations: L band Compatibility Criteria and Interference Scenarios Study," Eurocontrol, 2009.

[80] T. Kraus, R. Bauernfeind and B. Eissfeller, "Survey of In-Car Jammers – Analysis and Modeling of the RF signals and IF samples," in *ION GNSS 2011*, Portland, OR, 2011.

[81] D. M. Akos, P.-L. Normark, J.-T. Lee and K. Gromov, "Low power global navigation satellite system (GNSS) signal detection and processing," in *ION GPS*, 2000.

[82] X. G. Gao, "DME/TACAN Interference and its Mitigation in L5/E5 Bands," in *ION GNSS* , Fort Worth, Texas, 2007.

[83] C. W. Kok and T. Nguyen, "Multirate filter banks and transform coding gain," in *IEEE*

*Trans. Signal Processing, vol. 46, no.7, pp. 2041-2044*, 1998.

[84] J. Vartiainen, J. J. Lehtomäki and H. Saarnisaari, "Double Threshold Based Narrowband signal Extraction," in *Proc. IEEE Vehicular Technology*, Stockholm, Sweeden, 2005.

[85] P. Henttu and S. Aromaa, "Consecutive mean excision algorithm," in *Proc. IEEE Int. Symp. Spread Spectrum Techniques and Applications*, Czech Republic, 2002.

[86] I. Daubechies, "Ten Lectures on Wavelets," 1992.

[87] A. Graps, "An introduction to wavelets," in *IEEE Comput. Sci.Eng. 2 (2) (1995) 50-61.*, 1995.

[88] A. Poularikas and et.al., The Transforms and Applications Handbook, CRC Press LLC, 2000.

[89] Q. Hu, "Development of a real-time wavelet library and its application in electric machine control," Technical University of Munich, 2013.

[90] V. Namias, "The fractional order Fourier transform and its applications to quantum mechanics," 1980.

[91] A. McBride and F. Kerr, "On Namias's fractional Fourier transform," 1987.

[92] A. Lohmann, "Image rotation,Wigner rotation and the fractional Fourier transform," 1993.

[93] L. Almeida, "The fractional Fourier transform and time-frequency representations," 1994.

[94] H. Ozaktas, „Digital computation of the Fractional Fourier Transform,“ in *IEEE Signal Processing Transactions, Vol. 44, No 9*, 1996.

[95] C. Capus and K. Brown, "Short-time fractional Fourier methods for the time-frequency

representation of chirp signals," in *JASA 113*, 2003.

[96] M. Kutay, H. Ozaktas, O. Arikan and L. Onural, "Optimal filtering in Fractional Fourier Domains," *IEEE Transactions on Signal Processing,* Vols. vol. 45, No.5, 1997.

[97] O. Akay and G. Boudreaux-Bartels, "Broadband Interference Excision in Spread Spectrum Communication Systems via Fractional Fourier Transform," in *Conf. Rec. 32nd Asilomar Conf. Signals, Systems, and Computers, vol. 1, 1998, pp. 832–837.*, 1998.

[98] M. Ullrich, „Entwicklung und Aufbau von Signalstörern und deren Auswirkung auf GNSS-Empfänger,“ Neubiberg, 2011.

[99] A. Sicramaz Ayaz, R. Bauernfeind, T. Pany and B. Eissfeller, "Time-Frequency based Intentional Interference Suppression Techniques in GNSS Receivers," in *ION GNSS*, Portland, OR, 2012.

[100] K. Ravi and R. Ormondroyd, "Performance of sequential detectors for the acquisition of data modulated spread spectrum pseudo noise signals," in *IEEE International Conference on Communications*, 1991.

[101] A. Pósfay, T. Pany and B. Eissfeller, "First Results of a GNSS Signal Generator Using a PC and a Digital-to-Analog Converter," in *ION GNSS*, Long Beach, CA, 2005.

[102] J. Lehtomaki, "Analysis of Energy Based Signal Detection," PhD Thesis, 2005.

[103] E. Anyaegbua, G. Brodina, J. Coopera, E. Aguadoa and S. Boussaktaa, "An integrated pulsed interference mitigation for GNSS receivers," in *Journal of Navigation, Vol. 61, Issue 02, pp 239-255*, 2008.

[104] L. Xu and Y. Yan, "Wavelet based removal of sinusoidal interference from a signal," in *Measurement Science and Technology Vol. 15 No. 9*, 2004.

[105] R. Tao, Y. Li and Y. Wang, "Short-time Fractional Fourier Transform and its Applications," in *IEEE Transactions on Signal Processing, Vol. 58 No. 5*, 2010.

[106] C. Candan, M. Kutay and H. Ozaktas, "The discrete fractional Fourier Transform," in *IEEE Transactions on Signal Processing vol.48, pp.1329-1337*, 2000.

[107] A. Van Dierendonk, Global Positioning System:Theory and Applications, American Institute of Aeronautics and Astronautics, vol. 1, 1996.

[108] A. Bultheel and H. Sulbaran, "A shattered survey of the Fractional Fourier Transform," 2003.

# Appendix A Software Receiver Capabilities

The ipexSR is a real-time capable GNSS software receiver which runs on a conventional PC. The signal processing modules which are performed in software run on a PC that is connected to the antenna via a USB front-end as represented in Figure A.1.

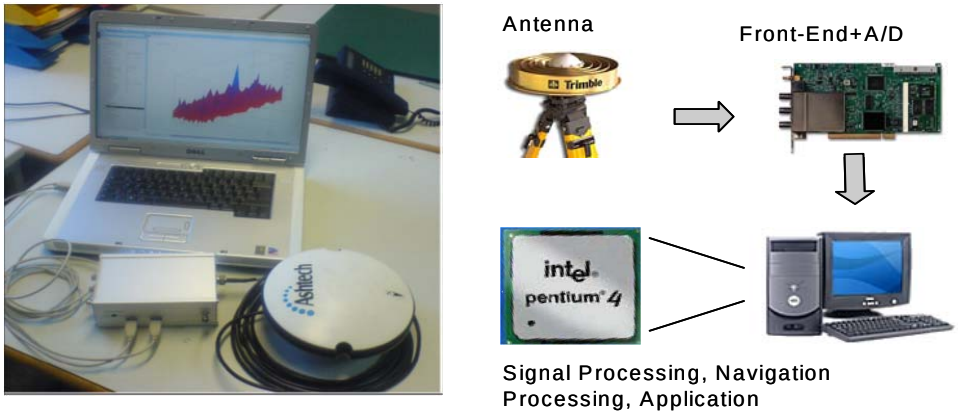


Figure A.1: ipexSR software receiver [37] and user terminal of the ipexSR process flow

The receiver consists of a triple frequency (L1/L2/L5) USB front-end, an FFT-based acquisition model, a tracking scheme with two filter modes, a bit synchronization module, a single shot positioning or Kalman filter based positioning module.

Table A.1: Signals processed in ipexSR

| Systems | Signals |
|---|---|
| GPS | L1 C/A, L2, L5 |
| Galileo | E1, E5, E6 |
| Glonass | L1, L2 |
| EGNOS | L1 |

Besides the real-time capability of ipexSR, it also offers post-processing mode to be able to work with stored IF sample files. The receiver accepts IF samples as an input taken from the hard disc in post-processing mode or from a USB front-end in real-time. The signals processed by the ipexSR are tabulated in Table B.1.

The ipexSR performs all tasks of a conventional hardware receiver. Besides, parameters such as sensitivity, frequency, tracking loop bandwidth are adaptable compared to hardware receivers. One of the most significant characteristics of a receiver is the sensitivity in the sense of the minimum Rx signal strength at which a receiver can still detect the signal. This covers signal acquisition and tracking sensitivities. The bounds to achieve a certain sensitivity level are determined by the front-end and signal processing modules.

In FFT-based acquisition module, there are two levels; the first level indicating to acquire strong signals and the second level to achieve high sensitivity under weak signal coverage. Owing to the second level, standard sensitivity algorithms are improved achieving around 10 dBHz sensitivity. The TTFF achieved with FFT-based acquisition is 0.3 s using 22 point FFT method (P4, 3.4 GHz). Since one FFT is basically sufficient to search one Doppler bin (after the signal pre-processing and the forward transform of the Rx and replica signals), this corresponds to more than 20 million effective correlators.

In the tracking module, the code continuous reference waveform (CCRW) approach is used and the receiver runs in two modes, namely PLL/FLL/DLL and a third order PLL with aided FLL and DLL. Besides, vector re-acquisition technique is used to track signals that show highly variable power characteristics. Vector acquisition computes code phase and Doppler frequency of the corresponding satellite using an approximate PVT solution, independent from the conventional FFT acquisition. The tracking sensitivity of the receiver with data signals is about 35 dBHz and with pilot signals sensitivity further improves to below 10 dBHz. In addition, tracking sensitivities are increased by applying advanced code multipath mitigation techniques implemented using the optimization of the correlator's reference functions. One of the figure of merit appropriate with the ipexSR is the tracking accuracy that is mainly related to tracking errors

of the code and carrier phases. During the evaluation, the external factors of thermal noise, dynamic stress, vibration and clock stability is considered as well. Another related figure of merit is the positioning accuracy in the sense of measuring the positioning errors. With single shot positioning, the achieved PVT accuracy is around 100 m. However with Real-time Kinematic (RTK) method, using code measurements accuracy levels of around 30 cm and using carrier phase measurements 1 mm accuracy levels are realized. Using RTK centimeter level accuracy by using carrier phase measurements could be achieved. In order to improve the positioning accuracy, ipexSR also obtains the EGNOS ephemerides from SISNET service in real-time provided by ESA via internet.

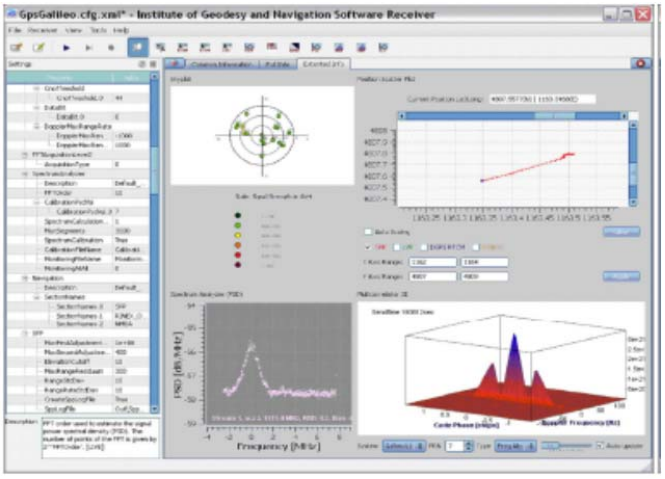


Figure A.2: The general GUI of ipexSR

In the thesis, an Application Programming Interface (API) is used as an interference mitigation module controlling the overall synchronization and positioning modules implemented in ipexSR [3]. Intermediate Frequency (IF) sample API is settled as a stream of packet of samples with certain signal characteristics (e.g. carrier frequency, sample rate) and then applies the *pre-correlation* mitigation algorithm to excise interference signal on the desired GNSS signal band as represented in the following flow diagram .

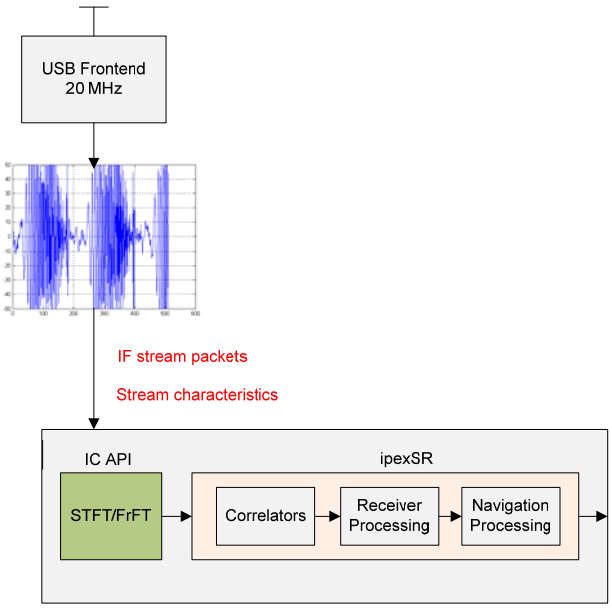


Figure A.3: The concept of ipexSR IF sample API

## Appendix B Parallel Acquisition Using OpenMP

Acquisition is the most computationally intensive module and requires the most processing time in a GNSS receiver and consequently the optimization of this module is essential and any improvement gives considerable performance gain. The acquisition module is in the parallel code phase domain; hence the parallelization on the code phase bin is achieved by circularly shifted FFT process. In this case, for each Doppler frequency bin, correlation is performed for N-point FFT length of samples by multiplying circularly rotated FFT domain preprocessed signal and complex conjugate of FFT domain locally generated code. Besides, parallelization can be extended for a number of Doppler bins and number of visible satellites to be acquired. In parallelized Doppler bin acquisition, correlation function is applied for the whole Doppler frequency bins and the entire code phase bin and hence the processing time is improved depending on computer hardware specifications. Parallelization of the acquisition module is achieved by using OpenMP standard. OpenMP is a high level shared memory parallel programming. It allows applying parallel applications without using threads in a straightforward way by counting the number of iterations and dividing the work among available processors and set them for parallel execution of individual chunks of work. In the implementation, the computationally intensive parts are identified and the dependencies on that part are eliminated. In the presence of nested for-loops, the OpenMP pragmas are used in the outer most loop level which is more beneficial in terms of the amount of work done per iteration. The point to take into consideration through implementation in OpenMP is that not all loops could be parallelized due to dependencies in loops. Another point is to ensure equal division of work (load balancing) among threads. In this way, some threads may not finish the work before other threads and don't waste the performance. By applying OpenMP to the frequency bin, the implementation of the parallel region is written in the algorithm below.

```
// openMP parallel execution of chunks of Doppler bins
#pragma omp parallel \
private(...)
#pragma omp for
// code phase bin is already parallelized by circularly shifted FFT operation
for(#Doppler bins)
{
  for(#FFT length)
  {
    ...
  }
}
```

Algorithm B.1: Parallel Doppler bin Acquisition using OpenMP

The parallelized acquisition module is tested for GPS L1 C/A signal using dual, quad and 8 core computers and considering the serial acquisition, performance gains of acquisition time are 42%, 52%, 64% respectively.

Table B.1: Computer specifications

| | |
|---|---|
| Processor | Intel Pentium ® 3.2 GHz |
| | Intel Core 2 Quad CPU 2.66 GHz |
| | Intel Xeon ® 2.66 GHz |
| # of cores | 2 |
| | 4 |
| | 8 |
| Operating system | Windows 7 Ultimate |
| | Windows XP |
| | Windows XP |
| L2 Cache size | 2 MB |
| | 4 MB |
| | 6 MB |

Table B.2: Acquisition time comparison with various computer specifications (in) and serialized/parallelized acquisition using FFT order of 14.

| | Acquisition time [ms] | | |
|---|---|---|---|
| | Dual Core | Quad Core | 8- Core |
| Serial Doppler Bin (SDB) | 85.54 | 100.91 | 99.91 |
| Parallel Doppler Bin (OpenMP) | 48.94 | 47.99 | 35.09 |
| Serial Doppler Bin (SDB) | 85.54 | 100.91 | 99.91 |

Acquisition time requirement of different number of cored computers is depicted in Figure B.1. Accordingly, in serial Doppler bin acquisition mode, it requires less acquisition time for the same scenario since dual core computer has a faster CPU than others. Quad and 8 core computers have the same CPU speed; therefore they require almost the same amount of acquisition time. In parallel Doppler bin mode, CPU speed and L2 cache size specifies the performance gain, thus for dual and quad core computers they have the same performance. One can clearly see the performance gain when the parallel Doppler bin mode is used and work is split over several cores.

The FFT size of samples determines the code phase resolution; hence increased code phase resolution eases the ambiguity resolution problem. Ascending FFT length at one hand increases the code phase resolution, on the other hand increases the acquisition time as well.

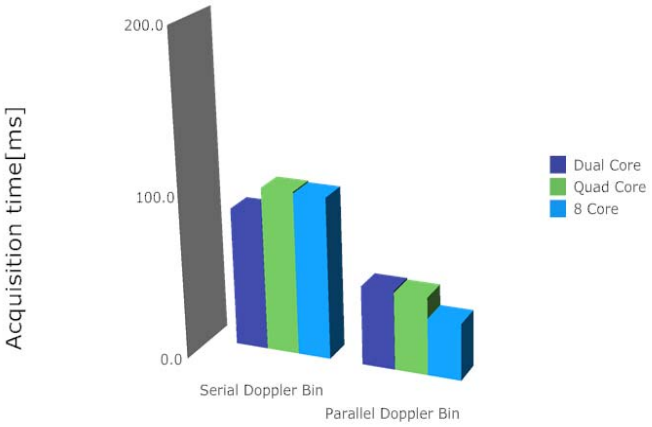


Figure B.1: Acquisition time comparison for various cored computers w.r.t serial/ parallel Doppler bin mode of acquisition process

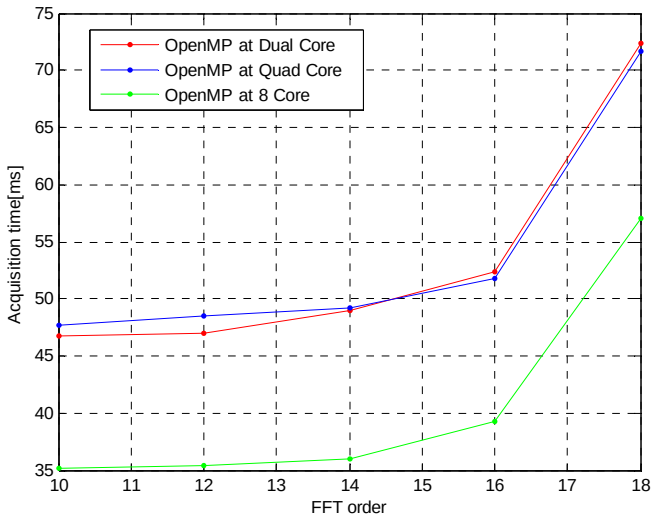


Figure B.2: Acquisition time comparison versus FFT length for various computer hardware specifications

## Appendix C Tracking Sensitivity Evaluation of Simulated DME

The superposition of GIOVE E5a signal and DME interference is generated in baseband using Matlab. E5a BPSK (10) is generated for the following measurements with a sampling rate of 40.96 MHz. The Rx signal power is calibrated at -158 dBW. The interfered baseband signal is generated, stored and replayed from the signal recorder in the analogue domain. Afterwards it is mixed with the local oscillator for up-converting it to the RF frequency of 1176.45 MHz. Then signal power is attenuated using a 31 dB attenuator. At the final stage, the signal is fed into the ipexSR front-end. The photo of the test setup and the schematic overview of the system are presented in Figure C.1.

Figure C.1: Test setup

DME interference is expected to exist in the 1151 – 1213 MHz frequency range when operating in the X mode and thus Galileo E5a/b and GPS L5 signals are directly interfered.

For the following simulations, a typical pulse interval of 12 μs between two single pulses and a repetition rate of about 2700 pulse pairs per second (pps) is used. The following test scenario is considered for DME interference:

Table C.1: Settings used in signal generation and tracking process in ipexSR

| | |
|---|---|
| Process Time (s) | 60 |
| IF (MHz) | 12.74 |
| Sampling Frequency (MHz) | 40.96 |
| ADC bits | 4 |
| Pulse interval between single pulses (μs) | 12 |
| Pulse repetition rate (pps) | 2700 |
| DME frequency offset | 0 |
| Loop bandwidths narrow /wide (Hz) | 0.5/3 (DLL)<br>18/20 (PLL)<br>4/10 (FLL) |
| Coherent integration time (ms) | 20 |
| Interference free $C/N_0$ (dBHz) | 5 |
| Threshold FLL (dBHz) | 40 |

The AGC gain factor of ipexSR front-end is set externally by the user, hence for every interference signal level the AGC is updated by checking the histogram of the signal generated. In the signal generation scenario, DME signals at power levels of -110/-100/-90 dBW are generated. The PSD of simulated signal with DME power level of -110 dBW is represented in Figure C.2. There is one partial band interference spectrum around 15 MHz frequency. Monotone like spikes in the PSD plot are non-intentional signals which exist although when there is no DME. We can ignore them as their power is not severe and not pulse like. The time domain and PSD representations are illustrated in Figure C.3.

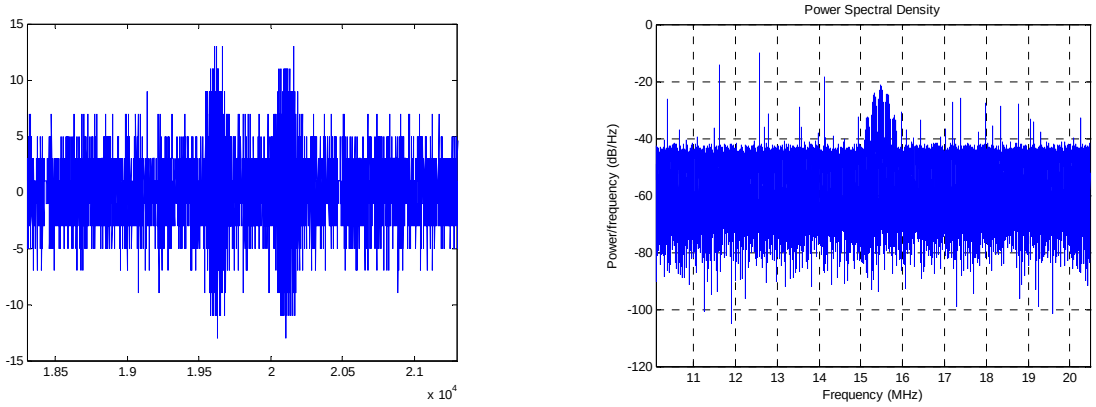


Figure C.2 The GIOVE E5a signal plus DME interference having power level of -110 dBW with 2700 pps

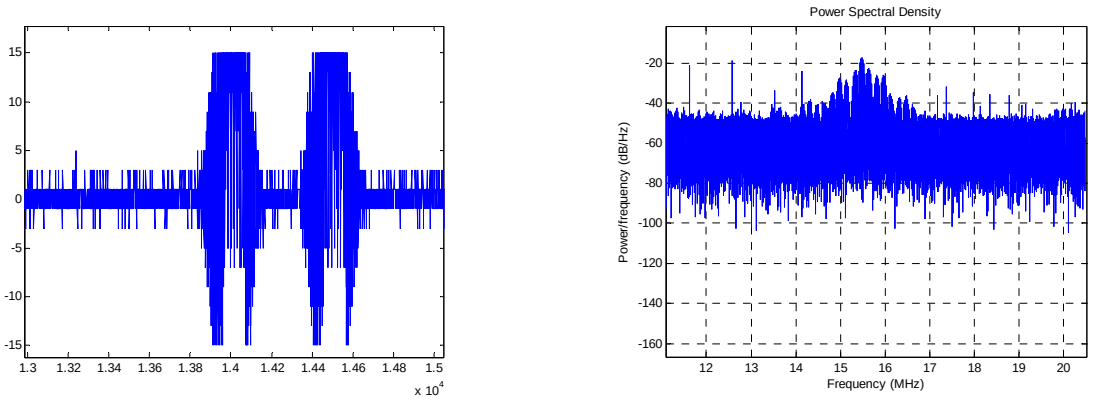


Figure C.3 The GIOVE E5a signal plus DME interference having power level of -90 dBW with 2700 pps

In Figure C.4-Figure C.6 tracking sensitivities are represented for the typical GIOVE E5a data signal at the power level of -158 dBW with strong, medial and weak DME signals. In blanking method, block size of 100 sample is used. In strong DME scenario, wavelet based mitigation and blanking algorithms give almost similar tracking performance with 5 dB gain compared to without mitigation case.

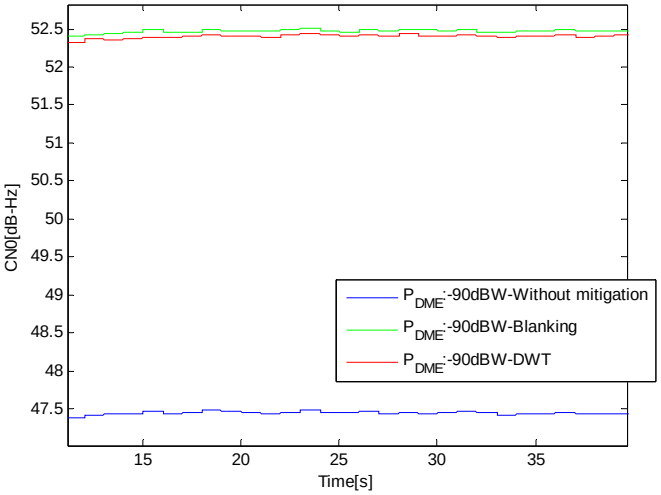


Figure C.4 Tracking sensitivity levels with strong DME interference (-90 dBW)

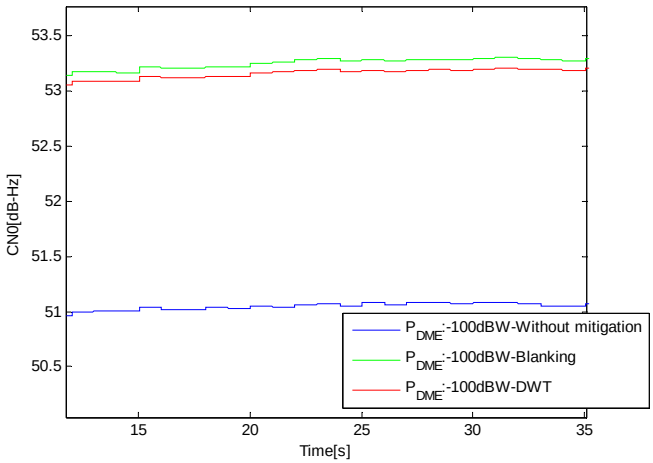


Figure C.5 Tracking sensitivity levels with medial DME interference (-100 dBW)

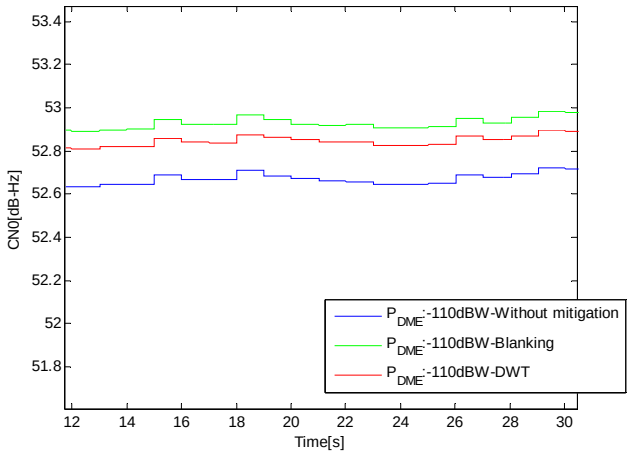


Figure C.6 Tracking sensitivity levels with weak DME interference (-110 dBW)